UNIVERSIDADE TECNOLÓGICA FEDERAL DO PARANÁ

JOÃO PAULO ALMIRÃO DE JESUS

ABORDAGENS COMPUTACIONAIS APLICADAS AO ESTUDO DE SEMICONDUTORES NANOESTRUTURADOS

LONDRINA

2022

JOÃO PAULO ALMIRÃO DE JESUS

ABORDAGENS COMPUTACIONAIS APLICADAS AO ESTUDO DE SEMICONDUTORES NANOESTRUTURADOS

Computational Methodologies Applied to the Study of Nanostructured Semiconductors

Dissertação apresentada como requisito para obtenção do título de Mestre em Ciência e Engenharia de Materiais da Universidade Tecnológica Federal do Paraná (UTFPR).
Orientador: Prof. Dr. Felipe de Almeida La Porta.

LONDRINA

2022

Ministério da Educação
Universidade Tecnológica Federal do Paraná
Campus Londrina

JOAO PAULO ALMIRAO DE JESUS

ABORDAGENS COMPUTACIONAIS APLICADAS AO ESTUDO DE SEMICONDUTORES NANOESTRUTURADOS

Trabalho de pesquisa de mestrado apresentado como requisito para obtenção do título de Mestre Em Ciência E Engenharia De Materiais da Universidade Tecnológica Federal do Paraná (UTFPR). Área de concentração: Materiais Para Aplicação Em Engenharia E Tecnologia.

Data de aprovação: 27 de Setembro de 2022

Dr. Felipe De Almeida La Porta, Doutorado - Universidade Tecnológica Federal do Paraná

Dr. Anderson Dos Reis Albuquerque, Doutorado - Universidade Federal do Rio Grande do Norte (Ufrn)

Dra. Erica Cristina Moreno Nascimento, Doutorado - Universidade de Brasília (Unb)

Documento gerado pelo Sistema Acadêmico da UTFPR a partir dos dados da Ata de Defesa em 21/10/2022.

AGRADECIMENTOS

RESUMO

Essa dissertação tem como principal objetivo a aplicação de diferentes abordagens computacionais em dois estudos de casos, utilizando clusters hexagonais, com configuração M_6X_6 (M = Zn, Cd e X = S, O), como modelos para semicondutores coloidais de ZnS, $Zn_{6-x}Cd_xS_6$, CdS e ZnO com estrutura wurtzita. No primeiro trabalho, foi apresentado um estudo teórico sobre os efeitos de um campo elétrico na estrutura eletrônica e nas propriedades espectroscópicas de clusters de $Zn_{6-x}Cd_xS_6$. Assim, foram identificadas distorções nos ângulos e comprimentos de ligações conforme a hibridização dos clusters devido a estrutura mais compacta de Zn_6S_6 em relação ao Cd_6S_6, sendo a estrutura $Zn_3Cd_3S_6$ a mais distorcida e, também, os modos ativos Raman e as propriedades termodinâmicas, sugerindo os clusters de Zn_6S_6 como os mais estáveis. Com a aplicação do campo elétrico, as distorções dos comprimentos e ângulos de ligações aumentaram significativamente, com limite em 0,20 V $Å^{-1}$, sendo observada polarização das estruturas locais, além do efeito quântico Stark verificado pelos desvios de energia das propriedades físicas e na polarização dos orbitais HOMO e LUMO, mantendo uma tendência ao longo do trabalho. No segundo trabalho, foi feita uma abordagem teórica-experimental de nanopartículas de ZnS e ZnO em três partes. Na primeira parte foi realizada a síntese das nanopartículas por meio da rota hidro(solvo)térmica e as propriedades estruturais, espectroscópicas e fotocatalíticas analisadas, indicando a excelente capacidade das nanopartículas em degradar o corante azul de metileno. Na segunda parte, foram simuladas as estruturas no estado fundamental e excitado de clusters de Zn_6S_6 e Zn_6O_6, aprofundando então nas propriedades eletrônicas, vibracionais e no comportamento químico, no qual as análises de QTAIM e NBO mostraram um maior caráter iônico das ligações do cluster Zn_6O_6, resultando em uma estrutura mais polarizada e distorcida e, consequentemente, em defeitos intrínsecos. Na última parte, os clusters optimizados foram submetidos a um estudo de ancoramento molecular e a inibição das principais enzimas do SARS-CoV-2, *Escheria coli* e *Fusarium solani* avaliadas, sugerindo um largo espectro de atividade antimicrobiana para as nanopartículas de ZnO e ZnS e elucidando a influência do estado excitado na maior atividade de inibição contra os agentes patogênicos. Com isso, nesse último estudo foram descobertas alta reatividade das nanopartículas como agente infectantes, bloqueio na região UVA e UVB e um largo espectro de propriedades antimicrobianas. Portanto, como mostrado nos resultados dos artigos, os métodos computacionais atingiram excelentes resultados em ambos os trabalhos, sempre seguindo tendências e apresentando valores próximos aos presentes na literatura para os sistemas alvos e dentro da margem de erro metodológico, destacando então a eficiência dos cálculos teóricos no estudo de materiais funcionais.

Palavras-chave: DFT; Semicondutores; Nanoestrutura; Docking; Processamento hidro(solvo)térmico

ABSTRACT

This thesis is mainly focused on applying different computational methodologies in two case studies, using hexagonal clusters with M_6X_6 (M = Zn, Cd e X = S, O) configuration as models for ZnS, $Zn_{6-x}Cd_xS_6$, CdS, and ZnO colloidal semiconductors with wurtzite structure. In the first work, it was presented the theoretical study of the effects of an electric field on the electronic structure and spectroscopic properties of $Zn_{6-x}Cd_xS_6$ clusters. Hence, it was identified distortions in the bond angles and lengths according to the cluster hybridization due to the more compact structure of Zn_6S_6 in comparison to Cd_6S_6, while the $Zn_3Cd_3S_6$ cluster was the most distorted, as well as the Raman active-modes and the thermodynamical properties, suggesting the Zn_6S_6 clusters as the most stable. Under the effects of an electric field, the distortions in bond angles and lengths increase significantly, reaching a limit at 0.20 V $Å^{-1}$, thus observing polarizations in the local structures and verifying the quantum Stark effect due to energy shifts in the physical properties and the HOMO and LUMO polarizations, keeping a tendency throughout the text. In the second work, a theoretical-experimental approach was taken in the study of ZnS and ZnO compounds in three steps. First, ZnS and ZnO nanoparticles were synthesized by means of the hydro(solvo)thermal route and their structural, spectroscopic, and photocatalytic properties were analyzed, showing their excellent ability to degrade methylene blue dye. Second, the ground and excited state structures of Zn_6O_6 and Zn_6S_6 were simulated, studying their electronic and vibrational properties and their chemical behavior, in which QTAIM and NBO analyses indicated the higher ionic bond character of ZnO clusters, resulting in a more polarized and distorted structure and, as consequence, intrinsic defects. Lastly, the optimized clusters were submitted to molecular docking study, and their ability to inhibit the proteins of the SARS-CoV-2, *Escherichia coli* and *Fusarium solani* were evaluated, suggesting a broad spectrum of antimicrobial activity for the ZnO and ZnS nanoparticles and elucidating the excited state influence into the higher inhibition activity against pathogenic agents. Hence, in this last study, it was discovered the high reactivity of these particles as disinfectant agents, UVA and UVB blocking ability, and a large spectrum of antimicrobial properties. Therefore, as shown in the results, the computational approaches reached excellent results in both works, always following tendencies and presenting values close to those reported in the literature and within the methodological deviation, highlighting the efficiency of theoretical calculations in the study of functional materials.

Keywords: DFT; Semiconductors; Nanostructure; Docking; Hydro(solvo)thermal processing

SUMÁRIO

1. INTRODUÇÃO

Com o rápido desenvolvimento tecnológico e o surgimento de novos dispositivos optoeletrônicos, nasceu uma grande necessidade social e tecnológica por novos materiais com propriedades físicas ajustáveis que possibilitam a confecção de dispositivos de alta performance. Esses materiais, conhecidos também como materiais funcionais, possuem excelentes propriedades eletrônicas e ópticas ajustáveis por meio do controle de suas características físicas (como tamanho, estrutura, composição, morfologia, bem como, imperfeições nestes parâmetros) tornando possível a criação de uma nova geração de dispositivos multifuncionais (LA PORTA; TAFT, 2021, 2020; LONGO; LA PORTA, 2017).

Entre esses materiais, os semicondutores de configuração II-VI (II = Zn, Cd e VI = O, S), como por exemplo, o óxido de zinco (ZnO), sulfeto de zinco (ZnS) e sulfeto de cádmio (CdS) ganharam destaque na literatura pelas suas atrativas propriedades eletrônicas, ópticas e fotocatalíticas, bem como, devido a sua simplicidade de fabricação e grande versatilidade de emprego em diversas tecnologias (DE JESUS; JIMENEZ; LA PORTA, 2021; KOVALENKO et al., 2015; MURRAY; KAGAN; BAWENDI, 2000; TALAPIN et al., 2010).

Por exemplo, o ZnO (Figura 1-A) é um material semicondutor com célula unitária hexagonal (wurtzita) que apresenta *band gap* em torno de 3,27 eV na fase *bulk*, uma alta energia de ligação dos éxcitons e resistência a radiação ultravioleta, sendo um possível material para aplicações em dispositivos com altas temperaturas de operação (LOOK, 2001; NAUSE; NEMETH, 2005).

Já no caso do ZnS (Figura 1-B), sua estrutura *bulk* demonstra a fase cúbica (blenda de zinco) como preferencial e um *bandgap* elevado de 3,72 eV, resultando em emissões em comprimentos de onda menores que o ZnO, bem como, um alto índice de refração e alta transmitância na região do visível, sendo estas características desejáveis para dispositivos optoeletrônicos e aplicações fotocatalíticas (LA PORTA et al., 2014a; LIN; HO, 2017).

Em adição as características comentadas acima, ambos ZnO e ZnS também apresentam excelentes propriedades antimicrobiana, mesmo em baixas concentrações, contra uma grande variedade de organismos (DHUPAR et al., 2021; GUDKOV et al., 2021; NAVARRO-LÓPEZ et al., 2021). Por exemplo, esses materiais apresentaram elevada atividade biológica contra a *Escherichia coli* e *Staphylococcus*

aureus, no qual somada a sua biocompatibilidade e baixo custo, fazem desses sistemas agentes antimicrobianos muito promissores (DHUPAR et al., 2021; GUDKOV et al., 2021; NAVARRO-LÓPEZ et al., 2021).

Em contraste aos outros materiais mencionados acima, o CdS (Figura 1-C) possui configuração wurtzita mas é diferenciado pelo seu *band gap* de 2,42 eV, sendo significativamente menor em relação aos materiais do mesmo grupo contendo zinco. Além disso, devido a sua capacidade de absorver a maior parte da luz na região do visível, o CdS pode ser considerado com um dos materiais mais proeminentes na produção de H_2 e como camada ativa em dispositivos fotovoltaicos (AOKI et al., 2021; CHENG et al., 2018).

Nessa perspectiva, é mostrado na Figura 1-D o alinhamento de bandas de alguns semicondutores derivados de óxidos e calcogênios, sendo identificadas as energias das bandas de valência e condução e o *band gap* em relação ao ZnS, devido este material ser um dos primeiros semicondutores da família II-VI descobertos (KLEIN, 2015). Por meio do alinhamento de bandas, em particular, é possível prever alguns comportamento físico-químico para estes semicondutores estudados.

Por exemplo, na Figura 1-E é elucidada a capacidade de oxirredução de nanopartículas de ZnS e evidenciada a possibilidade de sua aplicação fotocatalítica na produção de O_2 e decomposição de micropoluentes orgânicos (KLEIN, 2015; LA PORTA et al., 2017). Em adição, tanto o ZnS quanto CdS são fotocatalisadores com forte atividade redutora de CO_2 e evolução de H_2, enquanto o ZnO é um forte oxidante para degradação do radical livre de *OH e evolução de O_2 (UNDERWOOD; ROBINSON, 2022), estando em acordo com o alinhamento apresentado na Figura 1-D.

Portanto, no ponto de vista da pandemia provocada pelo SARS-CoV-2 e a constante ameaça de agentes patogênicos comuns que mostram crescente resistência a antibióticos, as propriedades antimicrobianas e fotocatalíticas apresentadas por nanopartículas a base de zinco fazem destes materiais candidatos muito promissores para aplicações como agente antimicrobianos e desinfetantes. Exemplificando, Sportelli et al. (2022) relatou a eficiência *in vitro* contra o SARS-CoV-2 de nanopartículas de ZnO sintetizadas por uma rota segura ao meio ambiente, mostrando uma redução da carga viral de até 90% e sugerindo a aplicação das nanopartículas em revestimentos. Uma redução quase completa da infectividade de suspensões de SARS-CoV-2 por revestimentos porosos de nanopartículas de ZnO

também foi reportada pelo trabalho de Hosseini et al. (2021), no qual os autores relacionaram a redução da infectividade com a porosidade de materiais hidrofílicos e sugeriram a aplicação do revestimento em objetos. Com isso, a capacidade antimicrobiana de revestimentos de nanopartículas de ZnO e ZnS com aplicação em máscaras e seu elevado interesse social, econômico e tecnológico são destacadas em um dos capítulos deste texto.

Figura 1 – Monocristais de A) ZnO, B) ZnS e C) CdS. D) Alinhamento de bandas intrínseco de semicondutores calcogênicos. E) Diagrama da capacidade oxirredução de nanopartículas de ZnS
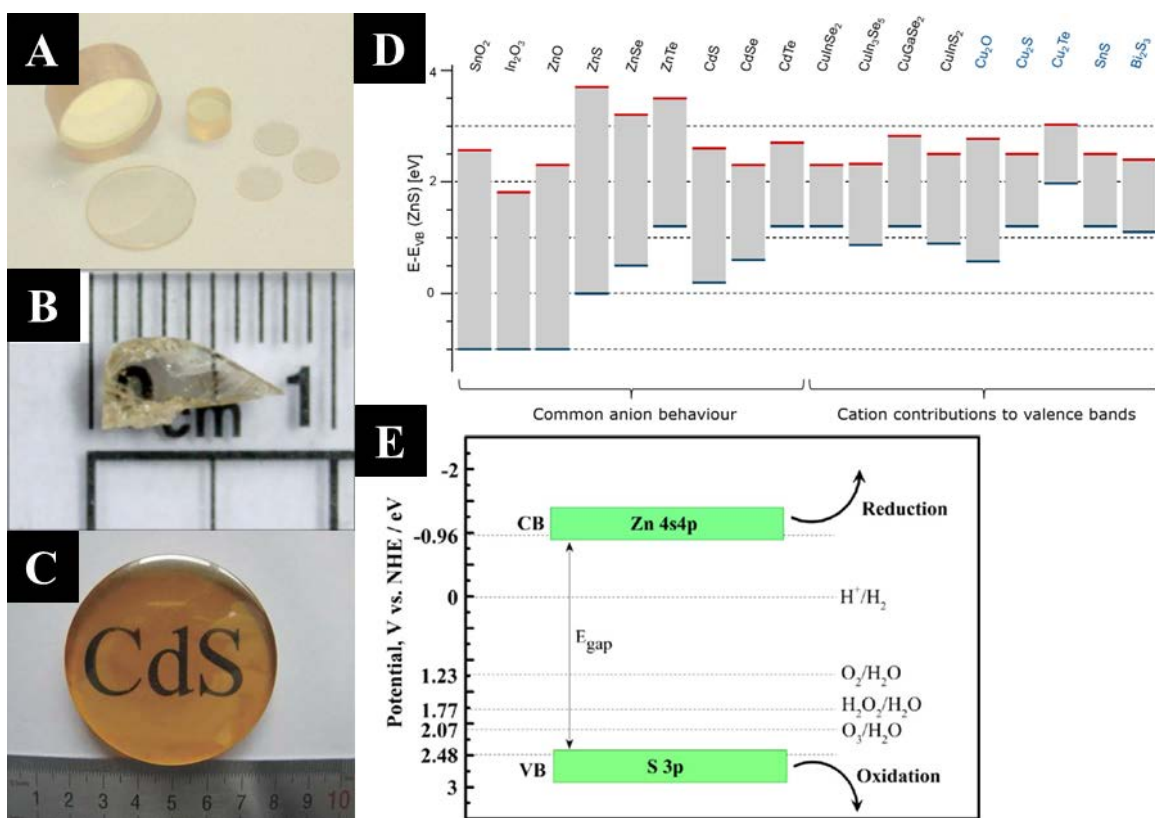
Fonte: A) Nause e Nemeth (2005), B) Lin e Ho (2017), C) Huo et al. (2018), D) Klein (2015) e E) La Porta et al. (2017)

Ainda dentro desse grupo de materiais, as nanoestruturas conhecidas como pontos quânticos e compostas por ZnS, CdS e ZnO são sistemas de elevado interesse científico em virtude das suas propriedades físicas facilmente ajustáveis e dos efeitos resultantes do confinamento quântico do éxciton, tendo características favoráveis para uma variedade de aplicações tecnológicas, como fotocatálises (DI MAURO et al., 2017; GARG et al., 2016; LA PORTA et al., 2017; LEE; WU, 2017; QI et al., 2017),

células fotovoltaicas (AOKI et al., 2021; FONSECA et al., 2018; HUANG; YIN; ZHENG, 2011; UMMARTYOTIN; INFAHSAENG, 2016), diodos emissores de luz (PEARTON; REN, 2014; SHEN et al., 2014; ZHANG et al., 2019), (bio)sensores (BAI et al., 2021; BERGER et al., 2016; MOSTAFA et al., 2021; TERESHCHENKO et al., 2016; WANG et al., 2011; ZENG et al., 2014).

No entanto, o estudo desses sistemas pode se tornar muito complexo em razão da limitação da nanoescala, impossibilitando o emprego de metodologias experimentais convencionais (BURNIN; SANVILLE; BELBRUNO, 2005; DE JESUS; JIMENEZ; LA PORTA, 2021; JAIN; SHIN; PERSSON, 2016; LA PORTA et al., 2014b; RAUBACH et al., 2013). Sendo assim, os métodos computacionais são ferramentas muito úteis na elucidação das propriedades físico-químicas de sistemas com dimensões reduzidas e também na descoberta/previsão de novos materiais funcionais (BURKE, 2012; BURNIN; SANVILLE; BELBRUNO, 2005; DE JESUS; JIMENEZ; LA PORTA, 2021; JAIN; SHIN; PERSSON, 2016; LA PORTA et al., 2014b; RAUBACH et al., 2013).

Na perspectiva computacional, a Teoria do Funcional da Densidade (DFT) emergiu recentemente como uma opção de excelente performance e qualidade para os cálculos de primeiro princípio, em contrapartida a outros métodos químico-quânticos, permitindo uma acurada descrição de suas propriedades sob menor custo computacional (ALBERI et al., 2019; HAFNER; WOLVERTON; CEDER, 2006; NEUGEBAUER; HICKEL, 2013). Notáveis exemplos da aplicação da DFT para o tratamento de sistemas moleculares em fase gasosa (LA PORTA et al., 2014a), em solvente (PLIEGO JR, 2006) e sólidos periódicos (LA PORTA et al., 2014c) podem ser facilmente encontradas na literatura e, além disso, esta metodologia de cálculo está amplamente disponível em diversos *softwares* computacionais.

Dessa forma, a DFT possibilita a simulação e o entendimento das propriedades espectroscópicas, estruturais e eletrônicas, assim como suas relações, auxiliando em ambos estudos teóricos e experimentais, como será visto em um dos capítulos no qual é aplicada em uma investigação teórica sobre o efeito de um campo elétrico nas propriedades de pontos quânticos (BURNIN; SANVILLE; BELBRUNO, 2005; DE JESUS; JIMENEZ; LA PORTA, 2021; JAIN; SHIN; PERSSON, 2016; LA PORTA et al., 2014b; RAUBACH et al., 2013).

Além da DFT, outras metodologias computacionais são amplamente usadas nos estudos de novos materiais e biomoléculas, como a Teoria Quântica dos Átomos

em Moléculas (*Quantum Theory of Atoms in Moléculas*, QTAIM) de Bader, a teoria dos Orbitais Naturais de Ligação (*Natural Bond Orbitals*, NBOs) e os métodos de modelagem por ancoramento molecular. Como será detalhado na fundamentação teórica desta dissertação, em geral, os métodos de QTAIM e NBO são capazes de fornecer informações úteis sobre a estrutura eletrônica e a natureza das ligações químicas, possibilitando uma completa avaliação do ambiente químico e do caráter de ligações dos sistemas alvos, por exemplo (BADER, 1991; FOSTER; WEINHOLD, 1980). Em relação aos cálculos de ancoragem molecular, esses métodos são muito empregados no estudo de interação entre ligantes e receptores e para análises conformacionais de proteínas, enzimas e fármacos, sendo, portanto, ferramentas indispensáveis no desenvolvimento de novos medicamentos (ASSIS et al., 2021a, 2021b; DE JESUS et al., 2021; DIAS; DE AZEVEDO JR., 2008; FAN; FU; ZHANG, 2019; PAGADALA; SYED; TUSZYNSKI, 2017).

Portanto, este trabalho tem como foco principal apresentar dois estudos de caso, no qual abordagens computacionais foram empregadas na resolução de problemas pertinentes a nanopartículas de ZnS, CdS e ZnO, a partir do emprego de metodologias de baixo custo computacional. No primeiro trabalho publicado na revista *Computational Materials Science* (DOI: 10.1016/j.commatsci.2020.110147), foram analisados e pontuados os efeitos de um campo elétrico na estrutura eletrônica e nas propriedades espectroscópicas de clusters de $Zn_{6-x}Cd_xS_6$ como modelo para pontos quânticos de ZnS e CdS. Por fim, o segundo trabalho, recentemente publicado no serviço ChemRxiv (DOI: 10.26434/chemrxiv-2022-v2tc6) no formato de *pre-print* e sob revisão por pares, foi feito uma abordagem teórica-experimental nas propriedades espectroscópicas e fotocatalíticas de nanopartículas de ZnS e ZnO, avaliando o seu potencial em revestimento antimicrobiano para máscaras contra agentes como SARS-CoV-2, *Fusarium oxysporum* e *Escheria coli*.

2.   REFERENCIAL TEÓRICO

2.1.   Materiais Funcionais

Com base nos avanços científicos do último século, aliado ao rápido desenvolvimento tecnológico, a busca por novos materiais com propriedades adaptadas para diversas aplicações específicas se tornou em larga medida o foco de diversos campos da Ciência, ou seja, levando a criação de muitos grupos de pesquisa multidisciplinar (LA PORTA; TAFT, 2021, 2020; LONGO; LA PORTA, 2017). O destaque principal desses materiais funcionais se deve a possibilidade de ajustar suas propriedades físico-químicas por meio da otimização dos parâmetros de produção, tornando possível a síntese de materiais seletos para as aplicações desejadas.

Dessa maneira, há vários caminhos para a produção de novos materiais funcionais, sendo alguns dos mais conhecidos a síntese solvotérmica, a rota por injeção a quente e o banho químico. Por meio dessas, as propriedades físicas dos produtos são ajustadas por meio dos parâmetros de síntese, sendo estes os reagentes precursores, a estequiometria, o efeito de solvente, a temperatura, o pH do meio, o tempo de reação, a adição de agentes surfactantes e impurezas, a aplicação de micro-ondas (no caso da síntese solvotérmica), entre outros (SUZUKI et al., 2019). Tais parâmetros são algumas das variáveis experimentais mais importantes para o controle das características dos produtos obtidos, permitindo forte flexibilidade na engenharia desses novos materiais.

Em relação ao controle das propriedades físicas dos materiais, por exemplo, na síntese solvotérmica, Jiang et al. (2008) demostraram a obtenção de diferentes morfologias de nanocristais de ZnS por meio do controle de solvente, sendo estes o etileno glicol, etilenodiamina, 1-hexanol e a mistura de etilenodiamina e ácido nítrico. Na Figura 2-A é ilustrado as morfologias obtidas pelo controle de etilenodiamina/ácido nítrico. No mesmo artigo, os autores mostraram também o controle de fases cristalinas por meio da troca de solvente usado na síntese, no qual etileno glicol e etilenodiamina levaram a estruturas wurtzita, enquanto o 1-hexanol resultou em configuração de blenda de zinco (JIANG et al., 2008).

De forma similar, o estudo de La Porta et al. (2013) mostrou o efeito do precursor de zinco nas propriedades ópticas de nanopartículas de ZnS, como mostrado no espectro de fotoluminescência na Figura 2-B (LA PORTA et al., 2013). Em outro trabalho, os autores indicaram o controle da fase cristalina do ZnS por meio

da adição de hidróxido de tetrabutilamônio na síntese solvotérmica assistida por micro-ondas, mostrando a mudança de preferência da fase cúbica pela hexagonal e, como consequência, o impacto nas suas propriedades (Figura 2-C e D (LA PORTA et al., 2014a). Em ambos os trabalhos, foram almejados produtos com diferentes características físicas para um mesmo sistema, que foram obtidos a partir do ajuste dos parâmetros experimentais de síntese.

Figura 2 – A) Controle de morfologia pelo ajuste de solvente. B) Controle da fotoluminescência pelo ajuste de precursor de zinco. C e D) Controle de *band gap* pelo ajuste de fase.
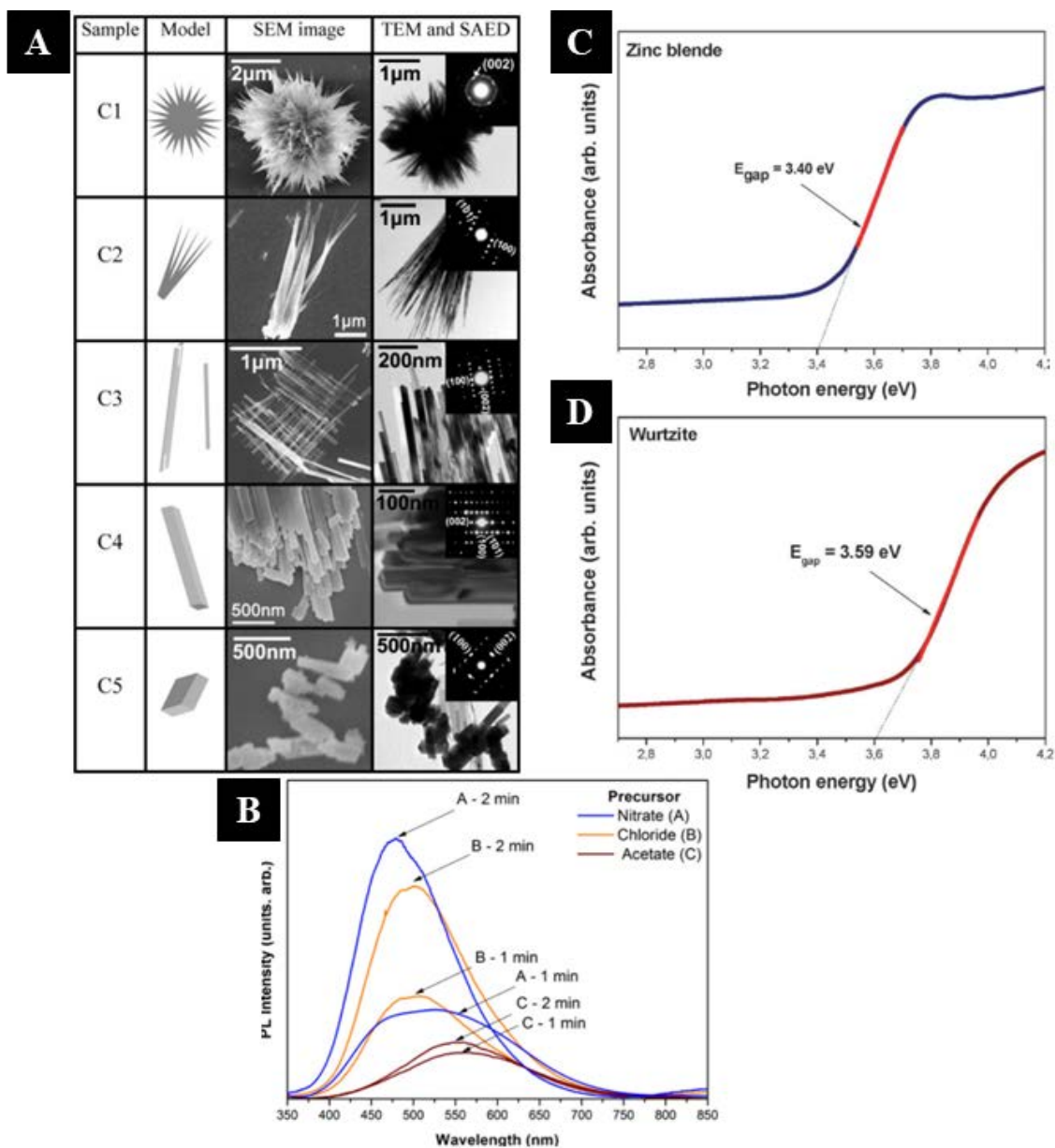
Fonte: adaptado de A) Jiang et al. (2008), B) La Porta et al. (2013), C e D) La Porta et al. (2014)

Junto a extensa variedade de materiais pesquisados pela literatura estão os semicondutores do grupo II-VI, a junção de um íon metálico do grupo 12 como o Zn^{2+} e Cd^{2+} com um ânion calcogênio como O^{2-} e S^{2-}. O elevado interesse por esses materiais, em particular, se deve principalmente pelas suas propriedades físico-químicas, dando grande flexibilidade para uma gama de aplicações tecnológicas, como comentado no capítulo anterior. Com isso, nesse trabalho é dado destaque ao ZnS, CdS e ZnO.

De maneira geral, os semicondutores de ZnS, CdS e ZnO apresentam estrutura *bulk* com *band gap* de 3,72, 2,42 e 3,27 eV, respectivamente (ASHRAFI; JAGADISH, 2007; CORTES, 2004; FANG et al., 2011). Normalmente, a configuração termodinamicamente mais estável do ZnS é a fase blenda de zinco, enquanto ambos ZnO e CdS cristalizam na fase wurtzita (ASHRAFI; JAGADISH, 2007; CORTES, 2004; DE JESUS; JIMENEZ; LA PORTA, 2021; FANG et al., 2011). No entanto, devido à redução de tamanho durante a cristalização de suas nanoestruturas, em particular, o equilibro termodinâmico é invertido e as fases metaestáveis se tornam preferenciais em baixas temperaturas (ASHRAFI; JAGADISH, 2007; CORTES, 2004; DE JESUS; JIMENEZ; LA PORTA, 2021; FANG et al., 2011). Em adição, os três materiais têm uma terceira fase que aparece em condições de pressões elevadas, a estrutura cúbica do tipo *rocksalt*, e por isso tem menos interesse tecnológico.

A vista disso, nas Figuras 3-A e B são apresentadas as células unitárias dos sistemas blenda de zinco (cúbica) e wurtzita (hexagonal), respectivamente. Na Figura 3-C são mostrados os padrões de difração de raios-X calculados para o CdS, ZnS e ZnO por meio das células unitárias de ambas geometrias hexagonais e cúbicas. Já na figura 3-D são organizados valores de constante de rede em função do *band gap* para semicondutores de algumas famílias (BURST et al., 2016).

Figura 3 – Estruturas A) blenda de zinco e B) wurtzita (baixo). C) Diagramas de raios-X simulados para o ZnO, ZnS e CdS com configurações wurtzita (W) e blenda de zinco (Z). D) Constante de rede de diferentes materiais semicondutores em função do *band gap*
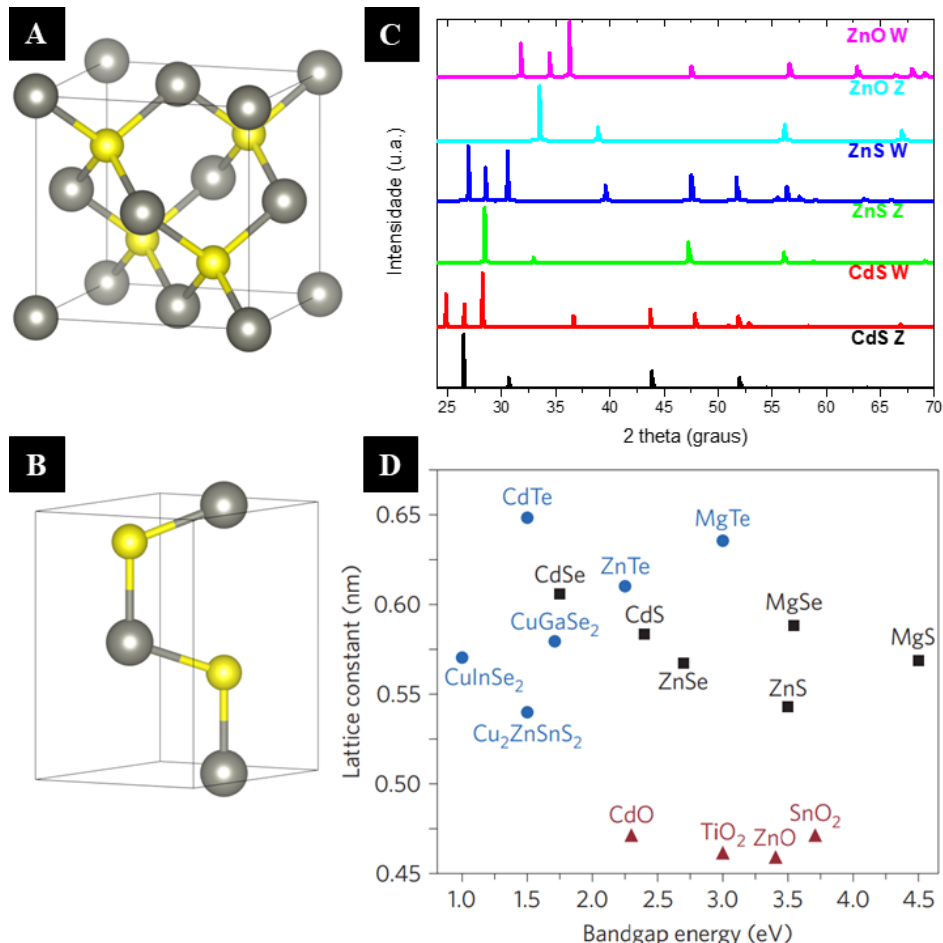
Fonte: A) a C) autoria própria (2022), D) adaptado de Burst et al. (2016)

Com o desenvolvimento de novas rotas sintéticas, uma diversidade de nanoestruturas com morfologias e tamanhos controlados foram amplamente obtidas para o ZnS, CdS, ZnO e muitos outros materiais. Em geral, as morfologias mais observadas, por exemplo, são na forma de nanobastões, nanofios, nanoesferas e outras geometrias como as apresentadas na Figura 2-A. No entanto, uma categoria de nanoestruturas recebeu atenção especial devido as propriedades decorrentes dos efeitos de confinamento quântico do éxciton (i.e, par elétron excitado e buraco), os pontos quânticos.

Em particular, as estruturas *bulk* são volumosas a ponto de os portadores de cargas apresentarem liberdade de movimento em três dimensões espaciais (3D), havendo locomoção com pouca restrição pela matriz cristalina (BIMBERG; POHL, 2011; DE JESUS; JIMENEZ; LA PORTA, 2021; SUPREET; SINGH, 2020). Mas no

caso de materiais nanocristalinos, o volume é reduzido drasticamente e, como consequência, a liberdade de movimento dos portadores de carga é impedida por barreiras de potenciais que levam ao efeito de confinamento quântico (BIMBERG; POHL, 2011; DE JESUS; JIMENEZ; LA PORTA, 2021; SUPREET; SINGH, 2020). Portanto, quando um cristal apresenta dimensões inferiores ao seu raio do éxciton de Bohr, o confinamento do éxciton pode ser observado em uma-, duas- e três-dimensões, resultando nos poços quânticos (2D), fios quânticos (1D) e pontos quânticos (0D) apresentados na Figura 4-A (BIMBERG; POHL, 2011; SUPREET; SINGH, 2020).

Figura 4 – A) Diferentes níveis de confinamento quântico e suas respectivas densidades de estados eletrônicos. B) Representação esquemática da dependência de *bandgap* e fotoluminescência pelo tamanho. C) Espectro de fotoluminescência de pontos quânticos núcleo/casca de CdSe/ZnS e D) quando submetidos a luz UV
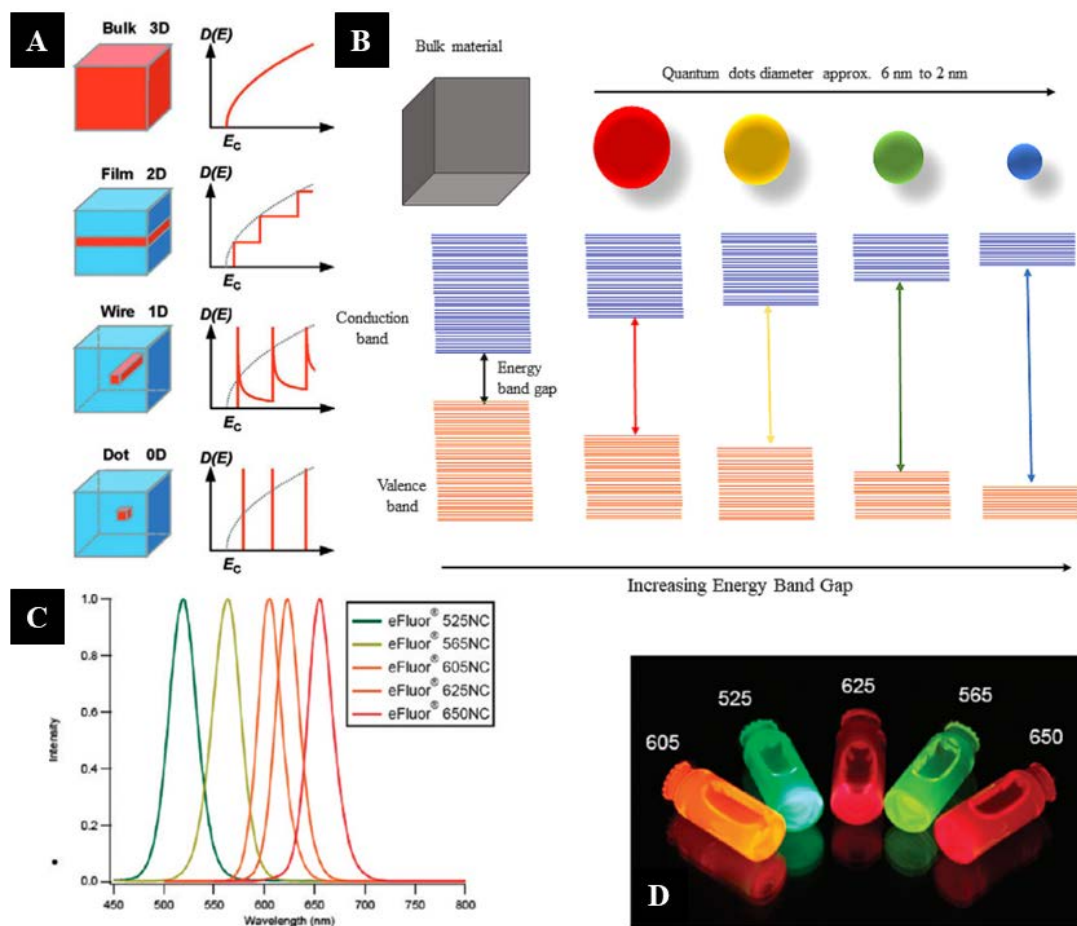
Fonte: adaptado de A) Bimberg e Pohl (2011), B) Supreet e Singh (2020), C) e D) Jennings et al. (2011)

Assim, os pontos quânticos, popularmente conhecidos como átomos artificiais, são definidos como nanopartículas com tamanhos geralmente entre 20 a 1 nm (Figura 4-B a C) (BIMBERG; POHL, 2011; DE JESUS; JIMENEZ; LA PORTA, 2021; JENNINGS et al., 2011; SUPREET; SINGH, 2020). Além disso, a concentração de defeitos estruturais também é significativamente inferior ao *bulk* e limitadas às suas dimensões, contribuindo para a engenharia de *band gap* ao mostrar valores elevados conforme a redução de tamanho e de estados eletrônicos na região proibida (BIMBERG; POHL, 2011; DE JESUS; JIMENEZ; LA PORTA, 2021; JENNINGS et al., 2011; SUPREET; SINGH, 2020).

2.2. Teoria do Funcional da Densidade

Com objetivo de ajudar no design de novos materiais funcionais, cientistas das mais diversas áreas aplicam abordagens computacionais sinergicamente com estudos experimentais (LA PORTA; TAFT, 2021, 2020; LONGO; LA PORTA, 2017). Existem várias metodologias computacionais que podem ser diferenciadas pelo nível teórico utilizado, desde os cálculos semiempíricos e químico-quânticos de Hartree-Fock baseados em equações de onda, a DFT e os métodos de dinâmica molecular e híbridos, até o desenvolvimento recente de algoritmos de inteligência artificial e *machine learning*. Entre as metodologias teóricas, nesta dissertação focaremos nos cálculos baseados na DFT que ganharam imensa popularidade ao longo das últimas décadas, junto com o desenvolvimento de computadores mais robustos e com maior poder computacional, especialmente para resolução de problemas de grande complexidade (ALBERI et al., 2019; HOHENBERG; KOHN, 1964; KOHN; SHAM, 1965; SEH et al., 2017).

Desse modo, a DFT se provou muito útil na interpretação e explicação de dados experimentais, no discernimento das propriedades eletrônicas, estruturais e espectroscópicas de materiais, no estudo do comportamento físico-químico de sistemas químicos, na previsão de novos materiais e estruturas desconhecidas e, essencial no entendimento dos fenômenos resultados da ordem atômica, quando a elucidação completa das propriedades físico-químicas são limitadas pela nanoescala (BURNIN; SANVILLE; BELBRUNO, 2005; DE JESUS; JIMENEZ; LA PORTA, 2021; JAIN; SHIN; PERSSON, 2016; LA PORTA et al., 2014b; RAUBACH et al., 2013).

Com isso em mente, uma perspectiva na capacidade da DFT em prever as propriedades de diversos materiais é dada pelo excelente *review* de Jain et al. (2016) sobre DFT aplicada no campo de energia renovável. Embora apenas alguns dos vários trabalhos apresentados pelo *review* são citados neste texto, há muitos artigos excelentes sobre a DFT aplicada ao estudo de materiais além da aplicação em energia renovável (ALBERI et al., 2019; CEDER, 1998; HAFNER; WOLVERTON; CEDER, 2006; HAUTIER; JAIN; ONG, 2012; JAIN; SHIN; PERSSON, 2016; NEUGEBAUER; HICKEL, 2013; SEH et al., 2017; TAFT et al., 2021).

Por exemplo, Anasori et al. (2015) preveram por meio da DFT a ordenação atômica de vinte novos carbonetos bidimensionais para aplicação em anodos, cujo um desses materiais, o $Mo_2Ti_2C_2T_x$ (sendo T relacionado a terminação da superfície), foi sintetizado e apresentou performance razoável (ANASORI et al., 2015). Em produção de hidrogênio, Yan et al. (2015b) investigaram uma triagem computacional com mais de cem óxidos metálicos de transição com propriedades fotocatalíticas para aplicação em separação da água, sendo baseada no *bandgap* e na estabilidade em meio aquoso (YAN et al., 2015b), identificando o $Mn_2V_2O_7$ como um candidato promissor para essa aplicação e confirmando experimentalmente sua estabilidade de fotocorrente em pH elevado (YAN et al., 2015b). Na área de fotovoltaica, Yan et al. (2015) fizeram a triagem de ligas conhecidas e hipotéticas de *half-Heusler* e descobriram os princípios para o design dessa classe de materiais, levando na previsão e síntese do TaIrGe com alta transparência a luz visível e mobilidade de Hall (YAN et al., 2015a).

De acordo com os trabalhos acima, a capacidade da DFT em prever as propriedades dos materiais é geralmente avaliada por medidas experimentais, sugerindo a aplicação da DFT como uma prática de pesquisa a ser adotada como padrão. Nessa perspectiva, na Figura 5-A é apresentada a popularidade da DFT pelo número de publicações nas últimas duas décadas de acordo com a base de dados *Web of Science*, indicando uma forte relação com o estudo de materiais funcionais.

Figura 5 – A) Número anual de publicações com as palavras-chaves "DFT" (azul) e "DFT + Materials" (vermelho). B) Propriedades de um sistema calculado por equações de ondas (esquerda) e equações de Kohn-Sham (direita). C) Escada de Jacó da DFT" por John Perdew e Karla Schmidt. D) "Sopa de letras" dos funcionais mais comuns da DFT.
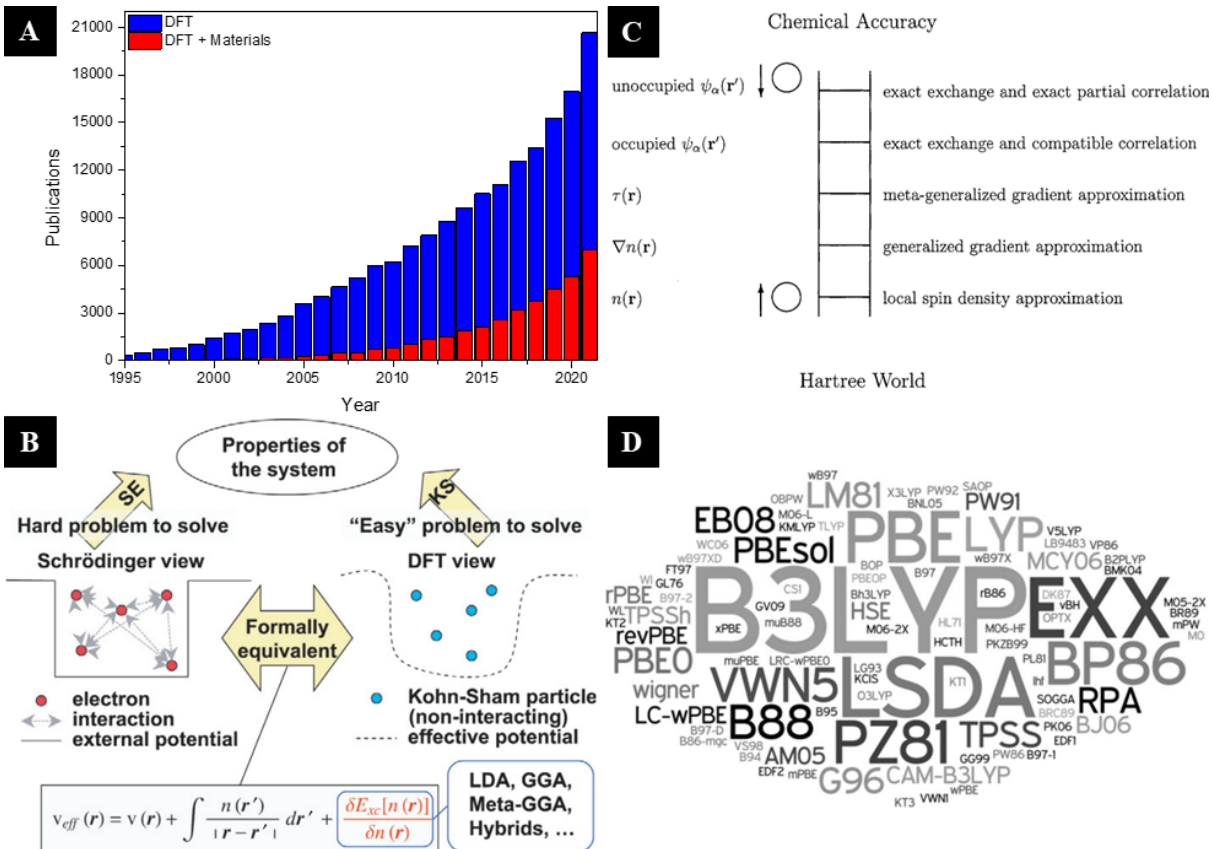
Fonte: A) Web of Science (2022), B) Mattsson et al. (2005), C) Perdew e Schmidt (2001), D) Burke e Elliott (2012)

Os princípios da DFT são fundamentados em dois teoremas propostos por Pierre Hohenberg e Walter Kohn em 1964 (HOHENBERG; KOHN, 1964). O primeiro teorema leva em consideração todas as propriedades do estado fundamental, incluindo a energia total, como funcionais da densidade eletrônica do estado fundamental $n(r)$, sendo determinado de maneira unívoca a partir de um potencial externo V_{ex} (HAUTIER; JAIN; ONG, 2012; HOHENBERG; KOHN, 1964). Já o segundo teorema considera que a densidade eletrônica minimiza o funcional de energia $E_0[n_0(r)]$, sendo a energia do estado fundamental E_0 igual a esse mínimo (HAUTIER; JAIN; ONG, 2012; HOHENBERG; KOHN, 1964). Dessa maneira, a energia total de um sistema prevista pela DFT pode ser dada pela equação (1)

$$E[n] = T[n] + U[n] + \int V(r)n(r)\,d^3r$$

(1)

Sendo n é a densidade eletrônica, r as coordenadas espaciais, E a energia total, T o termo da energia cinética, V o termo do potencial externo referentes as interações elétron-núcleo e U o termo do potencial de repulsão elétron-elétron.

Enquanto os teoremas de Hohenberg e Kohn permitam a descrição de um sistema no estado fundamental por meio da densidade eletrônica, uma maneira de calcular sua energia não é demonstrada pelos autores. Assim, em 1965, Kohn e Lu Jeu Sham ultrapassaram esse obstáculo ao aproveitar do princípio variacional, resultado do segundo teorema ao minimizar o funcional de energia, e propuseram as equações de Kohn-Sham, tendo em mente um sistema auxiliar não-interativo e levando a equação (2) ao aplicar um potencial efetivo de uma partícula dado pela equação (3) (HAUTIER; JAIN; ONG, 2012; KOHN; SHAM, 1965)

$$\left[-\frac{\hbar^2}{2m}\nabla^2 + V_s(r) \right] \phi_i(r) = \epsilon_i \phi_i(r)$$

(2)

$$V_s(r) = V(r) + \int \frac{e^2 n_s(r')}{r - r'} d^3r' + V_{xc}[n_s(r)]$$

(3)

$$n_s(r) = \sum_{i=0}^{N} \phi_i(r)^2$$

(4)

No qual, na equação (3), o segundo termo é o termo Hartree relacionado a repulsões elétron-elétron e o terceiro termo o potencial de troca-correlação, incluindo todas as interações (HAUTIER; JAIN; ONG, 2012). Além disso, ϕ_i são os orbitais representando a densidade eletrônica original e n_s a densidade eletrônica de Kohn-Sham (HAUTIER; JAIN; ONG, 2012).

Dessa forma, por meio das equações de Kohn-Sham e dos teoremas de Hohenberg e Kohn, a densidade eletrônica $n_s(r)$ de um sistema de muitos corpos pode ser variada até ser encontrada uma possibilidade no qual o funcional da energia $E_0[n_0(r)]$ atinja o mínimo global, alcançando então a densidade eletrônica do estado fundamental $n_0(r)$ e, consequentemente, as propriedades eletrônicas do sistema e suas derivadas (Figura 5-B) (HAFNER; WOLVERTON; CEDER, 2006; HAUTIER; JAIN; ONG, 2012).

No entanto, embora os teoremas sugerem um funcional de potencial de troca-correlação universal $V_{xc}[n_s(r)]$, este funcional é desconhecido. Como consequência, esse problema é contornado pelo desenvolvimento de funcionais aproximados por teóricos excepcionais em suas áreas, assim assumindo várias formas e tornando o cálculo aproximado das propriedades eletrônicas pela DFT possível para uma imensa variedade de sistemas com propriedades e ambientes químicos distintos (HAFNER; WOLVERTON; CEDER, 2006; HAUTIER; JAIN; ONG, 2012).

Os funcionais de densidade eletrônica são geralmente classificados de acordo com seu nível teórico, sendo os mais comuns e básicos os funcionais por aproximação da densidade local (*Local Density Approximation*, LDA), considerando apenas a densidade eletrônica $n(r)$ na avaliação do funcional; e os funcionais por aproximação do gradiente generalizado (*Gradient Generalized Approximation*, GGA), introduzindo uma dependência do gradiente da densidade $\nabla n(r)$, tais como o BLYP e PBE (ANDRADE, 2016; HAFNER; WOLVERTON; CEDER, 2006; HAUTIER; JAIN; ONG, 2012).

A energia estimada por esses funcionais pode ser alcançada pela equação (5) e (10) no caso dos funcionais LDA e GGA, respectivamente (KOCH; HOLTHAUSEN, 2001; PEREIRA DA SILVA, 2010). O termo $E_{xc}[n(r)]$ em ambas equações representa a soma das contribuições de troca $\varepsilon_x(n(r))$ e correlação $\varepsilon_c(n(r))$, apresentados pelas equações (7) e (8), sendo r_s o raio de uma esfera com volume igual ao volume por elétron de condução (KOCH; HOLTHAUSEN, 2001; PEREIRA DA SILVA, 2010). No entanto, vale notar que uma forma explícita da parte de correlação é desconhecida, aplicando assim simulações altamente precisas de Monte-Carlo do modelo de gás de elétrons homogêneo realizados inicialmente por Ceperly e Alder em 1980 (CEPERLEY; ALDER, 1980; KOCH; HOLTHAUSEN, 2001; PEREIRA DA SILVA, 2010).

$$E_{xc}[n(r)] = \int n(r)\varepsilon_{xc}(n(r))\, dr$$

(5)

$$\varepsilon_{xc}(n(r)) = \varepsilon_x(n(r)) + \varepsilon_c(n(r))$$

(6)

$$\varepsilon_x(n(r)) = -\frac{0{,}458}{r_s}$$

(7)

$$e_c(n(r)) = -\frac{0{,}44}{r_s + 7{,}8}$$

(8)

$$r_s = \left[\left(\frac{4\pi}{3}\right)n(r)\right]^{-\frac{1}{3}}$$

(9)

$$E_{xc}[n(r)] = \int e_{xc}[n(r), \nabla n(r)]dr$$

(10)

Em complementação aos funcionais de densidade mais básicos, outras classes mais complexas surgiram a partir da evolução da LDA e GGA, como os meta-GGA, contando com a densidade eletrônica cinética na forma de um laplaciano $\nabla^2 n(r)$ (e.g. TPSS e M06-L); os hyper-GGA, adicionando funções monoeletrônicas de Kohn-Sham no lugar de muitos corpos na avaliação do potencial de troca de Hartree-Fock; os híbridos, combinando parte do potencial de troca de Hartree-Fock (e.g. B3LYP e PBE0); e os *Range-Separated* (RSD), apresentando caráter Hartree-Fock dependente da distância entre elétrons (e.g. HSE06 e HISS) (ANDRADE, 2016; HAFNER; WOLVERTON; CEDER, 2006; HAUTIER; JAIN; ONG, 2012). Logo, com cada iteração, ambas a complexidade do cálculo e sua precisão aumentam significativamente, correspondendo uma hierarquia conhecida como "Escada de Jacó da DFT" (Figura 5-C e D) proposta por John Perdew (ANDRADE, 2016; HAFNER; WOLVERTON; CEDER, 2006; PERDEW, 2001).

Em adição a aproximação do funcional, as equações de Kohn-Sham também devem ser resolvidas de forma iterativa por combinações lineares de um conjunto de funções de bases representando as funções de onda monoeletrônicas, cujo suas

convergências têm papel essencial na precisão do cálculo computacional (HAFNER; WOLVERTON; CEDER, 2006). Assim, as funções de base são classificadas como localizadas ou por ondas planas e dependente do algoritmo disponível, no qual a escolha cuidadosa é essencial na elaboração de metodologias, uma vez que ambas as funções de bases e funcionais de densidade eletrônica são as raízes do cálculo mecânico quântico e podem facilmente levar a descrições incorretas ou precisas dos sistemas químicos (HAFNER; WOLVERTON; CEDER, 2006; MATTSSON et al., 2005).

Como visto anteriormente, a caracterização experimental de materiais com escalas nanométricas é muito difícil devido aos efeitos resultantes da própria nanoescala e da ordem atômica, tornando o emprego dos métodos computacionais extremamente úteis no estudo destes materiais (BURNIN; SANVILLE; BELBRUNO, 2005; DE JESUS; JIMENEZ; LA PORTA, 2021; JAIN; SHIN; PERSSON, 2016; LA PORTA et al., 2014b; RAUBACH et al., 2013). No entanto, ainda que na maioria dos casos a DFT possibilite o estudo e estimativa das diversas propriedades físico-químicas de materiais no estado *bulk*, os cálculos computacionais de sistemas com dimensões reduzidas podem se tornar muito complexos e caros de um ponto de vista computacional (CATLOW et al., 2010).

Com o objetivo de circundar esse problema, normalmente são realizadas modelagens teóricas com base nesses sistemas para simplificar e viabilizar o estudo computacional de nanomateriais. De maneira similar em que os pontos quânticos são usados como modelos simplificados no estudo teórico de sistemas de muitos corpos em razão do menor número de elétrons, a modelagem de clusters no estudo teórico de pontos quânticos também se tornou uma prática relativamente comum, como apresentado nas Figuras 6 e 7 (AZPIROZ et al., 2012; AZPIROZ; UGALDE; INFANTE, 2014; CATLOW et al., 2010; DE JESUS; JIMENEZ; LA PORTA, 2021; JACAK; WÓJS; HAWRYLAK, 1998; LA PORTA et al., 2014a; SANVILLE; BURNIN; BELBRUNO, 2006).

Nessa perspectiva, o excelente *review* por Catlow et al. (2009) pontua os principais motivos no qual a modelagem de clusters recebeu destaque nas últimas décadas. Como comentado pelos autores, em adição a pesquisa de fulerenos de carbono responsável por popularizar o cálculo de clusters de maneira geral, os clusters com dimensões menores apresentam maior simplicidade ao serem modelados em comparação com as nanopartículas, devido ao menor custo

computacional; também estão envolvidos nos complexos processos de nucleação e crescimento do estado condensado da matéria e ainda não consolidados pela comunidade científica; e suas propriedades físico-químicas (e.g. ponto de fusão) quando menores que 1 nm são muito diferentes das apresentadas pelo seu estado *bulk* (CATLOW et al., 2010).

Além disso, a existência desses clusters foi comprovada experimentalmente por medidas de espectrometria de massas por tempo de voo (Figura 6-B), apresentando números mágicos com estruturas locais ultra estáveis quando n = 6 e 13 para clusters com configuração M_nX_n (e.g. Zn_6S_6, Zn_6O_6, Cd_6S_6, Cd_6Se_6,) (SANVILLE; BURNIN; BELBRUNO, 2006). De forma complementar, aparentemente não há uma definição geral de tamanho para transição entre cluster e ponto quântico, uma vez que esse limite é fortemente dependente do sistema químico, como, por exemplo, os clusters de Zn_nO_n, apresentando propriedades do estado *bulk* a partir de $n > 75$ (CATLOW et al., 2010) para este sistema.

Figura 6 – A) Estruturas nos estados fundamentais ou mínimos globais de clusters de Zn_nO_n. B) Espectros de massa de clusters de Cd_nS_n obtidos por ablação a laser. Diagrama de correlação de energia de excitação teórica *vs* valores de referências obtida por diferentes funcionais de densidade eletrônica para clusters de C) Zn_6S_6 e D) Cd_6S_6
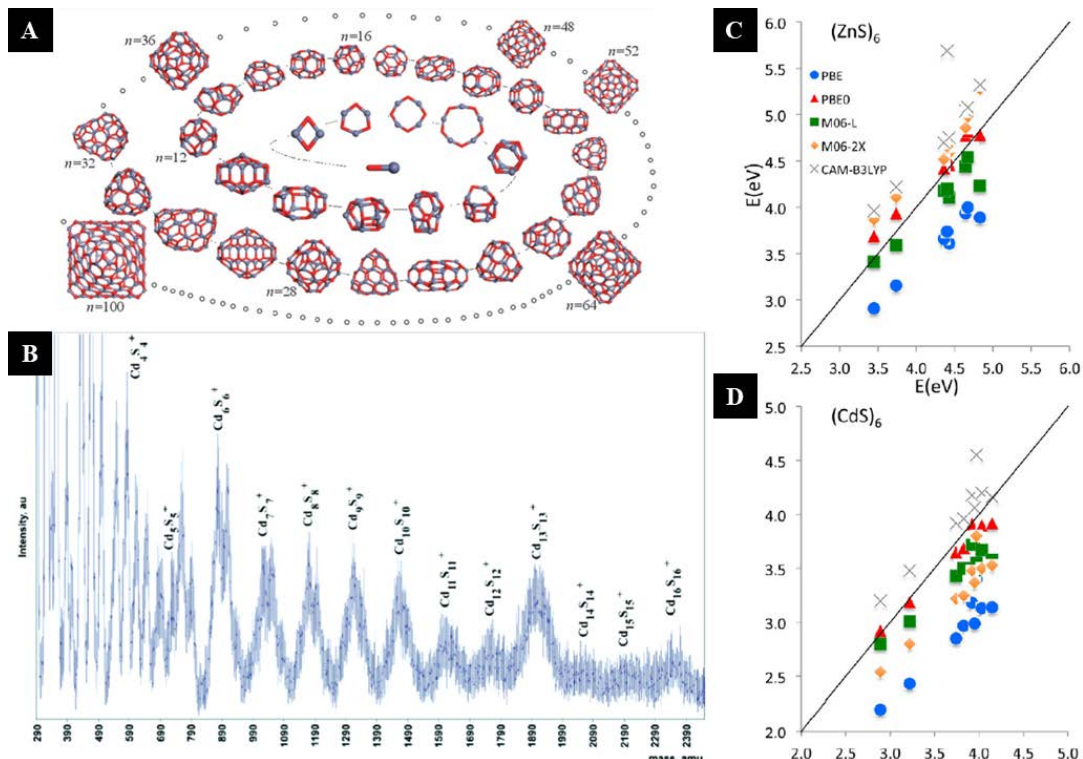
Fonte: A) Catlow et al. (2009), B) Sanville, Burnin e BelBruno (2005), C) e D) Azpiroz, Ugalde e Infante (2013)

Sendo assim, exemplificando a modelagem computacional de clusters aplicada no estudo de pontos quânticos, Azpiroz, Ugalde e Infante (2013) usaram clusters hexagonais de M_6X_6 (M = Cd, Zn e X = S, Se, Te) como modelos para pontos quânticos de estrutura wurtzita e avaliaram sua performance junto de vários funcionais de densidade e funções de base distintas (Figura 6-C e D), comparando com valores de referências obtidas pelos complexos e caríssimos cálculos de teoria *coupled clusters* no nível RI-CC2/def2-TZVPP. Por meio da avaliação, os autores mostraram que o modelo de clusters apresentam excelentes resultados por meio de um custo computacional muito mais baixo quando comparado com a metodologia de referência, sendo o funcional híbrido PBE0, o melhor na descrição da estrutura eletrônica e dos modos vibracionais dos sistemas (AZPIROZ; UGALDE; INFANTE, 2014).

Figura 7 – A) Caminho de reação e estruturas intermediárias na formação de ZnS cúbico e hexagonal. B) Modos vibracionais teóricos de infravermelho (esquerda) e Raman (direita) de clusters de Zn$_4$S$_4$ (azul) e Zn$_6$S$_6$ (vermelho). C) Densidade de estados e orbitais HOMO e LUMO de clusters de Zn$_4$S$_4$ (esquerda) e Zn$_6$S$_6$ (direita)
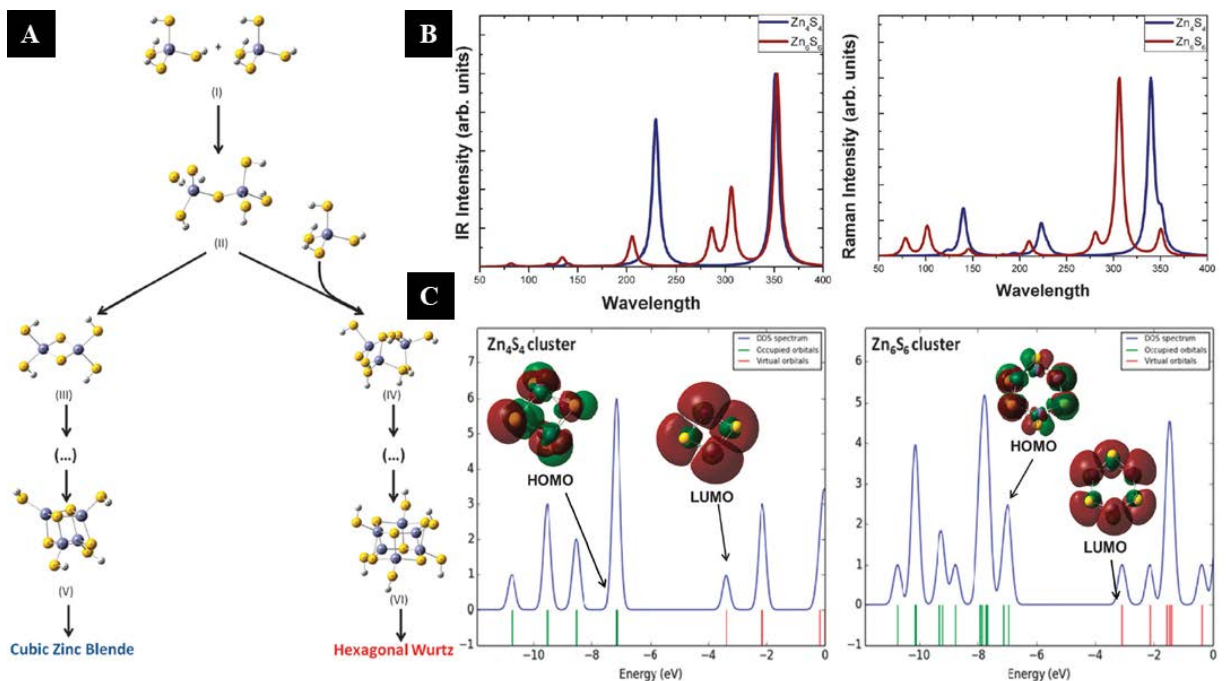
Fonte: La Porta et al., 2014

Em outro exemplo, La Porta et al. (2014) utilizaram clusters hexagonais e cúbicos (M_4X_4) como modelos para pontos quânticos de ZnS, propondo e investigando um mecanismo de crescimento de nanopartículas (Figura 7-A) e o controle de fase das estruturas blenda de zinco e wurtzita por meio do surfactante tetrabutilamônio em

uma metodologia teórico-experimental. Além disso, por meio da DFT dependente de tempo (TDDFT), os autores também identificaram os modos vibracionais no infravermelho e Raman das nanopartículas (Figura 7-B), a densidade de estados eletrônicos e o formato dos orbitais de fronteira HOMO e LUMO (Figura 7-C), demonstrando propriedades eletrônicas em acordo com a literatura (LA PORTA et al., 2014a). Portanto, a escolha cuidadosa de metodologias junto de modelos adequados pode levar a resultados promissores em ambos os estudos experimentais e teóricos, como apresentado pelos autores citados neste capítulo.

2.3. QTAIM e NBO

Embora a DFT por si só seja capaz de descrever a estrutura eletrônica de sistemas químicos adequadamente, algumas teorias podem ser complementadas aos métodos computacionais ao abordar especificidades dos sistemas. Como é sabido, toda informação relevante de um sistema está contida em suas funções de onda, permitindo a utilização das funções de ondas e orbitais atômicos e moleculares dos sistemas descrevidos teoricamente na elucidação estrutural dos sistemas químicos. No caso da DFT, por meio da densidade eletrônica e das populações de um sistema, é possível realizar análises da natureza das ligações químicas usando das teorias QTAIM e NBO (BADER, 1991; FOSTER; WEINHOLD, 1980).

Na teoria da QTAIM, a densidade eletrônica molecular ρ é usada na execução de integrações com o gradiente $\nabla\rho$ sendo a condição determinante da topologia (OLIVEIRA; ARAÚJO; RAMOS, 2010; POPELIER, 2000). Assim, considerando átomos de camada aberta e restringindo condições de contorno na superfície molecular, Bader mostrou que o fluxo da densidade eletrônica é nulo em qualquer ponto da superfície, sendo o gradiente perpendicular a uma normal a superfície (BADER, 1985; NASERTAYOOB; SHAHBAZIAN, 2008; OLIVEIRA; ARAÚJO; RAMOS, 2010). Logo, todas as linhas de contorno da densidade eletrônica são obtidas de uma sequência de gradientes $\nabla\rho$ bem definidas em pontos espaciais chamados de atratores (KEITH; BADER; ARAY, 1996; OLIVEIRA; ARAÚJO; RAMOS, 2010). Uma vez que o gradiente da densidade eletrônica é uma função dos seus atratores, estes são os núcleos do sistema e, quando considerado todos os atratores nucleares, o conjunto de linhas de contorno do gradiente formam o próprio sistema de

camada aberta traduzida como o átomo (MOHALLEM, 2002; OLIVEIRA; ARAÚJO; RAMOS, 2010).

Em moléculas, as trajetórias do gradiente de densidade se juntam para descrever o sistema químico a partir de pontos críticos localizados entre atratores (O'BRIEN; POPELIER, 1999; OLIVEIRA; ARAÚJO; RAMOS, 2010). Assim, quando duas trajetórias do gradiente direcionadas aos núcleos são formadas por um único ponto crítico de ligação, são resultadas em linhas interatômicas ou trajetórias de ligações, cujo a localização do ponto crítico de ligação é feita pelo laplaciano da densidade eletrônica $\Delta^2\rho$ (BADER, 1998; O'BRIEN; POPELIER, 1999; OLIVEIRA; ARAÚJO; RAMOS, 2010; POPELIER, 1999). De forma simples, quando uma trajetória de ligação interliga dois atratores, há a presença de uma ligação química entre os dois núcleos (BADER, 1998; OLIVEIRA; ARAÚJO; RAMOS, 2010).

Com isso, o laplaciano $\Delta^2\rho$ pode ser utilizado como parâmetro de modelagem topológica de ligações químicas junto com dados sobre os pontos de ligações críticos, elipicidade e autovalores de matrizes Hessianas, fornecendo informações como o caráter de ligação covalente ou insaturada usados na determinação da estabilidade molecular, ressonância e força interatômica pela QTAIM (ALCOBA et al., 2006; ALSBERG; MARCHAND-GENESTE; KING, 2000; OLIVEIRA; ARAÚJO; RAMOS, 2010; PALUSIAK; GRABOWSKI, 2004; RODE; DOBROWOLSKI, 2007). Assim, o laplaciano da densidade eletrônica pode levar a informações extremamente importantes na elucidação estrutural e das ligações dos sistemas químicos (FRADERA; AUSTEN; BADER, 1999; OLIVEIRA; ARAÚJO; RAMOS, 2010).

Por exemplo, considerando o sinal do laplaciano $\Delta^2\rho$ em uma determinada zona de ligação, a densidade eletrônica é acumulada nos pontos críticos de ligação químicas quando $\Delta^2\rho < 0$, ou nos núcleos atômicos quando $\Delta^2\rho > 0$ (BADER; NGUYEN-DANG; TAL, 1981; GRABOWSKI et al., 2006; OLIVEIRA; ARAÚJO; RAMOS, 2010). Essa relação é justificada pelo teorema virial da densidade eletrônica total conforme a equação (11), logo podendo relacionar as energias cinética (K) e potencial (U), respectivamente, com depressões e concentrações de densidade eletrônica (BADER, 1988; BADER; BEDDALL, 1972; OLIVEIRA; ARAÚJO; RAMOS, 2010). Portanto, para $\Delta^2\rho > 0$ (K) são caracterizadas interações intra- ou intermoleculares, enquanto $\Delta^2\rho < 0$ (U) são ligações covalentes ou insaturadas (FILHO et al., 2007; MATTA; BOYD, 2007; OLIVEIRA; ARAÚJO; RAMOS, 2010;

VENER et al., 2007). Essas informações são muito relevantes na determinação de caráter covalente ou iônico, como será visto no artigo sobre nanopartículas de ZnS e ZnO.

$$\nabla^2\rho = 2K + U$$

(11)

Uma segunda teoria como forma complementar aos estudos da DFT é a teoria do NBO proposta por Weinhold, no qual é considerado um conjunto de bases transformado a partir da função de onda inicial para o formato de NBO, sendo representante das ligações localizadas e pares isolados similar a estrutura natural de Lewis (BIHAIN et al., 2020; FOSTER; WEINHOLD, 1980; GLENDENING; LANDIS; WEINHOLD, 2012). Essa teoria permite avaliar os efeitos de deslocalização eletrônica de átomos ou grupos atômicos, prevendo fenômenos de hibridização, efeitos estéricos e, como será visto no trabalho sobre nanopartículas de ZnO e ZnS, a transferência de cargas entre orbitais (BIHAIN et al., 2020; GLENDENING; LANDIS; WEINHOLD, 2012).

Nessa teoria, os NBOs são calculados com ocupação eletrônica máxima, com conversão consistente de uma função de onda inicial de orbitais atômicos para outras funções seguindo as sequências de conjuntos: orbitais naturais atômicos (*Natural Atomic Orbitals*, NAOs), orbitais naturais híbridos (*Natural Hybrid Orbitals*, NHOs), NBOs e orbitais moleculares naturais localizados (*Natural Localized Molecular Orbitals*, NLMOs) interpostos aos orbitais atômicos e moleculares, sendo cada orbital do conjunto posterior formado pela combinação dos orbitais de um conjunto anterior (BIHAIN et al., 2020; GLENDENING; LANDIS; WEINHOLD, 2012).

Quando um conjunto é localizado, esse pode ser transformado em orbitais naturais localizados ou retornar para forma de orbitais moleculares originais, resultando nos orbitais ocupados em múltiplas direções antiligantes e de Rydberg que agem como armazenadores de transferência de cargas descritas pela densidade eletrônica (BIHAIN et al., 2020; GLENDENING; LANDIS; WEINHOLD, 2012; VOROBYOV; YAPPERT; DUPRÉ, 2002).

No entanto, alguns NBOs não aderem a estrutura natural de Lewis, nos quais são responsáveis por descrever os efeitos de deslocalização eletrônica (BIHAIN et al., 2020). Essas deslocalizações são analisadas de forma quantitativa pela remoção dos

orbitais antiligantes e de Rydberg, resultando em estruturas de Lewis idealizadas que podem dar informações sobre a contribuição de efeitos estéricos, hiperconjugativos e a força de interação e deslocamento de carga por uma análise de energia de perturbação de segunda ordem (BIHAIN et al., 2020; GLENDENING; LANDIS; WEINHOLD, 2012; VOROBYOV; YAPPERT; DUPRÉ, 2002).

2.4. Ancoragem Molecular

Saindo dos métodos químico-quânticos e seguindo outra vertente de cálculos computacionais, é encontrado uma categoria muito importante de metodologias computacionais conhecida como modelagem molecular, permitindo a investigação de estruturas e propriedades de moléculas e macromoléculas e sendo extremamente popular em campos derivados da Bioquímica e Farmacêutica (ASSIS et al., 2021a, 2021b; DE JESUS et al., 2021). Entre os métodos de modelagem molecular, a ancoragem molecular tem recebido destaque principalmente em estudos de desenvolvimento de fármacos devido a sua importante capacidade de prever a orientação de ligantes em proteínas e enzimas receptoras (ASSIS et al., 2021a, 2021b; DE JESUS et al., 2021; DIAS; DE AZEVEDO JR., 2008; FAN; FU; ZHANG, 2019; PAGADALA; SYED; TUSZYNSKI, 2017).

A ancoragem molecular é definida como um método de simulação computacional com foco em encontrar a melhor conformação de moléculas a partir de uma configuração prévia e complementariedades, de modo a prever a maneira e a afinidade no qual um ligante e um receptor estão em interação, quantificadas em um escore pelo formato molecular e das interações interatômicas envolvidas (FAN; FU; ZHANG, 2019; PAGADALA; SYED; TUSZYNSKI, 2017). Geralmente a ancoragem molecular é dividida em dois métodos conhecidos como ancoragem rígida e por ajuste induzido (DIAS; DE AZEVEDO JR., 2008; FAN; FU; ZHANG, 2019; PAGADALA; SYED; TUSZYNSKI, 2017).

No modelo de ancoragem rígida proposto por Fischer, é tomado em consideração o conceito clássico de chave-fechadura visto em processos enzimáticos (PAGADALA; SYED; TUSZYNSKI, 2017). No contexto do modelo, é realizada a ancoragem rígida de receptores e ligantes para buscar e avaliar uma orientação preferencial cujo uma chave (ligante) abre uma fechadura (receptor), enfatizando a complementaridade geométrica (FAN; FU; ZHANG, 2019). Em contrapartida, no

modelo mais complexo de ancoragem por ajuste induzido sugerido por Koshland, ambos os receptores e ligantes são flexíveis e mudam suas conformações para acomodar o acoplamento durante a interação (FAN; FU; ZHANG, 2019; PAGADALA; SYED; TUSZYNSKI, 2017).

Como citado brevemente, os métodos de ancoragem molecular geralmente aplicam uma função de escore baseada na energia com intuito de identificar a conformação mais energeticamente favorável de um ligante, cujo escores de menor energia representam melhor a ligação a um receptor em comparação a valores mais energéticos (THOMSEN; CHRISTENSEN, 2006). A função de escore implementada no *software Molegro Virtual Docking* usado em nossos estudos é baseada em um potencial linear por partes (PLP), sendo estes potenciais simplificados com parâmetros ajustados para estruturas proteínas-ligantes e contando com a direcionalidade das ligações de hidrogênio (DE CASTRO et al., 2022; THOMSEN; CHRISTENSEN, 2006). Assim, a função de escore da ancoragem é dado pela equação (12) (THOMSEN; CHRISTENSEN, 2006).

$$E_{escore} = E_{inter} + E_{intra}$$

(12)

$$E_{inter} = \sum_{i \varepsilon ligante} \sum_{j \varepsilon proteina} \left[E_{PLP}(r_{ij}) + 332{,}0 \frac{q_i q_j}{4 r_{ij}^2} \right]$$

(13)

$$E_{intra} = \sum_{i \varepsilon ligante} \sum_{j \varepsilon ligante} E_{PLP}(r_{ij}) + \sum_{flexixel} A[1 - \cos(m.\theta - \theta_0)] + E_{choque}$$

(14)

Como pode ser visto, a função de escore é dividida em dois termos representando as energias inter- e intramoleculares, evidenciadas pelas equações (13) e (14), respectivamente (DE CASTRO et al., 2022; THOMSEN; CHRISTENSEN, 2006). Como a função de escore é baseada em PLP, essa energia é dividida em dois parâmetros, havendo um potencial interpretando a aproximação do termo estérico entre átomos (interações de Van der Waals) e outro para as ligações de hidrogênio (DE CASTRO et al., 2022; THOMSEN; CHRISTENSEN, 2006). Em questão ao termo da energia interna, a primeira parte da equação envolve todos os pares de átomos do ligante, com exceção dos conectados por duas ligações; o segundo termo denomina

a energia torcional, tal qual θ é o ângulo de torsão da ligação; enquanto o terceiro termo é uma penalidade aplicada pela presença de átomos pesados separados por distâncias menores que 2,0 Å (DE CASTRO et al., 2022; THOMSEN; CHRISTENSEN, 2006).

Portanto, a ancoragem baseada nas complementaridades geométrica e energética e na configuração prévia permite alcançar uma estrutura mais estável por meio da minimização da energia livre (FAN; FU; ZHANG, 2019). Dessa forma, os modelos de ancoragem molecular aliada a comparações críticas com estruturas cristalinas presentes em bancos de dados como *ChemDB* e *PubChem* alavancaram o desenvolvimento de fármacos e reduziram o custo econômico e de tempo no qual seriam gastos em estudos experimentais, destacando a velocidade e precisão dos modelos de ancoragem (DIAS; DE AZEVEDO JR., 2008; FAN; FU; ZHANG, 2019; PAGADALA; SYED; TUSZYNSKI, 2017).

3. METODOLOGIA

Em ambos os trabalhos apresentados, foi utilizado clusters hexagonais de configuração M_6X_6 (M = Zn, Cd, X = S, O) como modelo para pontos quânticos semicondutores de estrutura wurtzita. A modelagem dos clusters foi realizada com base no trabalho de La Porta et al. (2014), no qual a estrutura local foi retirada por corte de parte de uma rede cristalina wurtzita, como apresentado na Figura 8 retirada do trabalho de Catlow et al. (2009), demonstrando a diferença de energia e tamanho entre clusters e suas configurações *bulk*. Assim, esses modelos foram submetidos a cálculos computacionais no pacote de Química Quântica *Gaussian 09* (J. FRISCH et al., 2009), no estado gasoso, enquanto os dados foram visualizados no *software GaussView* (DENNINGTON; KEITH; MILLAM, 2016), usando mapas de orbitais moleculares e potenciais eletrostáticos com valores de contorno igual a 0,0300 e 0,0004, respectivamente. Já os espectros de densidade de estados foram obtidos no *software GaussSum* (O'BOYLE; TENDERHOLT; LANGNER, 2008).

Figura 8 – Diferença de energia total E_b de clusters de Zn_nO_n no estado fundamental e na forma bulk de wurtzita e *rocksalt* em função inversa da formula unitária n, sendo n_c a transição entre duas configurações
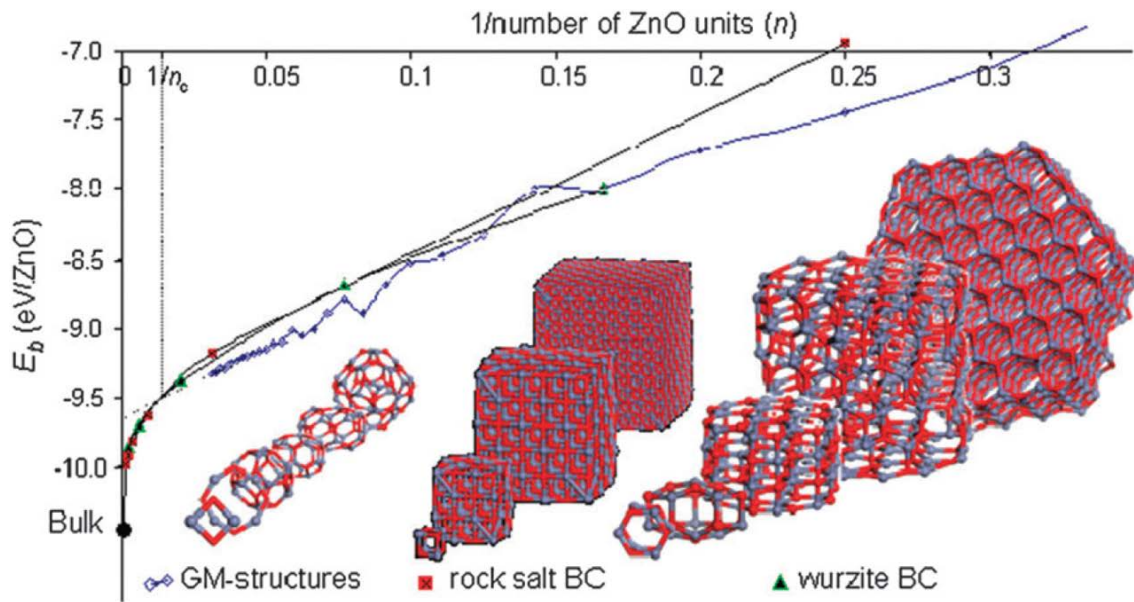
Fonte: Catlow et al. (2009)

Assim, no primeiro trabalho com clusters de $Zn_{6-x}Cd_xS_6$, estruturas híbridas foram modeladas por meio da troca de íons de Zn^{2+} do cluster original de Zn_6S_6 por Cd^{2+} e seguindo o caminho de menor energia. Todos os cálculos foram feitos no nível

B3LYP/3-21G, obtido assim as geometrias, estruturas eletrônicas, propriedades vibracionais e ópticas. Para simular as estruturas deformadas sob uma corrente gerada por eletrodos de dispositivos baseados em pontos quânticos, um campo elétrico externo foi aplicado na direção do eixo x dos clusters com intensidades de 0, 0,05142, 0,10284, 0,20568, 0,41136 e 0,82272 V $Å^{-1}$.

No segundo trabalho sobre nanopartículas de ZnO e ZnS como materiais para aplicação em revestimento antimicrobiano, a metodologia foi dividida em três partes. A primeira parte, a experimental, se resume a síntese de nanopartículas de ZnO e ZnS por meio da rota hidrotérmica sob 160 °C por 120 minutos, utilizando um reator de Teflon com as misturas precursoras e tecidos de algodão. A síntese do ZnO foi feita ao misturar e submeter nas condições acima uma solução de acetato de zinco (7,34, 3,68 e 1,84 mmol) em 80 mL de água com 3 mL de hidróxido de amônio. Já a síntese do ZnS foi realizada ao misturar uma solução pré-aquecida a 80 °C de acetato de zinco (7,34, 3,68 e 1,84 mmol) e hidróxido de butilamônio (16,00 mmol) em 25 mL de etileno glicol com uma solução de tioureia (7,34 mmol) em 25 mL de etileno glicol e também submeter sob as condições acima.

As caracterizações foram feitas após lavagem e secagem dos tecidos por instrumentos de difração de raios X, espectrofotômetro de UV-Vis e microscopia eletrônica de varredura, enquanto a análise de fotocatálise por exposição a um fotoreator com lâmpada UVC de amostras preparadas sob mergulho em solução de 10 mg L^{-1} de azul de metileno por 60 minutos.

A segunda parte do trabalho consta os cálculos químico quânticos. De maneira similar ao primeiro trabalho, clusters hexagonais de Zn_6O_6 e Zn_6S_6 foram selecionados como modelos para os sistemas ZnO e ZnS wurtzita e aplicados a cálculos no nível B3LYP/6-31+G(d,p). No estudo dos estados excitados, foram feitas simulações TDDFT com palavra-chave $root$ = 2, sendo a transferência de carga entre estados excitados analisadas por cálculos $single$-$point$ com populações NBO. Em contraste com o primeiro trabalho, os mapas de potenciais eletrostáticos foram obtidos por cálculos de Hartree-Fock no nível teórico MP2 com cargas pelo método CHELPG (*Charges from Electrostatic Grid Based*). Em adição, cálculos baseados na QTAIM foram usados na análise da natureza das ligações químicas no nível B3LYP/6-31+G(d,p) pelo programa *AIM* (O'BOYLE; TENDERHOLT; LANGNER, 2008).

Na terceira parte é destacada os cálculos de ancoragem molecular realizadas pelo programa *Molegro Virtual Docker* (O'BOYLE; TENDERHOLT; LANGNER, 2008),

usando de procedimentos documentados pelo grupo de pesquisa com a geração de 30 poses (conformações e orientações) (GUIMARAES et al., 2011; MATOS et al., 2011; SILVA et al., 2015). Os conjuntos de dados da estrutura cristalina da enzima protease principal do SARS-CoV-2, cutinase do *Fusarium solani* e DNA girasse da *Escherichia coli* foram obtidos no banco de dados *Protein Data Bank* com cartões PDB ID: 5R82, 1XZL e 1KZN, respectivamente (BERMAN et al., 2000; LAFITTE et al., 2002; LONGHI et al., 1996). Já a Mpro mutante R60C (KHAN et al., 2020) foi preparada pela adição de mutações pontuais no *software Discovery Studio* (ACCELRYS SOFTWARE, 2012) e minimizada no *Swiss PDB viewer* (https://spdbv.vital-it.ch/). Por fim, os valores teóricos da dose letal (LD50) foram calculadas pelo modelo ADMET (http://biosig.unimelb.edu.au/pkcsm/prediction).

4. ARTIGO 1: THEORETICAL INVESTIGATION ON THE EFFECTS OF ELECTRIC FIELD ON THE ELECTRONIC STRUCTURE AND SPECTROSCOPIC PROPERTIES OF $Zn_{6-x}Cd_xS_6$ CLUSTERS AS MODEL SYSTEMS OF SEMICONDUCTOR QUANTUM DOTS

4.1. Introduction

Semiconductor quantum dots (QDs) based nanomaterials, exhibiting sizes raging of 1 to 20 nm, have attracted noteworthy attention in many technologies, mainly due to their outstanding size-dependent properties confined in all three-dimensions (KOVALENKO et al., 2015; MURRAY; KAGAN; BAWENDI, 2000; TALAPIN et al., 2010). Because of this, they present similar molecule-like electronic structure properties. It is worth mentioning that due to their enormous complexity of the QDs systems that having the atomic-order limited to the nanoscale, in particular, represents a substantial obstacle to the full elucidation of their chemical and spectroscopic behavior. In this regard, computational methodologies are potent tools to obtain insights into the electronic structure and spectroscopic properties of the QDs systems. Such strategies offer great opportunities for solving diverse problems at the nanoscale, many of which can, in principle, be experimentally inaccessible. Among the theoretical methods, the Density Functional Theory (DFT) has proven been an essential tool in the understanding of nanoscale phenomena, interpretation, and explanation of diverse experimental data, as well as the discovery of new and more efficient materials (AZPIROZ et al., 2012; AZPIROZ; UGALDE; INFANTE, 2014; BURNIN; SANVILLE; BELBRUNO, 2005; HE-YING et al., 2008; KRAINARA et al., 2013; LA PORTA et al., 2014a, 2014b, 2017; OUENDADJI et al., 2011; PEGU et al., 2018; RAUBACH et al., 2013; SANVILLE; BURNIN; BELBRUNO, 2006; ZHAO; TRUHLAR, 2008).

As yet, the zinc sulfide (ZnS) and cadmium sulfide (CdS) are undoubtedly one of the most explored QDs systems, and due to their outstanding functional properties, which make them suitable for a wide range of light-emitting diodes, photovoltaic cells, photodetectors, biomedical and catalytic applications (BAE et al., 2009; BANSAL et al., 2016; DENG; LI, 2014; LA PORTA et al., 2014a, 2014b, 2017; RAUBACH et al., 2013; REGULACIO et al., 2013; WANG et al., 2012; ZHU et al., 2018). From a structural point of view, both ZnS and CdS, in terms of the chemical structure, have a very similar polymorphism. For instance, such systems crystallizing on hexagonal wurtzite, the cubic zinc blende, and, more rarely, the rock-salt structure (which is

usually observed in high pressures) (ACHARYA; DARULKAR; CHOUDHARY, 2013; LA PORTA et al., 2014a). For this reason, most studies are focused mainly on hexagonal wurtzite and cubic zinc blende forms for both ZnS and CdS materials. In the case of ZnS, it is well-known that the cubic zinc blende structure is the most thermodynamically stable phase in bulk; however, with the decrease of particle size, there is a stability shift towards wurtzite structure, which makes possible the production of wurtzite ZnS nanocrystals at low temperatures (HUANG; BANFIELD, 2005; LA PORTA et al., 2014a; SUN et al., 2008; TONG et al., 2007; ZHAO et al., 2004). On the other hand, unlike ZnS, the hexagonal wurtzite CdS structure is the most thermodynamically stable phase (BANERJEE et al., 2000; TAN; LI; JI, 2011). However, in this case, it is well known in the literature that CdS can adopt both hexagonal wurtzite and cubic zinc blende phases under ambient conditions (BANERJEE et al., 2000; TAN; LI; JI, 2011). Diverse synthesis routes with controlled phases, particle-sizes, composition, and morphologies have widely been reported to obtaining of both ZnS and CdS nanocrystals (LA PORTA et al., 2014a; XU et al., 2007). As shown in previous works, the Zn_nS_n and Cd_nS_n clusters with n = 3, 6, and 13 ZnS or CdS monomer units are the most stable, and their existence was confirmed utilizing time-of-flight mass spectrometry (BURNIN; SANVILLE; BELBRUNO, 2005; HE-YING et al., 2008; SANVILLE; BURNIN; BELBRUNO, 2006). As such, the Zn_6S_6 and Cd_6S_6 clusters are adequate as model systems of QDs to represent the hexagonal wurtzite structure (AZPIROZ; UGALDE; INFANTE, 2014; BURNIN; SANVILLE; BELBRUNO, 2005; HE-YING et al., 2008; LA PORTA et al., 2014a; NASRAOUI et al., 2019; ZWIJNENBURG; ILLAS; BROMLEY, 2011).

Therefore, in the current study, we report the effects of an external electric field on the electronic structures and spectroscopic properties of $Zn_{6-x}Cd_xS_6$ clusters as model systems of QDs in hexagonal wurtzite structure. Consequently, this leads to the order-disorder effects on the surface states in the functional properties of $Zn_{6-x}Cd_xS_6$ clusters, which is responsible for energy shifts such as in the electronic band gap and the excitonic peaks, known as the quantum Stark effect.

4.2. Methodology

In this study, we have performed DFT and single-point time-dependent DFT (TDDFT) calculations at the B3LYP/3-21G level on the structure, vibrational frequency,

optical and electronic calculations, with and without the effect of an external electric field (0, 0.05142, 0.10284, 0.20568, 0.41136, 0.82272 V Å^{-1}) applied along the x-direction of the $Zn_{6-x}Cd_xS_6$ clusters as model systems of QDs in hexagonal wurtzite structure. Particularly, we choose to apply the electric field along the x-axis to simulate the pathway of the current from electrodes in devices based on such QDs. As such, the change of Zn^{+2} to Cd^{+2} atoms in the cluster structure has a significant impact on their electronic structure and spectroscopic properties of QDs systems under investigation. Figure 9 shows the most stable optimized structure obtained for $Zn_{6-x}Cd_xS_6$ clusters. The thermodynamic properties of these $Zn_{6-x}Cd_xS_6$ clusters are shown in the Supplementary information. These results demonstrate that the Zn_6S_6 cluster has higher stability than the Cd_6S_6 cluster.

It should be emphasized that in this type of simulation, the computational level used has a direct impact on the quality of the results obtained. Regarding the hybrid exchange–correlation functionals such as the B3LYP, they are known for leading to deficient atomization energies, especially in the case of metallic systems, presenting a deviation around 25 to 40% (LA PORTA et al., 2011; PAIER et al., 2006; PAIER; MARSMAN; KRESSE, 2007; RAMALHO; TAFT, 2005). However, for this system, previous work in the literature has shown that the B3LYP functional is suitable and presents a good agreement with experimental data (AZPIROZ et al., 2014; LA PORTA et al., 2014a; ZWIJNENBURG et al., 2011). Also, Azpiroz et al. (2014) in its benchmark study for DFT calculations of MX clusters (M = Zn and Cd; X = O, S, Se, and Te) as model systems of QDs, in particular, showed that a small and large base set leads to similar results for title models. Hence, it should be noted that the proposed methodology in the current paper, in which the general behaviors observed was consistent in the entirety of the work as well as in agreement with the literature, have wide satisfactory results. Molecular orbitals (MOs) images were acquired through GaussView with a contour value of 0.03, and the density of states (DOS) spectra was obtained using GaussSum (FRISCH et al., 2009; O'BOYLE; TENDERHOLT; LANGNER, 2008). All of DFT and TDDFT calculations were evaluated in the gas phase through the Gaussian 09 package (FRISCH et al., 2009).

Figure 9 - Optimized geometry of the most stable $Zn_{6-x}Cd_xS_6$ clusters from a side and top view
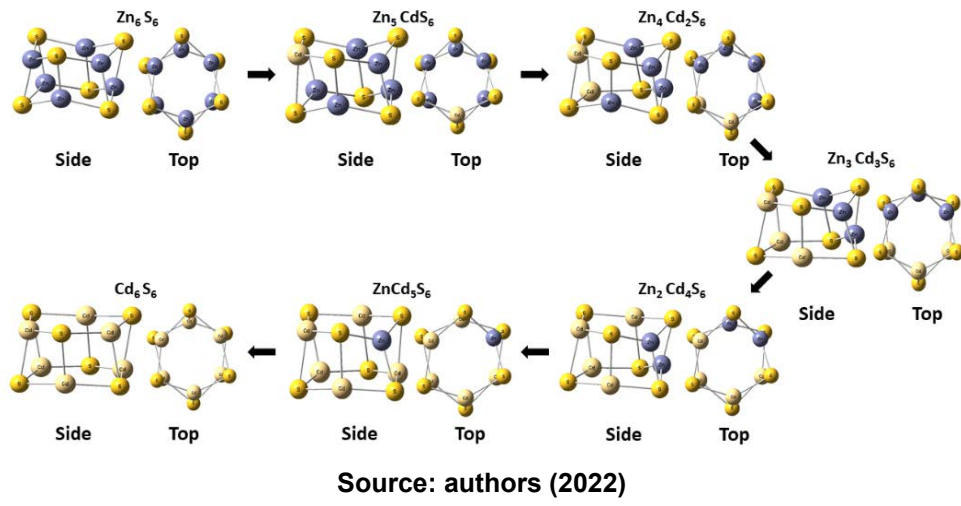
Source: authors (2022)

4.3.   Results and Discussions

Here we have focused on understanding the influence of the electric field on their structural, vibrational, optical, and electronic properties of the $Zn_{6-x}Cd_xS_6$ clusters as model systems of QDs in hexagonal wurtzite structure. Along this line, we first performed a detailed structural analysis for the most stable $Zn_{6-x}Cd_xS_6$ clusters. As expected, the compositional modulation of $Zn_{6-x}Cd_xS_6$ clusters leads to significant differences in bonding angles and lengths.

Figure 10 shows the Zn_6S_6, $Zn_3Cd_3S_3$, and Cd_6S_6 clusters as representative structures for our structural discussion. In the case of Zn_6S_6 cluster (Figure 10-A), it is possible to observe two Zn-S bond lengths of about 2.324 Å and 2.385 Å, respectively. On the other hand, this observation also suggests that the present model is adequate to represent a hexagonal structure. Additionally, a higher angle around 109° and a lesser angle of about 66° are also observed for this structure. The computed Zn-S bond lengths are in accordance with other theoretical works and experimental values (~2.34 Å) for ZnS (AZPIROZ et al., 2012; BURNIN; SANVILLE; BELBRUNO, 2005; LA PORTA et al., 2014a; WANG; DUKE, 1987). However, with an increasing Cd content in the cluster has been observed changes in the local structure of QDs systems. For example, for the case of $Zn_3Cd_3S_6$ cluster (see Figure 10-B), it is observed a small increase in the horizontal bond lengths, 2.325-2.329 Å, and greater in the vertical bonds, 2.377-2.395 Å in the extremity of ZnS. In contrast, the angles are unchanged to the Zn_6S_6 cluster. On the other hand, as for the CdS extremity, is found a slight

decrease in the horizontal bond lengths, 2.576-2.581 Å, and major shifts in the vertical bonds, 2.690-2.734 Å. The bond angles for the CdS part is close to the precursor structure as well. As such, the horizontal and vertical Zn-S-Cd bonds are of 2.319 and 2.394 Å for Zn-S and about 2.581 and 2.690 Å for Cd-S, respectively. Similarly, for the $Zn_3Cd_3S_6$ cluster, the angles are approximately 112° and 95°, respectively, for S-Zn-S and S-Cd-S in the interface of both parties, while the lesser angles are of 72°. These structural changes (in the bond lengths and angles) with increasing Cd content are likely due to their difference in atomic radius. This leads to a highly polarized Zn-S and Cd-S bond lengths and angles, presenting the most distorted cluster. On the other hand, in the case of the Cd_6S_6 cluster (see Figure 10-C), the horizontal and vertical Cd-S bond lengths of about 2.584 Å and 2.721 Å, respectively, in a nice agreement with experimental data (~2.52 Å) (HE-YING et al., 2008; PEGU et al., 2018; ROCKENBERGER et al., 1997; SANVILLE; BURNIN; BELBRUNO, 2006). Additionally, this cluster structure has a higher angle of 99° and lower of approximately 76°, respectively. However, from these results, we can see that the angles of this Cd_6S_6 cluster are closer to the right angle. Therefore, based on this information, we believe that this structure can in principle be more easily transformed into a cubic system. In practice, under ambient conditions, it is well-known that the CdS can exist in both forms, i.e., hexagonal wurtzite and cubic zinc blende.

Herein, to better inspect structural changes induced by the presence of an applied external electric field, in this study, the difference between the orbital density was plotted in Figure 10-A to C. Hence, the electric field applied along the x-direction is responsible for induced a higher polarization in these QDs. As is well-known, these effects will become more pronounced as the cluster size increases, mainly due to the quantum Stark effect (EMPEDOCLES, 1997). Also, the structural polarization of these QDs, leads to a change in their electronic structure and spectroscopic properties significantly. As such, the effects of the electric field are most visible during the compositional modification of these QDs due to their heterogenic structure, clearly indicating a highly polarized Zn-S and Cd-S bond lengths and angles. Consequently, these clusters have a more distorted structure. It is worth notice that also was applied to an electric field above of 0.41 V Å^{-1}; however, as a result, we observed the cleavage of Zn-S and Cd-S bonds, as well as the cluster completely lost its structure. For this reason, these calculations were not considered in the present study.

Figure 10 - Illustration for optimized structures with and without the effect of an external electric field applied along the x-direction and the difference between the molecular orbital density for the A) Zn₆S₆, B) Zn₃Cd₃S₆ and C) Cd₆S₆ clusters. Inset in cluster structure the respective bond lengths from the front (F) and back (B) side
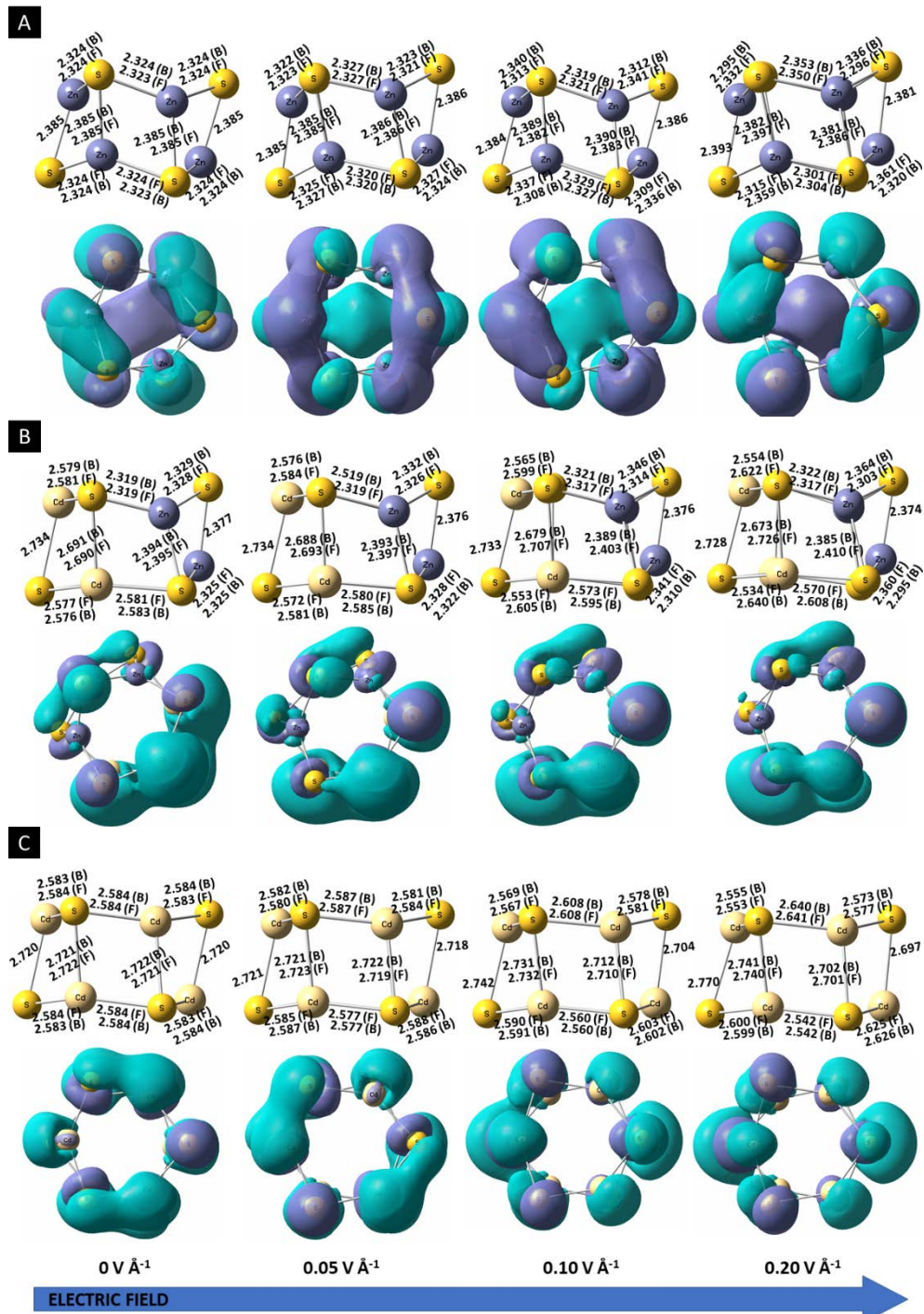
Moreover, the vibrational analysis reveals that for these Zn$_{6-x}$Cd$_x$S$_6$ clusters, all modes are positives confirmed a minimum of potential energy. Additionally, the

Raman spectra and their respective vibrational modes displacement for these $Zn_{6-x}Cd_xS_6$ clusters as a function of the electric field applied are shown in Figure 11-A to E. There are blue-shifts in Raman-active modes of the Zn_6S_6 cluster to Cd_6S_6 cluster, which is associated with structural changes (see Figure 11-A). Thus, this type of displacement is associated with an increase in bond length. By increasing Cd content in relation to the Zn_6S_6 cluster, in particular, an overlap of Raman-active modes can be identified. In this case, changes in the intensity and position of the Raman spectrum are directly related to compositional modulation that alters the cluster structure (see Figure 11-A). As such, the Raman spectra of the Zn_6S_6 cluster have also revealed a nice agreement with experimental and other theoretical data for ZnS QDs (CHENG et al., 2009; TRAJIĆ et al., 2015). Similarly, Raman spectra of the Cd_6S_6 clusters also are consistent with experimental results for the CdS QDs (GONG; KELLEY; KELLEY, 2017; SCHREDER et al., 2003). It is important to emphasize that alteration in the position of Raman-active modes, when compared to the literature, likely is due to the QDs diameters distinction. Additionally, the influence of the electric field in computed Raman spectra of $Zn_{6-x}Cd_xS_6$ clusters are illustrated in Figure 11-B to D.

However, the structural analyses suggest that the Cd_6S_6 cluster has likely a more symmetrical structure (see Figure 10-C). It is evident that this Cd_6S_6 cluster can be more easily polarized with the electric field, as shown in Figure 10-C and Figure 11-D. In parallel, the same principle can also be used to understand some spectral characteristics of these Cd-containing clusters under investigation (Figure 11-C). In general, such clusters are more sensitive to the magnitude of the applied electric field, as shown in Figure 11-C and D. Therefore, with the increase in the magnitude of the applied electric field, the intensity of the overlapped peaks located at 277 cm^{-1} for the $Zn_3Cd_3S_6$ cluster and the 268 cm^{-1} of Cd_6S_6 cluster is reduced significantly. Also, for the Cd_6S_6 cluster, the Raman-active mode at 268 cm^{-1} is split into two other peaks of higher and lower energy modes. Similarly, the overlapped peaks at 277 cm^{-1} for the $Zn_3Cd_3S_6$ cluster are separated and their intensity inverted, then being split into four total peaks with distinct energy modes with increasing of the magnitude of the electric field. Based on these results, it can be seen that ZnS QDs have a high resistance to the electric field, which is superior to CdS QDs. These results are consistent with the literature for both materials (RODRIGUEZ; GORDILLO, 1989).

Figure 11 - A) Computed Raman spectra for the Zn$_{6-x}$Cd$_x$S$_6$ clusters and effect of the electric field in Raman-active modes for the B) Zn$_6$S$_6$, C) Zn$_3$Cd$_3$S$_6$ and D) Cd$_6$S$_6$ clusters. E) The vibrational modes displacement for representative clusters. In this figure, the vectors are represented by blue arrows


Source: authors (2022)
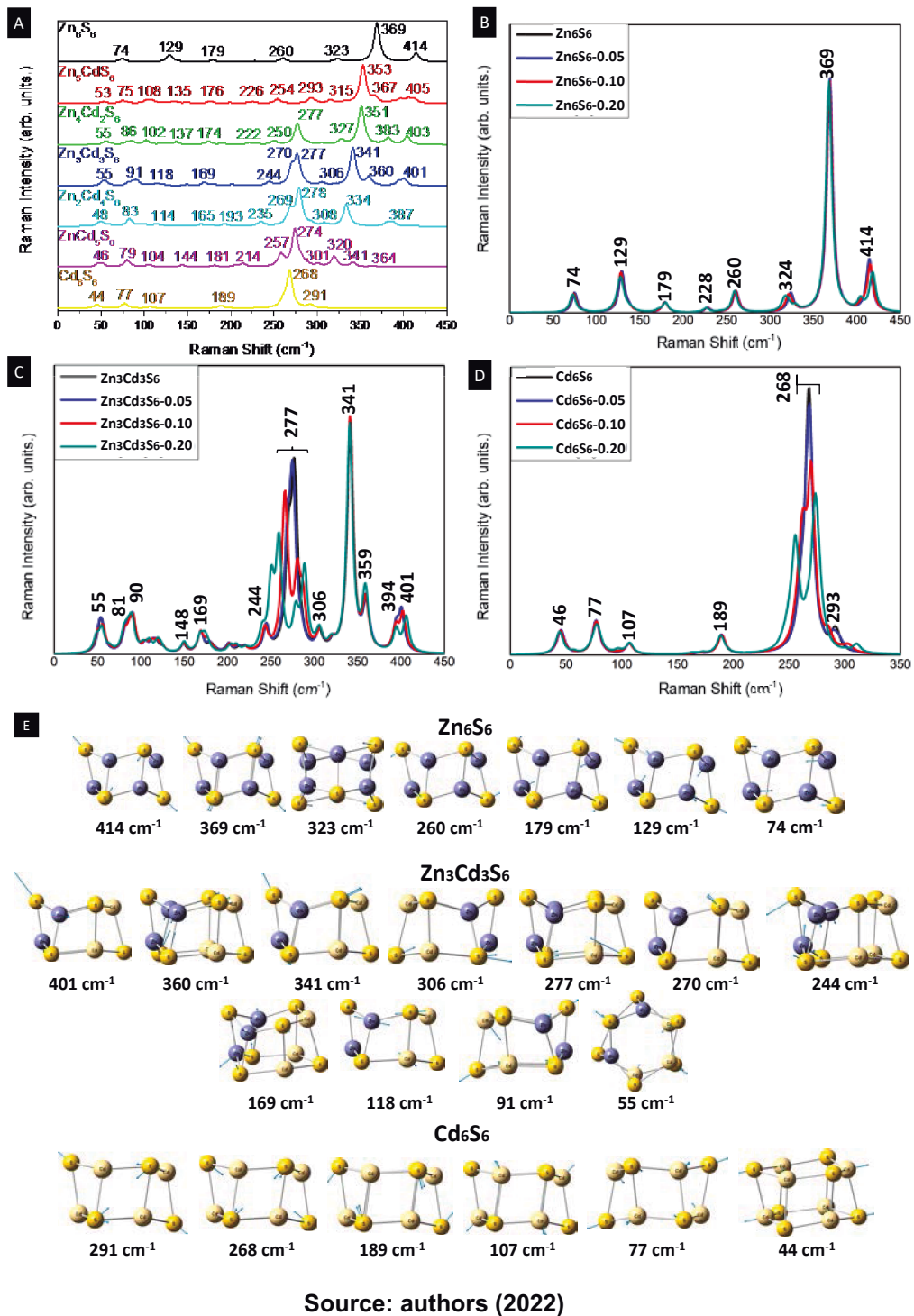
Figure 12-A shows the computed UV-Vis spectra for the Zn$_{6-x}$Cd$_x$S$_6$ clusters. As such, the replacement of Zn to Cd atoms leads to improved absorbance for these

clusters. Note that the increasing Cd content leads to a red-shift in UV-vis spectra, ranging from 345 nm (Zn_6S_6) to 448 nm (Cd_6S_6), due to bandgap value of ZnS (~3.6 eV) and CdS (~2.55 eV) (BURNIN; SANVILLE; BELBRUNO, 2005; FANG et al., 2011; HE-YING et al., 2008; LA PORTA et al., 2014a, 2014b, 2017; SHIN et al., 1991). For instance, Liu et al. (2013) has reported an absorption peak at 316 nm for ZnS QDs with a particle size of about 2.9 nm. Ye et al. (2016) has reported for CdS QDs of 5.0 nm an absorption peak at about 447 nm. These results are consistent with our computed results. Table 1 shows a summary of the excitonic transitions, their respective energies, and the exciton binding energy obtained from computed UV-vis spectra for these $Zn_{6-x}Cd_xS_6$ clusters. As can be seen in Table 1, the maximum absorption at approximately 345 nm (Zn_6S_6) and 448 nm (Cd_6S_6) can be assigned to the HOMO-2 → LUMO transitions. We note, for the other cases, that these absorption peaks are characterized by both lower energy HOMO-2 → LUMO and higher energy HOMO-3 → LUMO transitions, respectively. Additionally, the exciton binding energy for these $Zn_{6-x}Cd_xS_6$ clusters is shown in Table 1. Our results demonstrate that the first excitonic peak has a high oscillator strength, which is consistent for the calculated values of the exciton binding energy for these $Zn_{6-x}Cd_xS_6$ clusters. As such, the observed trend is consistent with the literature (BHARGAVA, 1997; CHEN et al., 2010; PARK; REYNOLDS, 1963; TRAN et al., 1997; YU et al., 2002). However, we anticipate that the use of a more robust and realistic model could achieve a better agreement between experimental data and theoretical estimate for this parameter.

Figure 12 – A) Computed UV-Vis spectra of $Zn_{6-x}Cd_xS_6$ clusters. B) Band alignment configurations for the different compositions investigated. The effect of the electric field in computed band alignment for C) Zn_6S_6, D) $Zn_3Cd_3S_6$ and E) Cd_6S_6
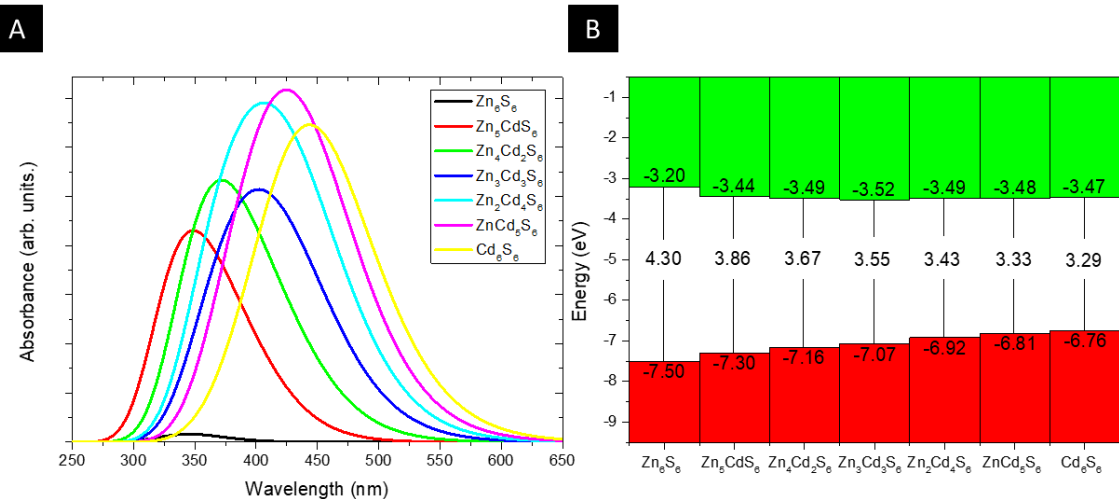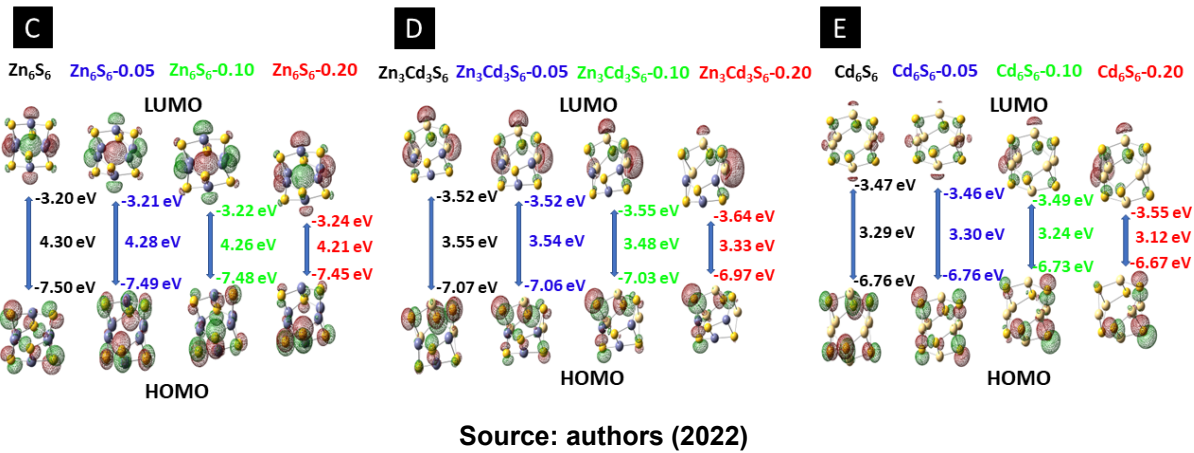
Source: authors (2022)

The computed band gaps and alignment of energy levels for the $Zn_{6-x}Cd_xS_6$ clusters, are shown in Figure 12-B. As expected, the electronic band gaps are also calculated from the HOMO and LUMO orbitals and decrease along with the increase of Cd content, ranging from 4.30 to 3.29 eV, respectively, for Zn_6S_6 and Cd_6S_6 clusters. Thereby, it is worth notice that the calculated band gaps are significantly higher than experimental values (BURNIN; SANVILLE; BELBRUNO, 2005; FANG et al., 2011; HE-YING et al., 2008; LA PORTA et al., 2014a, 2014b, 2017; SHIN et al., 1991). This likely is due to the base set and density functional used in this study. However, it is well-known that the band alignment levels, which is based on combination among two or more materials, has attracted enormous attention in recent years, especially towards the build of a variety of more efficient advanced materials for high-performance applications (GIAMPIETRI; DRERA; SANGALETTI, 2017; LANDMANN; RAULS; SCHMIDT, 2017; MAZZO et al., 2019; OLIVEIRA et al., 2017). Thus, in this perspective, this synergistic effect results in improved of their functional properties. The formation of the $Zn_{6-x}Cd_xS$ clusters as model systems of QDs, originate a band alignment of type-I for ZnS/CdS, in which the higher valence and conduction (VB and CB) bands of CdS are present within the energy gap of ZnS, possessing VB and CB offsets ranging from -0.20 to -0.74 eV and 0.24 to 0.32 eV, respectively (PETRYAYEVA; ALGAR; MEDINTZ, 2013). Similarly, a band alignment of reverse type-I is obtained for CdS/ZnS. As such, in this case, the lower bandgap of CdS is within the higher bandgap of ZnS, showing a VB and CB offset ranging from 0.05 to 0.74 eV and 0.05 to -0.27 eV, respectively (PETRYAYEVA; ALGAR; MEDINTZ, 2013). Nonetheless, the band alignments presented in the current work are in great agreement with the overall properties observed for the $Zn_{6-x}Cd_xS$ clusters, and with the

experimental data of ZnS/CdS and CdS/ZnS core/shell heterostructures reported in the literature as well (SAMADI-MAYBODI; SHARIATI, 2018).

In order to further explore the order–disorder effects, band alignments as function of the electric field were illustrated in Figure 12-C to E and, as expected, the calculated bandgaps decreased along the intensity of the electric field due to the effects originated from the structural polarization of the clusters. As such, the exciton binding energies and dipole moments as function of the electric field are also shown in Table 2. As a result, the decrease of the binding energy and the increase of the dipole moment for all clusters has been observed, which is consistent with the previous discussion. Also, it should be noted that $Zn_3Cd_3S_6$ clusters have a greater dipole moment. This likely is due to difference in Zn-S and Cd-S bonds, which leads to a major structural polarization of this $Zn_3Cd_3S_6$ clusters.

Table 1 - Computed UV-Vis spectra of the $Zn_{6-x}Cd_xS_6$ clusters

| Cluster	Transition	Wavelength	Energy	Exciton Binding Energy
Zn_6S_6	HOMO-2 → LUMO	345 nm	3.59 eV	0.86 eV
Zn_5CdS_6	HOMO-3 → LUMO	340 nm	3.65 eV	0.73 eV
	HOMO-2 → LUMO	377 nm	3.29 eV	
$Zn_4Cd_2S_6$	HOMO-3 → LUMO	360 nm	3.44 eV	0.72 eV
	HOMO-2 → LUMO	402 nm	3.08 eV	
$Zn_3Cd_3S_6$	HOMO-3 → LUMO	379 nm	3.27 eV	0.72 eV
	HOMO-2 → LUMO	418 nm	2.96 eV	
$Zn_2Cd_4S_6$	HOMO-3 → LUMO	399 nm	3.10 eV	0.70 eV
	HOMO-2 → LUMO	428 nm	2.90 eV	
$ZnCd_5S_6$	HOMO-3 → LUMO	417 nm	2.97 eV	0.68 eV
	HOMO-2 → LUMO	438 nm	2.83 eV	
Cd_6S_6	HOMO-2 → LUMO	448 nm	2.77 eV	0.67 eV

Source: authors (2022)

Table 2 - Exciton binding energy and dipole moment as function of the electric field for the Zn$_6$S$_6$, Zn$_3$Cd$_3$S$_6$ and Cd$_6$S$_6$ clusters

Cluster	Exciton Binding Energy and Dipole Moment as function of the Electric Field			
	0 V Å^{-1}	0.05 V Å^{-1}	0.10 V Å^{-1}	0.20 V Å^{-1}
Zn$_6$S$_6$	0.86 eV	0.84 eV	0.84 eV	0.83 eV
	0 D	0.12 D	0.64 D	1.28 D
Zn$_3$Cd$_3$S$_6$	0.72 eV	0.71 eV	0.70 eV	0.67 eV
	2.99 D	3.00 D	3.19 D	3.69 D
Cd$_6$S$_6$	0.67 eV	0.69 eV	0.65 eV	0.63 eV
	0 D	0.24 D	1.24 D	2.48 D

Source: authors (2022)

Figure 13-A to C shows the calculated total DOS and the corresponding HOMO and LUMO shape of the Zn$_6$S$_6$, Zn$_3$Cd$_3$S$_6$ and Cd$_6$S$_6$ clusters as a function of applied electric field. As such, the HOMO and LUMO energies obtained through DOS were used to estimate the energy gap of the Zn$_{6-x}$Cd$_x$S$_6$ clusters and to create the band alignment of energy levels. Additionally, the ionization potentials calculated through the Koopman's theorem and the HOMO energy for the Zn$_6$S$_6$ to Cd$_6$S$_6$ clusters were, respectively, 7.50, 7.30, 7.16, 7.07, 6.92, 6.81, and 6.76 eV (KOOPMANS, 1934). The estimated ionization potentials are significantly higher than the reported in other works for Zn$_6$S$_6$ (6.95 eV) and a slight deviated from Cd$_6$S$_6$ (~6.7 eV) due to the base set used; however, the higher energy tendency of ZnS is observed for this parameter, as well (DHUVAD; SHARMA, 2010; LA PORTA et al., 2014a).

Figure 13 - Calculated total DOS and the corresponding HOMO and LUMO shape of the A) Zn_6S_6, B) $Zn_3Cd_3S_6$, and C) Cd_6S_6 clusters as a function of an applied electric field
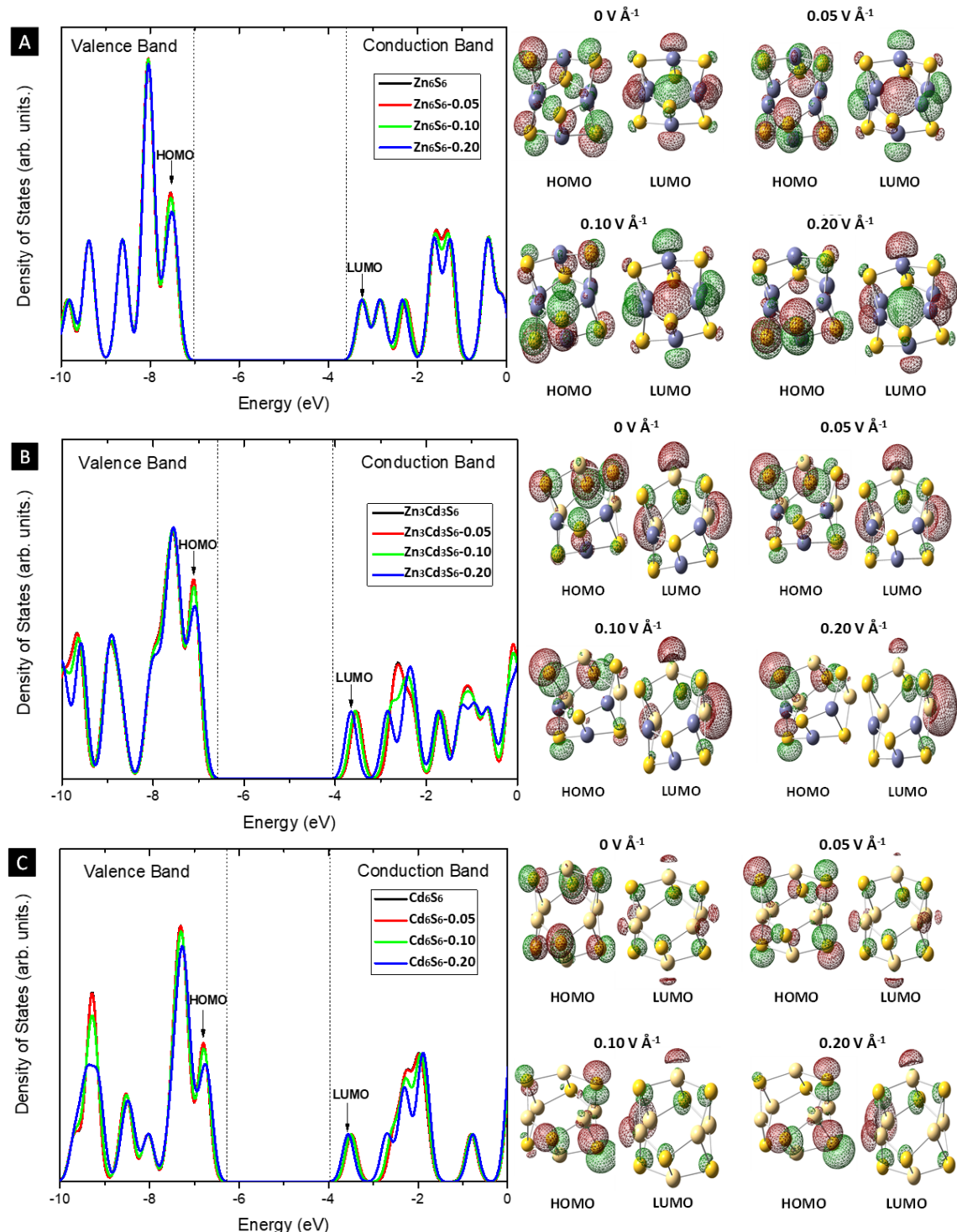
Source: authors (2022)

The orbitals compositions were discovered using the DOS spectra, founding that Zn_6S_6 HOMO is mainly composed of S $3p$ orbitals and LUMO of Zn $4sp$ hybrid orbitals. The Cd_6S_6 orbitals are quite similar to ZnS, thus presenting HOMO consisted

of S *4p* orbitals and LUMO of Cd *5sp* hybrid orbitals. On the other hand, the binding energies were also calculated for both Zn_6S_6 and Cd_6S_6 clusters, using the difference $\Delta E = E_{HOMO} - E_{core-level}$, where $E_{core-level}$ is the energy of Zn *3d* or Cd *4d* orbitals (LA PORTA et al., 2014b). Therefore, the estimated values for the binding energies of Zn and Cd d^{10} electrons are approximately 4.54 and 9.55 eV for both Zn_6S_6 and Cd_6S_6 clusters, respectively. However, these values obtained are smaller than those available from X-ray photoelectron spectroscopic studies for ZnS (10.6 eV) and CdS (11.5 eV) (LA PORTA et al., 2013, 2014b; POIRIER; WEAVER, 1993; XU et al., 1998). Though the calculated binding energy matches the experimental tendency, the use of a more robust methodology could lead to more realistic binding energies.

4.4. Conclusions

In this study, it was possible to obtain insights into the influence of the electric field on the electronic structure and spectroscopic properties of the $Zn_{6-x}Cd_xS_6$ clusters as model systems of QDs. It was observed distortions in the bond lengths and angles as the original ZnS and CdS structures became hybrids, in which the Zn_6S_6 cluster showed more compact structure than Cd_6S_6, and $Zn_3Cd_3S_6$ the most distorted. The electric field was responsible for more distorted structures and polarized S-Zn-S and S-Cd-S bond lengths, reaching a limit at 0.20 V $Å^{-1}$. The Raman-active modes and the excitonic transitions were also identified in this study. Hence, in all cases, the excitonic transitions and energies involved were affected by the electric field in manners of quantum Stark effect, as shown in the band alignments, the polarization of HOMO and LUMO orbitals, the electronic band gap, and the excitonic bands. Overall, the thermodynamic properties of the $Zn_{6-x}Cd_xS_6$ clusters, suggest that the Zn_6S_6 cluster is more stable than Cd_6S_6 cluster.

4.5. Acknowledgments

4.6.   References

ACHARYA, S. A.; DARULKAR, S.; CHOUDHARY, P. Effect of Coordination Agent on the Structure and Morphology of ZnS Nanostructure. In: [s.l: s.n.]. p. 65–75.

AZPIROZ, J. M. et al. A first-principles study of II–VI (II = Zn; VI = O, S, Se, Te) semiconductor nanostructures. **Journal of Materials Chemistry**, v. 22, n. 40, p. 21453, 2012.

AZPIROZ, J. M.; UGALDE, J. M.; INFANTE, I. Benchmark Assessment of Density Functional Methods on Group II–VI MX (M = Zn, Cd; X = S, Se, Te) Quantum Dots. **Journal of Chemical Theory and Computation**, v. 10, n. 1, p. 76–89, 14 jan. 2014.

BAE, W. K. et al. Highly Efficient Green-Light-Emitting Diodes Based on CdSe@ZnS Quantum Dots with a Chemical-Composition Gradient. **Advanced Materials**, v. 21, n. 17, p. 1690–1694, 4 maio 2009.

BANERJEE, R. et al. Effect of the size-induced structural transformation on the band gap in CdS nanoparticles. **Journal of Physics: Condensed Matter**, v. 12, n. 50, p. 10647–10654, 18 dez. 2000.

BANSAL, A. K. et al. Highly Luminescent Colloidal CdS Quantum Dots with Efficient Near-Infrared Electroluminescence in Light-Emitting Diodes. **The Journal of Physical Chemistry C**, v. 120, n. 3, p. 1871–1880, 28 jan. 2016.

BHARGAVA, R. **Properties of Wide Bandgap II-VI Semiconductors**. London: INSPEC, 1997.

BURNIN, A.; SANVILLE, E.; BELBRUNO, J. J. Experimental and Computational Study of the Zn n S n and Zn n S n + Clusters. **The Journal of Physical Chemistry A**, v. 109, n. 23, p. 5026–5034, jun. 2005.

CHEN, R. et al. Optical and Excitonic Properties of Crystalline ZnS Nanowires: Toward Efficient Ultraviolet Emission at Room Temperature. **Nano Letters**, v. 10, n. 12, p. 4956–4961, 8 dez. 2010.

CHENG, Y. C. et al. Raman scattering study of zinc blende and wurtzite ZnS. **Journal of Applied Physics**, v. 106, n. 12, p. 123505, 15 dez. 2009.

DENG, K.; LI, L. CdS Nanoscale Photodetectors. **Advanced Materials**, v. 26, n. 17, p. 2619–2635, maio 2014.

DHUVAD, P. H.; SHARMA, A. C. An ab-initio study of photoabsorption spectrum of ultra small CdS clusters. **Physica E: Low-dimensional Systems and Nanostructures**, v. 42, n. 5, p. 1365–1371, mar. 2010.

EMPEDOCLES, S. A. Quantum-Confined Stark Effect in Single CdSe Nanocrystallite Quantum Dots. **Science**, v. 278, n. 5346, p. 2114–2117, 19 dez. 1997.

FANG, X. et al. ZnS nanostructures: From synthesis to applications. **Progress in Materials Science**, v. 56, n. 2, p. 175–287, fev. 2011.

FRISCH, M. J. et al. Gaussian 09. Versão 9. Wallingford CT: Gaussian Inc, 2009.

GIAMPIETRI, A.; DRERA, G.; SANGALETTI, L. Band Alignment at Heteroepitaxial Perovskite Oxide Interfaces. Experiments, Methods, and Perspectives. **Advanced Materials Interfaces**, v. 4, n. 11, p. 1700144, jun. 2017.

GONG, K.; KELLEY, D. F.; KELLEY, A. M. Resonance Raman excitation profiles of CdS in pure CdS and CdSe/CdS core/shell quantum dots: CdS-localized excitons. **The Journal of Chemical Physics**, v. 147, n. 22, p. 224702, 14 dez. 2017.

HE-YING, C. et al. First-principles study of structures and electronic properties of cadmium sulfide clusters. **Chinese Physics B**, v. 17, n. 7, p. 2478–2483, jul. 2008.

HUANG, F.; BANFIELD, J. F. Size-Dependent Phase Transformation Kinetics in Nanocrystalline ZnS. **Journal of the American Chemical Society**, v. 127, n. 12, p. 4523–4529, mar. 2005.

KOOPMANS, T. Über die Zuordnung von Wellenfunktionen und Eigenwerten zu den Einzelnen Elektronen Eines Atoms. **Physica**, v. 1, n. 1–6, p. 104–113, jan. 1934.

KOVALENKO, M. V. et al. Prospects of Nanoscience with Nanocrystals. **ACS Nano**, v. 9, n. 2, p. 1012–1057, 24 fev. 2015.

KRAINARA, N. et al. Magic Numbers in a One-Dimensional Nanosystem: ZnS Single-Walled Nanotubes. **The Journal of Physical Chemistry C**, v. 117, n. 44, p. 22908–22914, 7 nov. 2013.

LA PORTA, F. A. et al. Orbital Signatures as a Descriptor of Regioselectivity and Chemical Reactivity: The Role of the Frontier Orbitals on 1,3-Dipolar Cycloadditions. **The Journal of Physical Chemistry A**, v. 115, n. 5, p. 824–833, 10 fev. 2011.

LA PORTA, F. A. et al. Synthesis of wurtzite ZnS nanoparticles using the microwave assisted solvothermal method. **Journal of Alloys and Compounds**, v. 556, p. 153–159, abr. 2013.

LA PORTA, F. A. et al. Zinc blende versus wurtzite ZnS nanoparticles: control of the phase and optical properties by tetrabutylammonium hydroxide. **Phys. Chem. Chem. Phys.**, v. 16, n. 37, p. 20127–20137, 2014a.

LA PORTA, F. A. et al. A DFT Study of Structural and Electronic Properties of ZnS Polymorphs and its Pressure-Induced Phase Transitions. **Journal of the American**

Ceramic Society, v. 97, n. 12, p. 4011–4018, dez. 2014b.

LA PORTA, F. A. et al. An experimental and theoretical investigation on the optical and photocatalytic properties of ZnS nanoparticles. **Journal of Physics and Chemistry of Solids**, v. 103, p. 179–189, abr. 2017.

LANDMANN, M.; RAULS, E.; SCHMIDT, W. G. Understanding band alignments in semiconductor heterostructures: Composition dependence and type-I–type-II transition of natural band offsets in nonpolar zinc-blende $Al_xGa_{1-x}N/Al_yGa_{1-y}N$ composites. **Physical Review B**, v. 95, n. 15, p. 155310, 12 abr. 2017.

LIU, X. et al. Facile synthesis of high-quality ZnS, CdS, CdZnS, and CdZnS/ZnS core/shell quantum dots: characterization and diffusion mechanism. **Materials Science in Semiconductor Processing**, v. 16, n. 6, p. 1723–1729, dez. 2013.

MAZZO, T. M. et al. Controlling the Electronic, Structural, and Optical Properties of Novel MgTiO 3 /LaNiO 3 Nanostructured Films for Enhanced Optoelectronic Devices. **ACS Applied Nano Materials**, v. 2, n. 5, p. 2612–2620, 24 maio 2019.

MURRAY, C. B.; KAGAN, C. R.; BAWENDI, M. G. Synthesis and Characterization of Monodisperse Nanocrystals and Close-Packed Nanocrystal Assemblies. **Annual Review of Materials Science**, v. 30, n. 1, p. 545–610, ago. 2000.

NASRAOUI, S. et al. Effects of thiol ligands on the growth and stability of CdS nanoclusters. **Journal of Molecular Structure**, v. 1198, p. 126832, dez. 2019.

O'BOYLE, N. M.; TENDERHOLT, A. L.; LANGNER, K. M. cclib: A library for package-independent computational chemistry algorithms. **Journal of Computational Chemistry**, v. 29, n. 5, p. 839–845, 15 abr. 2008.

OLIVEIRA, L. H. et al. Optical and gas-sensing properties, and electronic structure of the mixed-phase CaCu 3 Ti 4 O 12 /CaTiO 3 composites. **Materials Research Bulletin**, v. 93, p. 47–55, set. 2017.

OUENDADJI, S. et al. Theoretical study of structural, electronic, and thermal properties of CdS, CdSe and CdTe compounds. **Computational Materials Science**, v. 50, n. 4, p. 1460–1466, fev. 2011.

PAIER, J. et al. Screened hybrid density functionals applied to solids. **The Journal of Chemical Physics**, v. 124, n. 15, p. 154709, 21 abr. 2006.

PAIER, J.; MARSMAN, M.; KRESSE, G. Why does the B3LYP hybrid functional fail for metals? **The Journal of Chemical Physics**, v. 127, n. 2, p. 024103, 14 jul. 2007.

PARK, Y. S.; REYNOLDS, D. C. Exciton Structure in Photoconductivity of CdS, CdSe, and CdS: Se Single Crystals. **Physical Review**, v. 132, n. 6, p. 2450–2457, 15 dez.

1963.

PEGU, D. et al. Electronic, nonlinear optical and thermodynamic properties of (CdS) n clusters: A first principle study. **Computational Condensed Matter**, v. 14, p. 40–45, mar. 2018.

PETRYAYEVA, E.; ALGAR, W. R.; MEDINTZ, I. L. Quantum dots in bioanalysis: A review of applications across various platforms for fluorescence spectroscopy and imaging. **Applied Spectroscopy**, v. 67, n. 3, p. 215-352, mar. 2013.

POIRIER, D. M.; WEAVER, J. H. CdS by XPS. **Surface Science Spectra**, v. 2, n. 3, p. 249–255, jul. 1993.

RAMALHO, T. C.; TAFT, C. A. Thermal and solvent effects on the NMR and UV parameters of some bioreductive drugs. **The Journal of Chemical Physics**, v. 123, n. 5, p. 054319, ago. 2005.

RAUBACH, C. W. et al. Photocatalytic activity of semiconductor sulfide heterostructures. **Dalton Transactions**, v. 42, n. 31, p. 11111, 2013.

REGULACIO, M. D. et al. Aqueous synthesis of highly luminescent AgInS2–ZnS quantum dots and their biological applications. **Nanoscale**, v. 5, n. 6, p. 2322, 2013.

ROCKENBERGER, J. et al. EXAFS Studies on the Size Dependence of Structural and Dynamic Properties of CdS Nanoparticles. **The Journal of Physical Chemistry B**, v. 101, n. 14, p. 2691–2701, abr. 1997.

RODRIGUEZ, J. A.; GORDILLO, G. Study of electrical properties in ZnxCd1−xS thin films. **Solar Energy Materials**, v. 19, n. 6, p. 421–431, dez. 1989.

SAMADI-MAYBODI, A.; SHARIATI, M. R. A study on the transfer of photo-excited charge carriers within direct and inverted type-I heterojunctions of CdS and ZnS QDs. **New Journal of Chemistry**, v. 42, n. 12, p. 9808-9818, abr. 2018.

SANVILLE, E.; BURNIN, A.; BELBRUNO, J. J. Experimental and Computational Study of Small (n = 1−16) Stoichiometric Zinc and Cadmium Chalcogenide Clusters. **The Journal of Physical Chemistry A**, v. 110, n. 7, p. 2378–2386, fev. 2006.

SCHREDER, B. et al. Raman spectroscopy of II-VI semiconductor nanostructures: CdS quantum dots. **Journal of Raman Spectroscopy**, v. 34, n. 2, p. 100–103, fev. 2003.

SHIN, Y. J. et al. Photocurrent study on the splitting of the valence band for a CdS single-crystal platelet. **Physical Review B**, v. 44, n. 11, p. 5522–5526, 15 set. 1991.

SUN, J.-Q. et al. Low-temperature synthesis of hexagonal ZnS nanoparticles by a facile microwave-assisted single-source method. **Solid State Communications**, v.

147, n. 11–12, p. 501–504, set. 2008.

TALAPIN, D. V. et al. Prospects of Colloidal Nanocrystals for Electronic and Optoelectronic Applications. **Chemical Reviews**, v. 110, n. 1, p. 389–458, 13 jan. 2010.

TAN, J. J.; LI, Y.; JI, G. F. High-Pressure Phase Transitions and Thermodynamic Behaviors of Cadmium Sulfide. **Acta Physica Polonica A**, v. 120, n. 3, p. 501–506, set. 2011.

TONG, H. et al. Self-Assembled ZnS Nanostructured Spheres: Controllable Crystal Phase and Morphology. **The Journal of Physical Chemistry C**, v. 111, n. 10, p. 3893–3900, mar. 2007.

TRAJIĆ, J. et al. Raman spectroscopy of ZnS quantum dots. **Journal of Alloys and Compounds**, v. 637, p. 401–406, jul. 2015.

TRAN, T. K. et al. Photoluminescence properties of ZnS epilayers. **Journal of Applied Physics**, v. 81, n. 6, p. 2803–2809, 15 mar. 1997.

WANG, X. et al. Gas sensors, thermistor and photodetector based on ZnS nanowires. **Journal of Materials Chemistry**, v. 22, n. 14, p. 6845, 2012.

WANG, Y. R.; DUKE, C. B. Atomic and electronic structure of ZnS cleavage surfaces. **Physical Review B**, v. 36, n. 5, p. 2763–2769, 15 ago. 1987.

XU, J. F. et al. Preparation of ZnS nanoparticles by ultrasonic radiation method. **Applied Physics A: Materials Science & Processing**, v. 66, n. 6, p. 639–641, 1 jun. 1998.

XU, R. et al. Zinc blende and wurtzite cadmium sulfide nanocrystals with strong photoluminescence and ultrastability. **Journal of Crystal Growth**, v. 299, n. 1, p. 28–33, fev. 2007.

YE, Y. et al. Roles of adsorption sites in electron transfer from CdS quantum dots to molecular catalyst cobaloxime studied by time-resolved spectroscopy. **Physical Chemistry Chemical Physics**, v. 18, n. 26, p. 17389–17397, 2016.

YU, Y.-M. et al. Band gap energy and exciton peak of cubic CdS/GaAs epilayers. **Journal of Applied Physics**, v. 92, n. 2, p. 1162–1164, 15 jul. 2002.

ZHAO, Y. et al. Low-Temperature Synthesis of Hexagonal (Wurtzite) ZnS Nanocrystals. **Journal of the American Chemical Society**, v. 126, n. 22, p. 6874–6875, jun. 2004.

ZHAO, Y.; TRUHLAR, D. G. Density Functionals with Broad Applicability in Chemistry. **Accounts of Chemical Research**, v. 41, n. 2, p. 157–167, fev. 2008.

ZHU, N. et al. Combined CdS nanoparticles-assisted photocatalysis and periphytic biological processes for nitrate removal. **Chemical Engineering Journal**, v. 353, p. 237–245, dez. 2018.

ZWIJNENBURG, M. A.; ILLAS, F.; BROMLEY, S. T. The fate of optical excitations in small hydrated ZnS clusters: a theoretical study into the effect of hydration on the excitation and localisation of electrons in Zn4S4 and Zn6S6. **Physical Chemistry Chemical Physics**, v. 13, n. 20, p. 9311, 2011.

5. ARTIGO 2: PROSPECTS OF ZnS AND ZnO AS SMART SEMICONDUCTORS MATERIALS IN LIGHT-ACTIVATED ANTIMICROBIAL COATINGS FOR MITIGATION OF SEVERE ACUTE RESPIRATORY SYNDROME CORONAVIRUS-2 INFECTION

5.1. Introduction

Epidemics worldwide caused by common antibiotic-resistant microorganisms susceptible to mutations, together with the lack of vaccines and efficient treatments, as well as their associated hospital infections, are a serious risk to the global health, particularly in under-developed countries (ALMEIDA BATISTA et al., 2019; DUAN et al., 2021; MICOLI et al., 2021; SIRELKHATIM et al., 2015). The pandemic caused by the outbreak of the new coronavirus (severe acute respiratory syndrome coronavirus-2 (SARS-CoV-2), responsible for the coronavirus disease (COVID)-19, led to the use of personal protective masks as a mandatory non-pharmacological measure in every country (DE SOUSA NETO; DE FREITAS, 2020; FARIAS, 2020; GARCIA, 2020; WOROBEY et al., 2020). This led to a shortage of masks in the first few months of the pandemic. Particularly, the efficiency of personal protective masks was evaluated by Ueki et al. (UEKI et al., 2020). They demonstrated that the use of masks can prevent the transmission of SARS-CoV-2, leading to a virus absorption reduction by 70% when two mannequins used cloth and surgical masks and by almost 100% with N95 masks (UEKI et al., 2020). Studies targeting the SARS-CoV-2 regarding the efficiency and reusability of masks as well as the development of masks intelligently designed with graphene were published last year by Liao et al. and Zhong et al. (LIAO et al., 2020; ZHONG et al., 2020). The study by Hamdi et al. published this year suggests an antiviral activity of ZnO against the SARS-CoV-2 (HAMDI et al., 2021).

Extensive studies have been carried out to contain the advance of COVID-19, leading to the development of vaccines in record time. However, despite these advances, the contamination rate remains high in several countries (SANTOS, 2020; TESINI, 2020; ZHU et al., 2020). Therefore, from this perspective, the development of more efficient personal protective masks that can be reused is important to help stop this advance, particularly while most of the world population has not yet been vaccinated with the first dose (MATHIEU et al., 2021).

In this regard, the development of nanoscale materials with biological activity in a broader spectrum for broader applications as antimicrobial agents is of interest

(ESPITIA et al., 2012; RAI; YADAV; GADE, 2009; SATHISHKUMAR; RAJAMANICKAM; SAROJA, 2018). Among the semiconductor materials, ZnS and ZnO are very promising owing to their outstanding physical properties, manufacturing simplicity for different synthesis strategies, low cost, high chemical and thermal stabilities, and high versatility for several technologies (such as, ultraviolet light diodes, photocatalysis, sensors, and solar cells) (BERGER et al., 2016; FONSECA et al., 2018; HE et al., 2014; JANAKI; SAILATHA; GUNASEKARAN, 2015; KHANLARY; REYHANI, 2018; KWAMBOKA; OMWOYO*; OYARO, 2016; SAPSFORD et al., 2006; SATHISHKUMAR et al., 2016). They also exhibit high antimicrobial activities (DHUPAR et al., 2021; GUDKOV et al., 2021; KOKILAVANI et al., 2021; NAVARRO-LÓPEZ et al., 2021).The hydro(solvo)thermal method can be used as a low-cost approach to produce ZnS and ZnO nanoparticles (NPs) with high purity and crystallinity (LA PORTA et al., 2013, 2014a, 2014b, 2017). Further, the morphologies of ZnO and ZnS crystals and their physical properties may be tuned by their shapes and sizes, which are optimized by the synthesis parameters, such as the supersaturation, temperature, solvent and precursors, which affects the hydro(solvo)thermal growth kinetics of NPs (BARUAH; DUTTA, 2009; HE; TSUZUKI, 2010; LA PORTA et al., 2013, 2014a, 2014b, 2017; LEE et al., 2021; ZHANG et al., 2018). Based on the broad-spectrum antimicrobial activities of ZnO and ZnS NPs, they have been extensively investigated compared to other advanced materials as nontoxic to human cells (COLON; WARD; WEBSTER, 2006; ETACHERI et al., 2013; KHO; TORRES-MARTÍNEZ; MEHRA, 2000; KUMAR et al., 2014; NI et al., 2004; PADMAVATHY; VIJAYARAGHAVAN, 2008; SIRELKHATIM et al., 2015; VANAJA et al., 2013). In addition, ZnS and ZnO are classified as safe materials by the Food and Drug Administration agency (FDA, 2020).

We carried out a systematic experimental and theoretical study on ZnS and ZnO as promising antimicrobial coatings for mitigation of the SARS-CoV-2 infection. The photodegradation of a methylene blue (MB) dye was evaluated for ZnO and ZnS coating cotton fabrics prepared by the hydro(solvo)thermal method. For understanding at the molecular level, the broad-spectrum biological activities of these materials were evaluated theoretical calculations. The biological targets used in this computational study were Fusarium Oxysporum fungi, E. Coli bacteria, and SARS-CoV-2 virus and their variants. The results suggest that both ZnS and ZnO can be used as a light-

activated antimicrobial coatings on a large scale for the production of more efficient protection masks for SARS-CoV-2 infection mitigation.

5.2. Methodology

5.2.1. Fabrication of ZnO and ZnS coatings

The ZnO and ZnS coatings of cotton fabrics (2.5×2 cm^2) were synthesized by the hydro(solvo)thermal method at 160 °C for 120 min. In the preparation of ZnO coatings, 7.34 mmol of zinc acetate was dissolved in 80 mL of deionized water, and then 3 mL of ammonium hydroxide (30% in NH$_3$, Synth) was added. This solution was transferred to a Teflon autoclave with the cotton fabrics, properly sealed and placed in a muffle oven. The process was carried out at 160 °C for 120 min, repeated twice, with varying concentration of the Zn precursor, 3.68 and 1.84 mmol.

For the ZnS coatings, 7.34 mmol of zinc acetate was dissolved in 25 mL of ethylene glycol (EG) heated to 80 °C, and then 16 mmol of tetrabutylammonium hydroxide (40%) was added. A second solution with 7.34 mmol of thiourea dissolved in 25 mL of EG was prepared. The zinc-precursor solution was injected into the sulphur-precursor solution under magnetic stirring, transferred to a Teflon autoclave with the cotton fabrics, properly sealed and placed in a muffle oven. The procedure was carried out at 160 °C for 120 min, repeated with varying concentration of the precursors, 3.68 and 1.84 mmol. All product materials were washed and dried at the end of the procedure.

5.2.2. Characterization

The cotton fabrics with ZnO and ZnS NPs were structurally characterized by X-ray diffraction (XRD) using a Bruker-D2 PHASER instrument with Cu Kα radiation (λ = 1.5406 Å) in the range of 20° to 45° at 0.004°/s. Optical characterization was performed by ultraviolet-visible (UV-vis) spectra recorded with a S60 Libra (Biochrom) spectrophotometer. The morphologies of the ZnO and ZnS coated cotton fabrics were observed by scanning electron microscopy (SEM) using a TESCAN VEGA 4 microscope. Photocatalysis experiments were performed to analyze the disinfection potentials of these coatings. For this analysis, tissues with and without ZnO and ZnS NPs were immersed in a 10 mg.L^{-1} MB dye solution for 60 min to complete the dye

adsorption step, and then were removed from the MB dye solution, dried, and exposed to a photoreactor UVC lamp (254 nm, 15 W, G15T8/OF, OSRAM). UV-vis absorption measurements were carried out at regular intervals in the period of 0-240 min.

5.2.3. Quantum-chemical calculations

To study NPs and their antimicrobial properties theoretically, the Zn_6O_6 and Zn_6S_6 hexagonal clusters were selected as models for the ZnO and ZnS wurtzite systems, which are known to exhibit good agreement between theoretical and experimental results (DE JESUS; JIMENEZ; LA PORTA, 2021; LA PORTA et al., 2014a). Thus, the optimized clusters involving no imaginary frequencies were obtained using density functional theory (DFT) at the B3LYP/6-31+G(d,p) level. The electronic structures and spectroscopic properties were determined using time-dependent DFT (TD-DFT) calculations. For the excited states, the optimization calculations were performed using TD-DFT with root = 2. To analyze the charge transfer between excited states, single-point calculations were performed on the natural bond orbital (NBO) population. To obtain molecular electrostatic potential (MEP) maps, post Hartree-Fock energy calculations were performed on charges from electrostatic potential using a grid-based method (CHELPG) population at the MP2 level. MEP and molecular orbital (MO) surfaces were generated using GaussView (DENNINGTON; KEITH; MILLAM, 2016) with surface isovalues of 0.0004 and 0.0300, respectively. Finally, the density of states (DOS) spectra were plotted using GaussSum software (O'BOYLE; TENDERHOLT; LANGNER, 2008). All the calculations were performed using the Gaussian 09 software package.

Calculations based on Bader's theory of atoms in molecules (QTAIM) (KUMAR; RAGHAVENDRA; SUBRAMANIAN, 2016) are quite important in facilitating the comprehension of the nature of chemical bonds (for instance, to determine if the bond has covalent, partially covalent, or non-covalent characteristics) (SILVA et al., 2017). QTAIM calculations were performed for optimized Zn_6O_6 and Zn_6S_6 clusters at the B3LYP/6-31+G(d,p) level using the AIM program (KUMAR; RAGHAVENDRA; SUBRAMANIAN, 2016).

5.2.4. Molecular docking studies

Molecular docking calculations were performed using the Molegro virtual docker program (MVD®) (THOMSEN; CHRISTENSEN, 2006), considering the same procedures employed previously (GUIMARAES et al., 2011; MATOS et al., 2011; SILVA et al., 2015). For each investigated ligand, 30 poses (conformation and orientation) were generated as required by the nature of the docking methods calculations. The crystal structure dataset for the SARS-CoV-2 M^{pro} enzyme was obtained from the Protein Data Bank (PDB ID: 5R82, resolution 1.31Å) (BERMAN et al., 2000). The mutant M^{pro} R60C (KHAN et al., 2020) was prepared by inserting the point mutation using Discovery Studio software (ACCELRYS SOFTWARE, 2012), and it was minimized using the Swiss PDB viewer application (https://spdbv.vital-it.ch/). The crystal structure dataset for the *Fusarium Cutinase* enzyme was also obtained from the PDB (PDB ID: 1XZL, resolution 1.69 Å) (LONGHI et al., 1996) along with the crystal structure dataset for DNA gyrase from *Escherichia coli* (PDB ID: 1KZN, resolution 2.30Å) (LAFITTE et al., 2002). The theoretical values of the lethal dose (LD$_{50}$) were also obtained in this study for a rat model-based ADMET predictor (http://biosig.unimelb.edu.au/pkcsm/prediction). These techniques have been successfully employed for similar systems (ASSIS et al., 2021a, 2021b; DE CASTRO et al., 2022; DE JESUS et al., 2021).

5.3. Results and Discussions

The properties of crystalline materials are strongly dependent on their structure/composition in the short-, medium-, and long-range orders. In this regard, structural characterization is of interest to both theorists and experimentalists in the development of various materials with highly tailored properties (LA PORTA; TAFT, 2021, 2020; LONGO; LA PORTA, 2017).

Figure 14-A and B show XRD patterns of the ZnO and ZnS coatings of the cotton fabrics, where highly pure and crystalline structure are observed in the long-range order, which can be indexed to the wurtzite structure according to the Joint Committee on Powder Diffraction Standards (JCPDS) cards 36-1451 and 36–1450, respectively. The growth occurred preferentially in the (002) direction for ZnO and (101) direction for ZnS. The coated tissues exhibit slightly different average crystallite

sizes of approximately ~6.2 nm for ZnO and ~4.6 for ZnS, calculated by the Scherrer method.

Figure 14 - XRD patterns of the A) ZnO and B) ZnS coatings. C) Measurement of the contact angles of the ZnO and ZnS coatings of the cotton fabrics

Source: authors (2022)
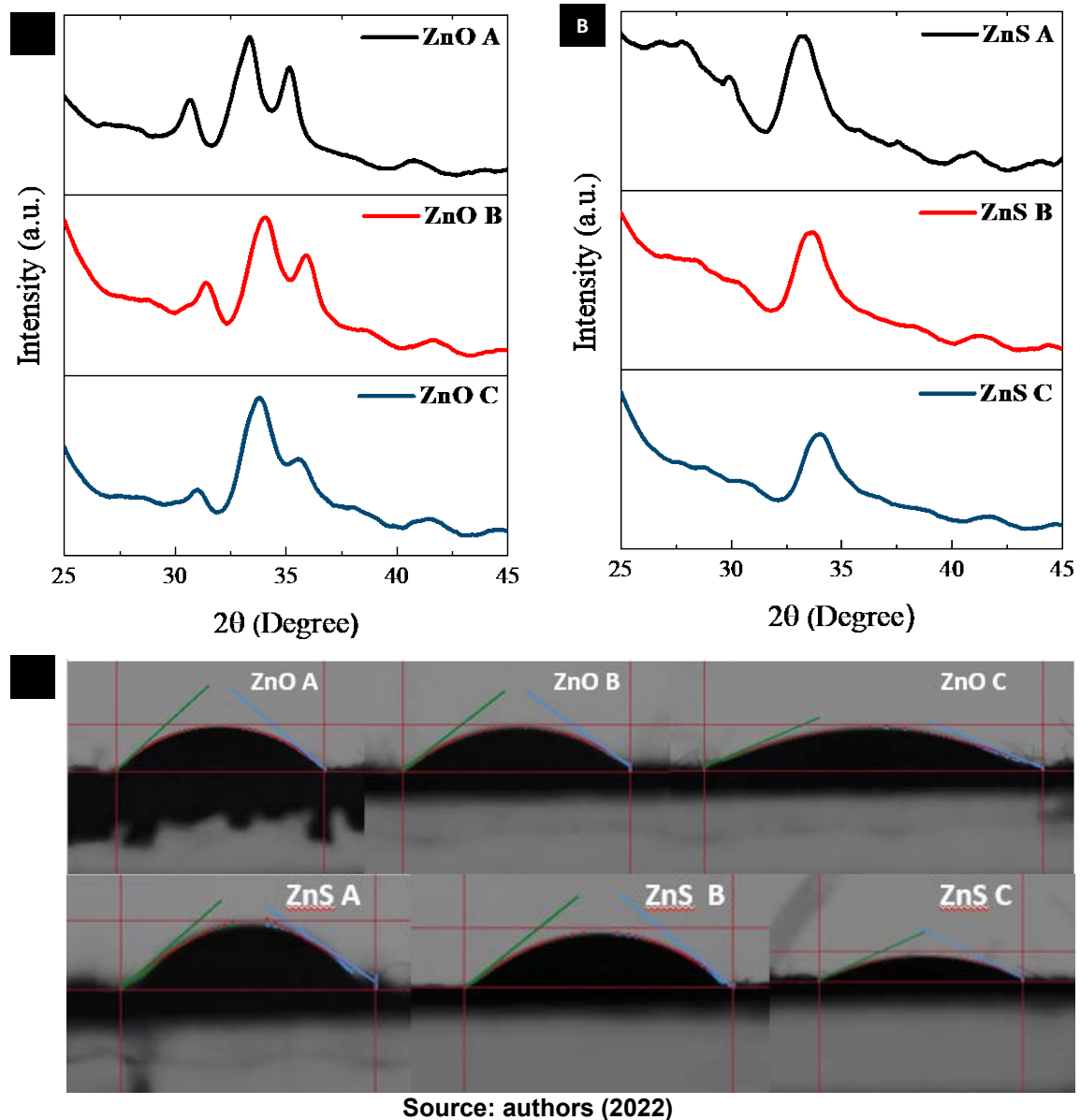
The wettability of a material is directly related to the interaction between its surface and liquid. At a lower wettability, the angle of contact with the surface is larger (DHAYGUDE et al., 2015). Images of the contact angles are shown in Figure 14-C, while their values are listed in Table 3. The surfaces of both ZnO and ZnS coatings are naturally hydrophilic.

Table 3 - Average optical transmittances of the ZnO- and ZnS-coated cotton fabrics in the visible range and film thicknesses

| Sample	Film Thickness (µm)	Average Transmittance (T%)	Contact Angle (°)
ZnO A	28.03	50.66	41.21
ZnO B	20.40	61.66	36.49
ZnO C	16.56	81.87	22.44
ZnS A	23.01	49.21	38.86
ZnS B	19.42	68.14	34.16
ZnS C	16.16	81.76	24.73

Source: authors (2022)

To investigate the effect of the film thickness on the optical properties of the ZnS and ZnO tissues, optical transmittance measurements at different thicknesses were performed. Through the transmittance spectra obtained by UV-vis spectrophotometry, the refractive index s and thickness of the incorporated films were estimated by the Swanepoel method (SWANEPOEL, 1983), used to simulate wave patterns in transmittance spectra (equations (15, 16)). In equation (14), Ts is the substrate maximum transmission value, while, in equation (15), $n1$ are refractive indices obtained from two consecutives maxima or minima, corresponding to wavelengths $l1$ and $l2$.

$$s = \frac{1}{Ts} + \left(\frac{1}{T^2s} - 1\right)^{\frac{1}{2}}$$

(15)

$$d = \frac{\lambda1\lambda2}{2(\lambda n1 - \lambda2 n1)}$$

(16)

The optical transmittance spectra are plotted in Figure 15, while average transmittance values are listed in Table 1. As observed, the films are highly transparent in the visible range (above 50%). The refractive indices of all fabric samples were approximately 1.51. As the film thickness increased, the average transmittance decreased due to the thickness effects.

Figure 15 - Transmittance spectra of the ZnO and ZnS coated cotton fabrics
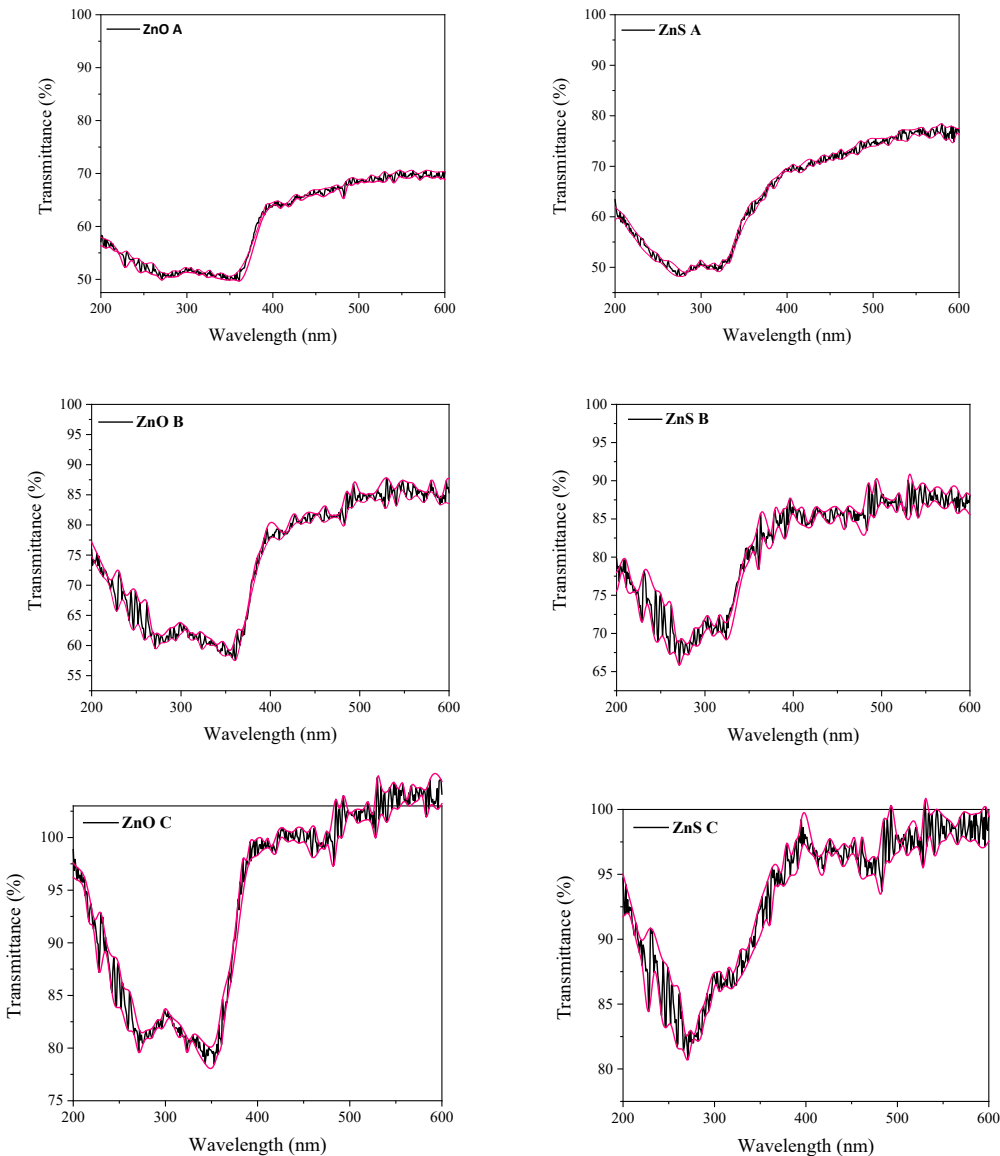

Source: authors (2022)

Figure 16-A and B show SEM images of the ZnS- and ZnO-coated cotton fabrics. Different morphologies, spherical-like for the ZnS coating and flower for the ZnO coating are observed in the SEM images, in good agreement with our previous studies (LA PORTA et al., 2013, 2014a, 2014b, 2017). The application of ZnO and ZnS NPs in disinfection technologies has been reported (LAXMA REDDY et al., 2017; RAY et al., 2017; REGMI et al., 2018). To analyse the ability to remove organic dye residues, the photocatalytic activities of tissues impregnated with ZnO and ZnS NPs were evaluated by the degradation of the MB dye. Digital pictures of the impregnated tissues with ZnO and ZnS NPs after the MB solution adsorption step and 240 min of UVC

treatment are presented in Figure 16-C. These results show a significant reduction in adsorbed MB dye content on the as-prepared cotton fabrics. A simple visual inspection reveals a change in the colour, from dark blue to a very light blue close to white.

Figure 16 - SEM images of cotton fabrics impregnated with A) ZnS and B) ZnO NPs. C) Digital images of the ZnO- and ZnS-coated cotton fabrics after adsorption of the Methylene Blue solution and 240 min of UVC treatment. The inset shows the samples A-G: A - uncoated cotton fabric; B - ZnO sample A; C – ZnO sample B; D – ZnO sample C; E - ZnS sample A; F – ZnS sample B and G – ZnS sample C

Source: authors (2022)
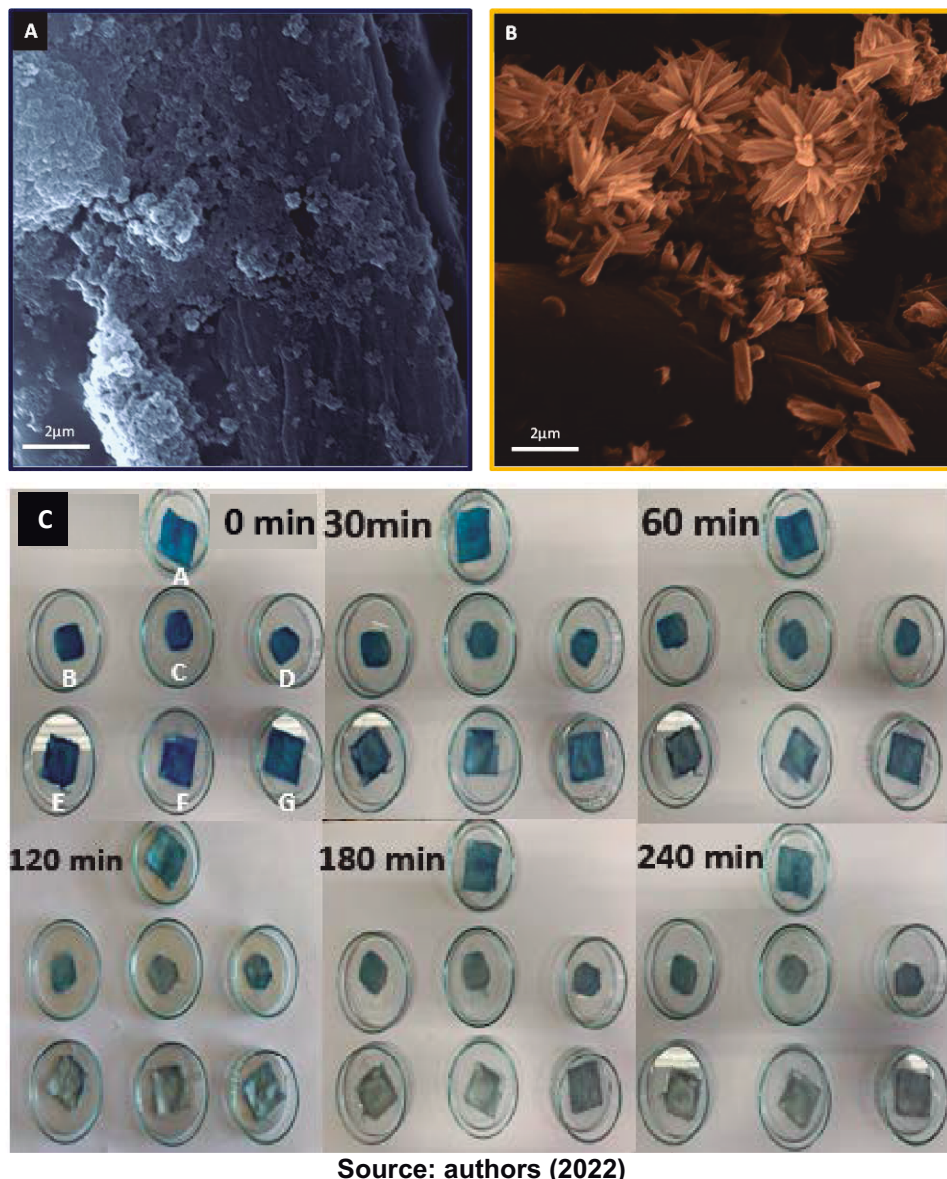
Figure 17-A show a bar graph of the degradation percentage of the MB dye for each sample. $In(C/C_0)$ vs. degradation time graphs in Figure 17-B were obtained to calculate k of the degradation reaction (using the slope). A better activity was obtained

in the photocatalytic test in the presence of ZnS with a higher amount of precursor. Table 4 lists the catalyst degradation reaction rates. The kinetic constants (k) without the NP impregnation were 0.00352, 0.01072, and 0.00736 min^{-1} for the impregnated samples with higher efficiencies for ZnS and ZnO. Figure 17-C show UV protection efficiency in the UVA and UVB regions for the ZnO- and ZnS-coated cotton fabrics. It is important to highlight that the uncoated cotton fabrics showed no UV protection properties. Both ZnO and ZnS coatings demonstrated excellent capacity for blocking UVA and UVB rays. These results are strongly correlated with the thickness of the coatings obtained.

Figure 17 - A). Degradation percentage of the Methylene Blue dye. B) ln(C/C₀) vs. degradation time plot. C) UV protection efficiency of the ZnO and ZnS coatings cotton fabrics
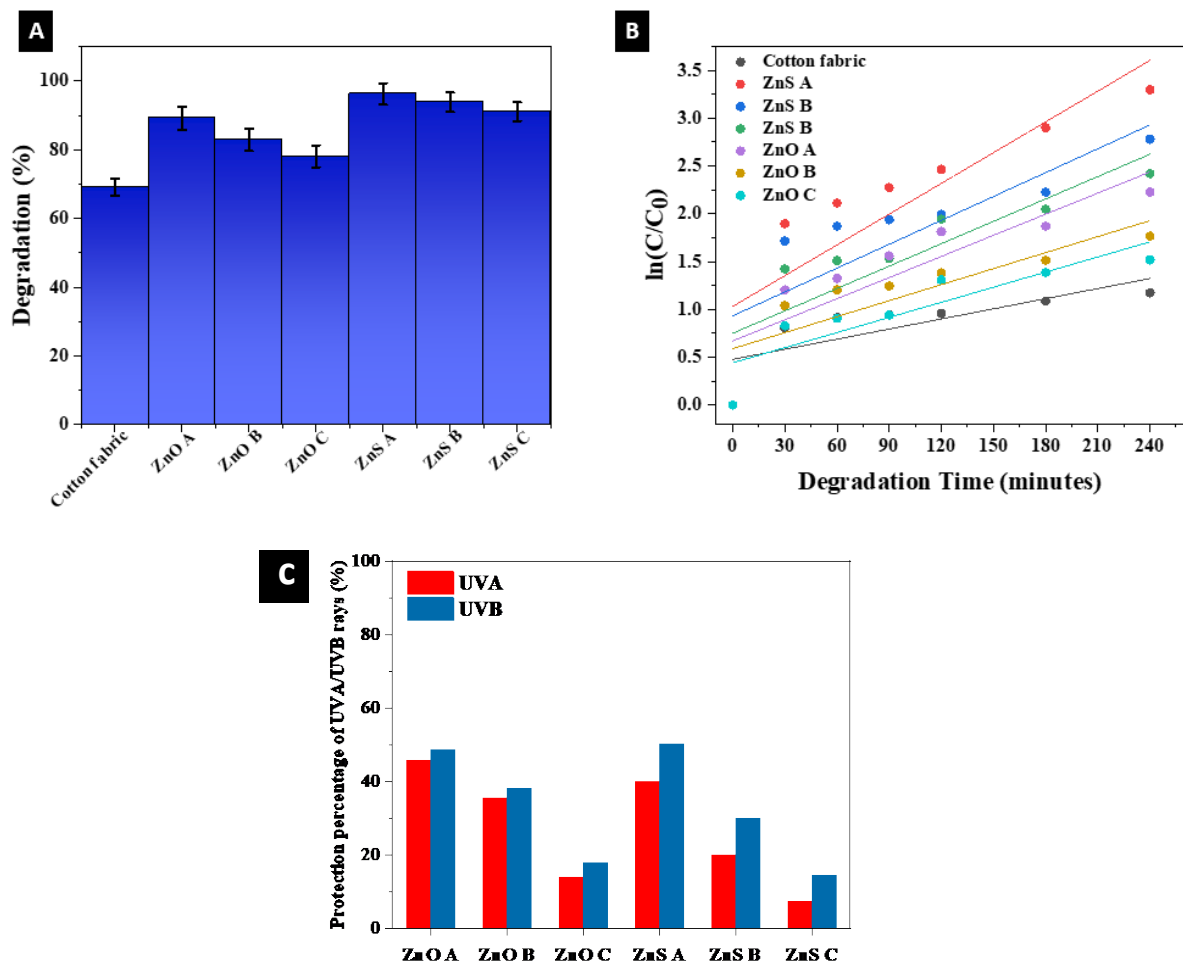

Source: authors (2022)

Table 4 - Pseudo-first-order kinetics for the photodegradation of MB dye

Sample	k (min^{-1})
Cotton fabric	0.0035 ± 0.0013
ZnS A	0.0107 ± 0.0028
ZnS B	0.0083 ± 0.0026
ZnS C	0.0078 ± 0.0021
ZnO A	0.0074 ± 0.0019
ZnO B	0.0056 ± 0.0016
ZnO C	0.0053 ± 0.0013

Source: authors (2022)

The ZnO and ZnS coatings demonstrated nice catalytic activity for MB photodegradation, suggesting a significant potential for use in disinfection technologies. Thus, to better understand these results and their future applications in such technologies, a complete computational study was conducted on their broad-spectrum biological properties of ZnO and ZnS coatings in this study. In particular, Zn_6O_6 and Zn_6S_6 clusters (see Figure 18-A) were selected as structural models for the ZnO and ZnS NPs, which were computationally evaluated for their ground and excited states. As shown in Figure 18-A, the clusters are composed of two chairs, both containing one Zn site (A) with equal O-Zn-O (1.905 Å) or S-Zn-S (2.300 Å) bond length, and two Zn (B) sites with different lengths, while the chairs mirror each other and are connected by Zn-O/Zn-S bonds. These two bond lengths confirm a hexagonal structure. The theoretical values calculated for the bond lengths of both clusters were in good agreement with the literature (AZPIROZ et al., 2012; BURNIN; SANVILLE; BELBRUNO, 2005; DE JESUS; JIMENEZ; LA PORTA, 2021; ESCUDERO; ESCAMILLA, 2011; HARUN et al., 2020; LA PORTA et al., 2014a; SOWA; AHSBAHS, 2006; WANG; DUKE, 1987; XIN-YU et al., 2007). All the Raman-active modes of both Zn_6O_6 and Zn_6S_6 clusters are shown in Figure 18-B. As expected, because of the electronegativity difference, the MEP assumes greater positive and negative values for the Zn_6O_6 cluster in relation to the Zn_6S_6 cluster (see Figure 18-C).

Figure 18 - A) Optimized structures and bond lengths, B) Raman spectra, and C) MEP maps of the ZnO and ZnS clusters

Source: authors (2022)
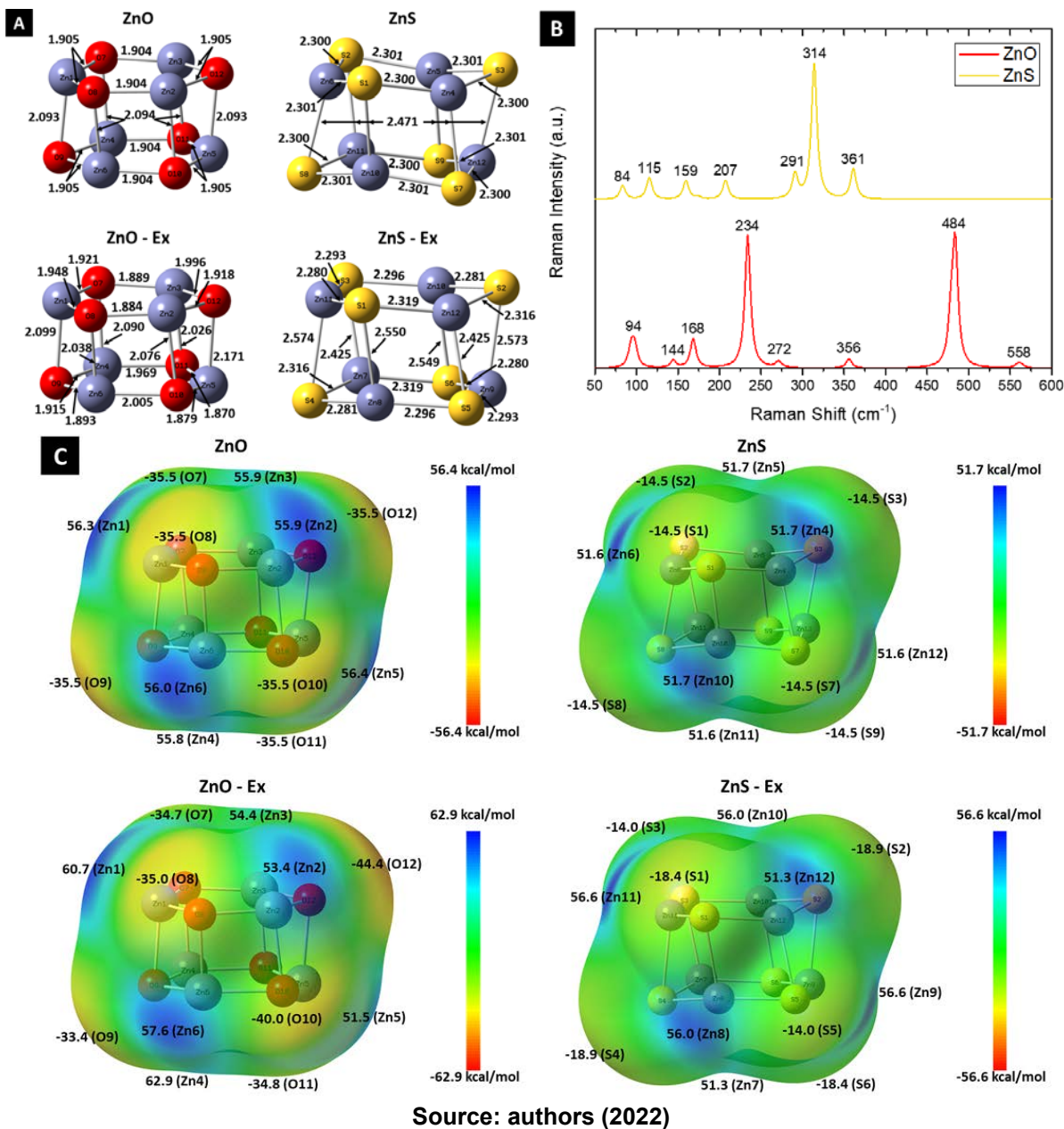
In general, the excited Zn_6O_6 cluster (as seen in the bond lengths reaching differences of up to 5% when compared with ground-state geometries) is more distorted than the Zn_6S_6 clusters. These results, therefore, suggest a greater increase in the ionic bond character of excited Zn_6O_6 cluster. To confirm these findings, QTAIM calculations were performed for both Zn_6O_6 and Zn_6S_6 clusters. It is important to observe that for the ionic bond: $\nabla^2\rho(r) > 0$; $-G/V > 1$; $G+V > 0$ and for the covalent bond: $\nabla^2\rho(r)< 0$; $-G/V < 1$; $G+V < 0$ (SILVA et al., 2017). The purpose here was to examine the chemical Zn-O and Zn-S bonds to investigate the covalent/ionic character. As

illustrated in Table 5, the increased Laplacian ($\nabla^2 p(r)$) values indicate that the Zn_6O_6 chemical bonds have a stronger ionic character than those of Zn_6S_6. However, the values for the parameters G+V and –G/V are extremely close and do not follow these trends. A charge analysis was performed for these compounds; however, it was observed that sulphur and oxygen have a partial charges of -0.8757 and -1.1853 for Zn_6S_6 and Zn_6O_6, respectively, in the computed data.

Table 5 - The QTAIM B3LYP/6-31+g (d, p) parameters, Laplacian ($\nabla^2 p(r)$), kinetic electron energy density ($G(r)$), and potential electron energy density ($V(r)$) for bond critical point (bcp) of Zn_6S_6 and Zn_6O_6

| Compounds	$\nabla^2 \rho(r)$	G	V	G+V	-G/V
ZnS*	0.135137	0.059238	-0.084692	-0.025454	0.69945
ZnS#	0.135913	0.058636	-0.083294	-0.024658	0.70396
ZnO*	0.396301	0.143431	-0.187786	-0.044355	0.76380
ZnO#	0.415852	0.149170	-0.194377	-0.045207	0.76742

*ground state, #excited state.

Source: authors (2022)

Furthermore, UV-vis and emission spectra were simulated for the Zn_6O_6 and Zn_6S_6 clusters, as shown in Figure 19-A and B, respectively. In these theoretical results, it is observed that the maximum absorption band is located at 357 nm for the Zn_6O_6 cluster (from HOMO-5 → LUMO transitions), whereas in the case of the Zn_6S_6 cluster, this peak is observed at approximately 371 nm (from HOMO-2 → LUMO transitions). The bandgap energies were estimated to be approximately 3.68 eV and 3.88 eV for the Zn_6O_6 and Zn_6S_6 clusters, respectively. In addition, the simulated emission spectrum was centered at 547 nm and 431 nm for Zn_6O_6 and Zn_6S_6, respectively, leading to Stokes shifts (i.e. the difference between the maximum absorption/emission peaks) of approximately 239 nm and 60 nm, respectively. The exciton binding energies were also calculated using the first excited state obtained from these clusters; approximately 0.87 eV and 0.79 eV for the Zn_6O_6 and Zn_6S_6 clusters, respectively, which are indeed much larger than the thermal energy resulting in a more pronounced excitonic resonance for these studied systems.

Figure 19 - UV-Vis and emission spectra of the A) Zn₆O₆ and B) Zn₆S₆ clusters. DOS spectra and HOMO-LUMO maps of C) Zn₆O₆ and D) Zn₆S₆ clusters in ground and excited states

Source: authors (2022)
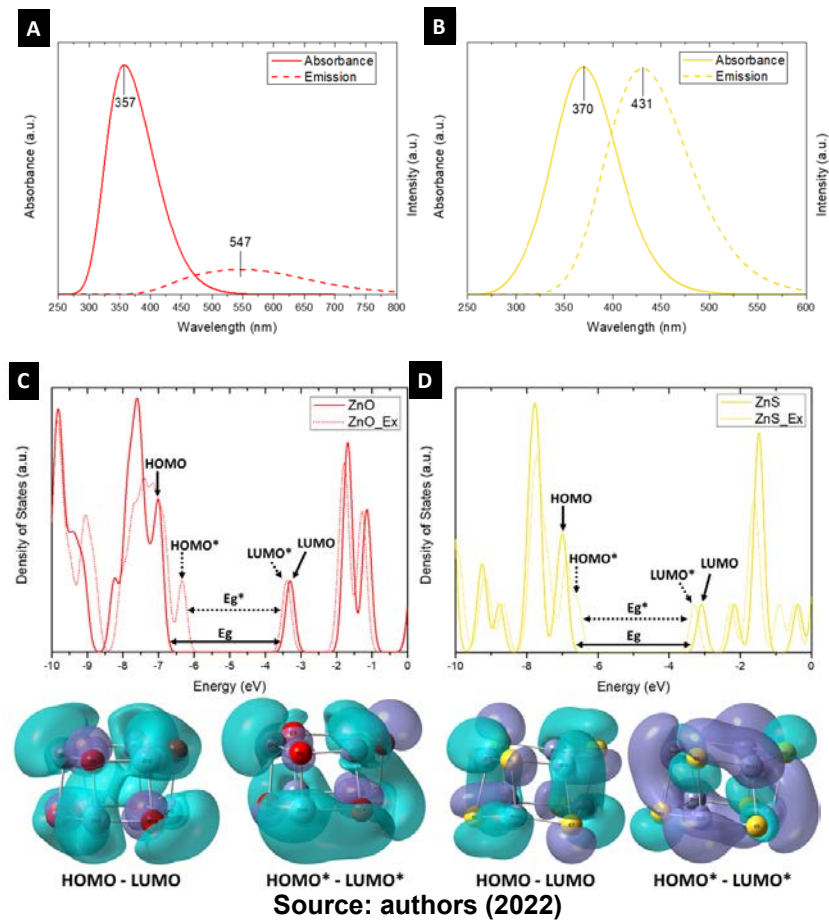
As indicated by the DOS spectrum of Zn_6O_6 in Figure 19-C, it was observed that the HOMO (-6.98 eV) and LUMO (-3.30 eV) are mainly composed by O $2p$ atomic orbitals and Zn $4sp$ hybrids, respectively. In the case of ZnS, the HOMO (-6.96 eV) is substantially formed by S $3p$ atomic orbitals, while the LUMO (-3.08 eV) is formed by Zn $4sp$ hybrid orbitals, as shown in Figure 19-D. In addition, the composition of the HOMOs and LUMOs for the ground and excited-states of the Zn_6O_6 and Zn_6S_6 clusters can be confirmed by the MOs surfaces in Figure 19-C and D, respectively. To complement this discussion, the estimated binding energies (BEs) of both Zn_6O_6 and Zn_6S_6 clusters, were computed from the difference between HOMO and Zn 3d orbital energies, and were calculated as -6.55 and -7.72 eV, respectively (DE JESUS; JIMENEZ; LA PORTA, 2021; LA PORTA et al., 2014c). Consequently, the projected DOS demonstrates that structural distortions lead to the formation of intermediate levels within the bandgap of these materials. To better illustrate the differences observed in the emission spectra of both Zn_6O_6 and Zn_6S_6 clusters in terms of the

order-disorder effects, the emission profile was deconvolved using the Voigt function, as shown in Figure 20-A and B.

Figure 20 - Deconvolution of the emission spectra of A) Zn_6O_6 and B) Zn_6S_6 from the respective transitions, oscillator strengths and MOs surfaces
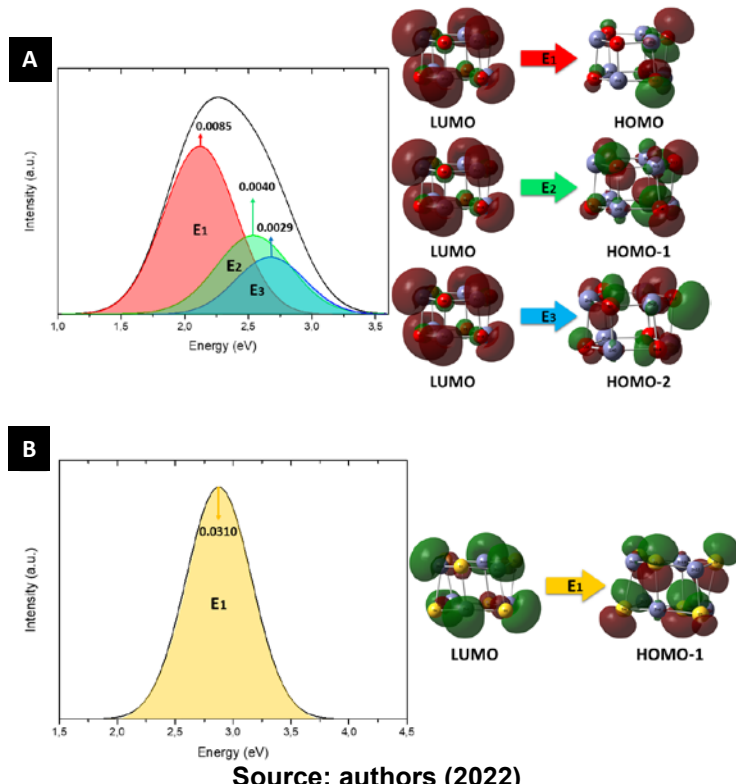
Source: authors (2022)

In Figure 20-A and B, the broad-band emission centered at 547 nm for the Zn_6O_6 cluster involves three oscillator strengths for the band position used in deconvolution; however, in the case of the Zn_6S_6 cluster, the emission peak at approximately 431 nm comprises of a single component. Based on our theoretical findings, this behavior is expected because of the more ionic character of the Zn-O bonds, which in turn can facilitate the visualization of these transitions in structural distortions. To study the nature of the excited states of these clusters, an analysis of charge transfer (μ_{CT}) was performed between Lewis-type donor and non-Lewis acceptor NBOs, by means of natural population analysis (NPAs). In the equation $\mu_{CT} = (NBO_{ES} - NBO_{GS})/(NBO_{ES} + NBO_{GS})$, where NBO_{ES} and NBO_{GS} are the natural charges of the excited and ground-state of these clusters, respectively. Hence, the estimated μ_{CT} value for the Zn_6O_6 cluster is 0.12672 e, which is much smaller than that obtained for the Zn_6S_6 cluster (0.40174 e). These μ_{CT} values are in alignment with the general tendency observed in other electronic properties, as the intense emission of

Zn_6S_6 cluster is reflected by higher charge transfer between donor and acceptor NBOs. The difference between the lowest excited singlet (S_1) state and triplet (T_1) state energy gap (ΔE_{S-T}) values were 0.90 eV for Zn_6O_6 and 1.13 eV for ZnS, which can in principle contribute to a high fluorescence rate for these clusters, providing a better structure-based understanding of their optical responses.

To elucidate the modes through which Zn_6S_6 and Zn_6O_6 interact with SARS-CoV-2, the crystal structure of the main protease (M^{pro}) of the virus in the complex with 6-(ethylamino)pyridine-3-carbonitrile was downloaded (DOUANGAMATH et al., 2020). The main variant of SARS-CoV-2 M^{pro} (R60C) was also prepared to investigate the interaction modes of these clusters in native and mutant enzymes. According to Khan et al. (KHAN et al., 2020), the R60C mutation in M^{pro} affects protein stability, thereby affecting the binding of ligands in the active site. The hydrogen bond network analysis demonstrated that the R60C mutation causes a disturbance in the interactions with the ligand as well as other surrounding active site M^{pro} residues. The authors noticed a large fluctuation in the hydrogen-bond network of the mutant M^{pro} (KHAN et al., 2020). Also, the Zn_6S_6 and Zn_6O_6 were evaluated against other organisms, including the *Escherichia coli* and *Fusarium Solani*. The crystal structures of DNA gyrase of *Escherichia coli* with chlorobiocin (LAFITTE et al., 2002) as well as cutinase of *Fusarium solani* with n-hexylphosphonate ethyl ester complexes (LONGHI et al., 1996) were also downloaded. Once the enzymes were prepared, the molecular docking protocol was initiated. First, re-docking calculations were performed using the MVD software (THOMSEN; CHRISTENSEN, 2006). To determine the best docking parameters, re-docking calculations were performed based on the orientation and conformation of the co-crystallised active ligand, which is found in the binding pocket of these enzymes.

The root-mean-square deviation (RMSD) variations obtained from the re-docking calculations suggested that the program correctly and efficiently simulated the experimental results for the respective ligands. RMSD values were 0.55 Å for native and mutant M^{pro}, 1.64 Å for DNA gyrase and 1.91 Å for cutinase. These preliminary results indicate that the conformational shift of the molecular docking technique is suitable for this study, and that the method is highly sensitive and specific. The re-docking overlay is shown in Figure 21. To simulate the ways in which the compounds interact with the molecular targets (native and mutant SARS-CoV-2 M^{pro}, *Escherichia coli* DNA gyrase and *Fusarium solani* cutinase), we used the best parameters provided

by the data from the re-docking validation performed with the co-crystallized active ligands.

Figure 21 - Re-docking overlaps of the initial (red) and representative (blue) structures and Root-Mean-Square Deviation (RMSD) values

| Native and Mutant M^{pro} SARS-CoV-2 **RMSD: 0.55 Å** | DNA gyrase *Escherichia coli* **RMSD: 1.64 Å** | Cutinase *Fusarium solani* **RMSD: 1.91 Å** |
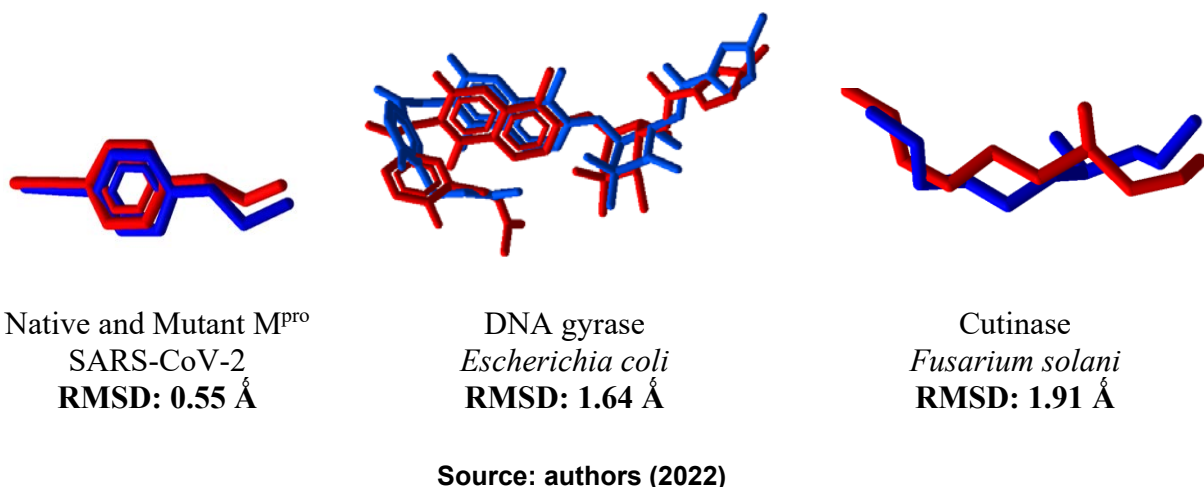
Source: authors (2022)

Table 6 - Intermolecular interaction energies (in kcal mol^{-1}) obtained through MVD

	M^{pro} SARS-CoV-2	M^{pro} (Mutant) SARS-CoV-2	DNA gyrase *Escherichia coli*	Cutinase *Fusarium solani*
Ground State				
ZnS	−44.36	−44.43	−42.68	−50.00
ZnO	−62.87 Asn142 / Cys145	−58.00 Asn142 / Cys145	−56.11 Ser121 / Val120 / Asn46 / Ala96	−54.28 Tyr119
Excited State				
ZnS	−92.69	−93.42	−89.58	−88.96
ZnO	−111.12 Ser144 / Cys145	−110.79 Ser144 / Cys145	−111.25 Thr165	−93.92 Tyr119

Source: authors (2022)

Molecular docking calculations were employed to investigate Zn$_6$S$_6$ and Zn$_6$O$_6$ the interaction modes in different organisms. Table 6 shows the intermolecular interaction energies for these compounds at M^{pro} binding site (native and mutant), DNA gyrase, and cutinase. According to our results, Zn$_6$S$_6$ and Zn$_6$O$_6$ exhibit robust stability when interacting with the investigated molecular targets, and the trend is indicated by the negative value stabilizing interactions of the intermolecular interaction energy.

For the viral M^{pro} enzyme, the compounds demonstrated similar stabilities within the active sites of the native and variant enzymes. For the native M^{pro}, the investigated Zn$_6$S$_6$ and Zn$_6$O$_6$ had an intermolecular energy variation between the

ground and excited states of 48.33 kcal mol^{-1} for Zn_6S_6 and 48.25 kcal mol^{-1} for Zn_6O_6. For the mutant M^{pro}, these variations were 48.99 kcal mol^{-1} for Zn_6S_6 and 52.79 kcal mol^{-1} for Zn_6O_6. The stability of the compounds Zn_6S_6 and Zn_6O_6 in the mutant M^{pro} active site was similar to that of the native enzyme. Thus, our findings suggest that these compounds may also act on this variant. According to the results computed for the cutinase of *Fusarium solani*, the interaction energies demonstrated a stabilizing effect, as supported by the favourable values of interaction energy obtained, similar to the results of M^{pro} of SARS-CoV-2. The interaction energy of Zn_6S_6 and Zn_6O_6 was also stabilizing when targeting the DNA gyrase of *Escherichia coli.* However, the interaction of the excited state of Zn_6O_6 cluster was more stabilizing for DNA gyrase than for cutinase. Trends regarding the interaction modes of these compounds were observed for both the ground and excited states, and in all cases, both Zn_6S_6 and Zn_6O_6 presented more stabilizing interactions in the excited site.

Furthermore, it was observed that Zn_6O_6 showed a more stabilizing interaction energy than ZnS in the ground and excited states (Table 6) for all molecular targets. In Table 6, it is observed that only the Zn_6O_6 compounds (ground and excited states) interacted with hydrogen-bond at the receptors active site, indicating that the presence of oxygen atoms in the chemical structure makes this interaction fundamental for stabilization. Conversely, the ZnS compounds did not form hydrogen-bonds, although they performed other intermolecular interactions which are important in stabilizing the ligands in the receptors' active sites, such as hydrophobic and electrostatic interactions.

Figure 22 - Intermolecular interactions of the best docking results (green dashed lines = hydrogen bond)

M^{pro}
SARS-CoV-2/ Ground State

M^{pro}
SARS-CoV-2/ Excited State

M^{pro} **(Mutant)**
SARS-CoV-2/ Ground State

M^{pro} **(Mutant)**
SARS-CoV-2/ Excited State

DNA gyrase
Escherichia coli/ **Ground State**

DNA gyrase
Escherichia coli/ **Excited State**

Cutinase
Fusarium solani/ **Ground State**

Cutinase
Fusarium solani/ **Excited State**
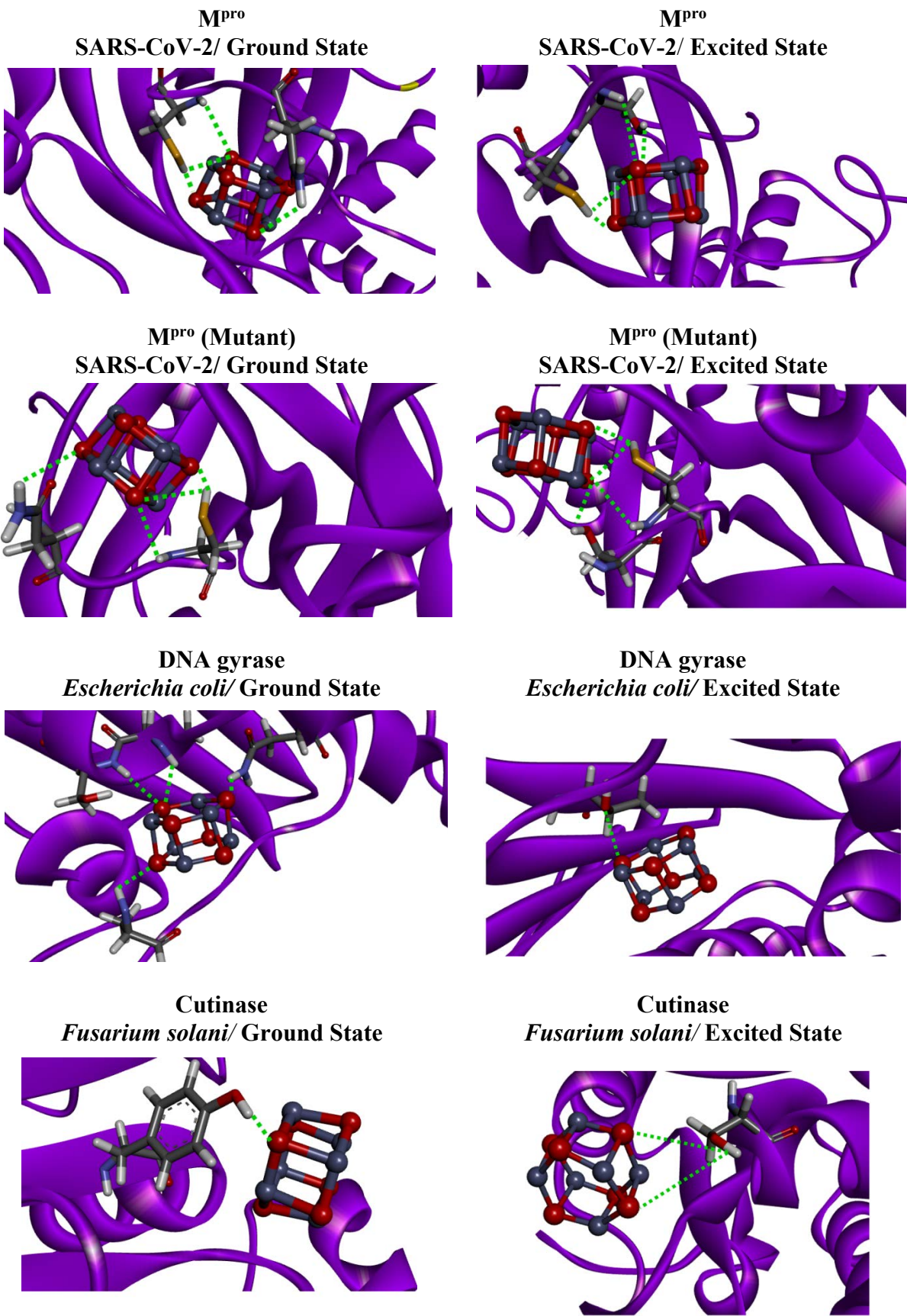
Source: authors (2022)

In general, Table 6 show the best docking results in terms of the intermolecular interaction energy, indicating that the Zn_6O_6 compounds in the excited state were more stable at the active sites of the molecular targets. As discussed previously, only Zn_6O_6 compounds performed hydrogen-bond interactions with receptors. These interactions are shown in Figure 22, in which the compounds performed interact with the residues Thr165, Ser121, Val120, Asn46, Ala96, Tyr119, Asn142, Cys145 and Ser144. Based on these results, it can be suggested that Zn_6S_6 and Zn_6O_6 compounds are important candidates for targeting these organisms. Also, the ADMET analysis was performed in order to elucidate the toxicity of ZnS and Zn_6O_6. The ADMET results obtained in this study demonstrate that Zn_6O_6 (LD_{50} = 3.425 mol/kg) and ZnS (LD_{50} = 3.628 mol/kg) have similar toxicities as their values of LD_{50} are close. However, Zn_6O_6 had a slightly smaller value, indicating that this compound could interact more with molecular targets. This trend was confirmed by the more stabilizing interaction energies of Zn_6O_6, as determined from the docking calculations. According to these values, the oxygen of Zn_6O_6 has a more negative partial charge, which can favor interactions within the binding sites of the molecular targets. This could explain the stronger interactions for Zn_6O_6 compounds.

5.4. Conclusions

In summary, we elucidated the physical and chemical properties of both ZnO and ZnS light-activated antimicrobial coatings based on a combination of experimental and theoretical approaches. Both ZnO and ZnS coatings had hexagonal wurtzite structures and were obtained successfully using the hydro(solvo)thermal method, with high reactivities as disinfection agents in photocatalysis reactions. Also, the ZnO- and ZnS-coated cotton fabrics provided excellent UV protective properties, which led to a blocking UVA and UVB rays significantly. An irregular sphere-like morphology was observed for the ZnS coating on the cotton fabric, while, under the same hydro(solvo)thermal conditions, a flower-like morphology (based on the self-assembly of nanorods) was obtained for the ZnO coating. Theoretical results showed that the excited ZnO cluster had a more polarized structure than that of ZnS, which can be confirmed by QTAIM results suggesting a stronger ionic character for Zn-O bonds. This leads to distortions in bond lengths and angles that influence its spectroscopic properties, as a direct consequence of intrinsic defects within the material. Regarding

the spectroscopic properties, the clusters exhibited similar absorbance spectra with peaks at 357 nm (ZnO) and 370 nm (ZnS). However, they had distinct emission spectra owing to their structures and differences in chemical bond character, with a broad band of ZnO (547 nm) with three components and the single emission peak of ZnS (431 nm). Our molecular docking results suggested that these ZnO and ZnS coatings have broad-spectrum antimicrobial properties. Therefore, these theoretical findings show that changes in the local chemical environment in these excited systems have a profound impact on their physical and chemical properties and thus can provide a better understanding to engineer new functional materials for light-activated antimicrobial coatings for mitigation of SARS-CoV-2 infection.

5.5. Acknowledgments

5.6. References

ACCELRYS SOFTWARE. **Discovery Studio Modeling Environment**San Diego, 2012.

ALMEIDA BATISTA, S. A. et al. Synthesis and comparison of antileishmanial and cytotoxic activities of S-(−)-limonene benzaldehyde thiosemicarbazones with their R-(+)-analogues. **Journal of Molecular Structure**, v. 1179, p. 252–262, 2019.

ASSIS, L. C. et al. Theoretical insights into the effect of halogenated substituent on the electronic structure and spectroscopic properties of the favipiravir tautomeric forms and its implications for the treatment of COVID-19. **RSC Advances**, v. 11, n. 56, p. 35228–35244, 2021a.

ASSIS, L. C. et al. Computational evidence for nitro derivatives of quinoline and quinoline N-oxide as low-cost alternative for the treatment of SARS-CoV-2 infection. **Scientific Reports**, v. 11, n. 1, p. 6397, 18 dez. 2021b.

AZPIROZ, J. M. et al. A first-principles study of II–VI (II = Zn; VI = O, S, Se, Te) semiconductor nanostructures. **Journal of Materials Chemistry**, v. 22, n. 40, p. 21453, 2012.

BARUAH, S.; DUTTA, J. Hydrothermal growth of ZnO nanostructures. **Science and**

Technology of Advanced Materials, v. 10, n. 1, p. 013001, 12 jan. 2009.

BERGER, D. et al. Improved photoluminescence emission and gas sensor properties of ZnO thin films. **Ceramics International**, v. 42, n. 12, p. 13555–13561, set. 2016.

BERMAN, H. M. et al. The Protein Data Bank. **Nucleic acids research**, v. 28, n. 1, p. 235–242, 2000.

BURNIN, A.; SANVILLE, E.; BELBRUNO, J. J. Experimental and Computational Study of the Zn n S n and Zn n S n + Clusters. **The Journal of Physical Chemistry A**, v. 109, n. 23, p. 5026–5034, jun. 2005.

COLON, G.; WARD, B. C.; WEBSTER, T. J. Increased osteoblast and decreased Staphylococcus epidermidis functions on nanophase ZnO and TiO2. **Journal of Biomedical Materials Research Part A**, v. 79, n. 4, p. 963–73, 2006.

DE CASTRO, A. A. et al. **New In Silico Insights into the Application of (Hydroxy)Chloroquine with Macrolide Antibiotic Co-Crystals against the SARS-CoV-2 VirusCOVID** , 2022.

DE JESUS, J. P. A. et al. Effect of drug metabolism in the treatment of SARS-CoV-2 from an entirely computational perspective. **Scientific reports**, v. 11, n. 1, p. 19998, out. 2021.

DE JESUS, J. P. A.; JIMENEZ, M. Z.; LA PORTA, F. DE A. Theoretical investigation on the effects of electric field on the electronic structure and spectroscopic properties of Zn6−xCdxS6 clusters as model systems of semiconductor quantum dots. **Computational Materials Science**, v. 188, p. 110147, fev. 2021.

DE SOUSA NETO, A. R.; DE FREITAS, D. R. J. Use of face masks: Indications for use and handling during the covid-19 pandemic. **Cogitare Enfermagem**, v. 25, p. 1–8, 2020.

DENNINGTON, R.; KEITH, T. A.; MILLAM, J. M. **GaussView, Version 6.1**, 2016.

DHAYGUDE, H. D. et al. Electrosynthesis of nanoflower like-ZnS thin films and its characterizations. **Journal of Materials Science: Materials in Electronics**, v. 26, n. 11, p. 8563–8567, 2015.

DHUPAR, A. et al. In-doped ZnS nanoparticles: structural, morphological, optical and antibacterial properties. **Applied Physics A**, v. 127, n. 4, p. 263, 2021.

DOUANGAMATH, A. et al. Crystallographic and electrophilic fragment screening of the SARS-CoV-2 main protease. **Nature Communications**, v. 11, n. 1, p. 5047, 2020.

DUAN, Z. et al. Understanding consumer behavior patterns in antibiotic usage for upper respiratory tract infections: A study protocol based on the COM-B framework.

Research in Social and Administrative Pharmacy, v. 17, n. 5, p. 978–985, 2021.

ESCUDERO, R.; ESCAMILLA, R. Ferromagnetic behavior of high-purity ZnO nanoparticles. **Solid State Communications**, v. 151, n. 2, p. 97–101, jan. 2011.

ESPITIA, P. J. P. et al. Zinc Oxide Nanoparticles: Synthesis, Antimicrobial Activity and Food Packaging Applications. **Food and Bioprocess Technology**, v. 5, n. 5, p. 1447–1464, 2012.

ETACHERI, V. et al. A highly efficient TiO2-xCx nano-heterojunction photocatalyst for visible light induced antibacterial applications. **ACS Applied Materials and Interfaces**, v. 5, n. 5, p. 1663–1672, 2013.

FARIAS, H. S. DE. O avanço da Covid-19 e o isolamento social como estratégia para redução da vulnerabilidadeO avanço da Covid-19 e o isolamento social como estratégia para redução da vulnerabilidadeL'avancement du Covid-19 et l'isolement social en tant que stratégie pour l. **Espaço e Economia**, n. 17, p. 0–12, 2020.

FDA. **Part 182—substances generally recognized as safe**.

FONSECA, A. F. V. DA et al. A theoretical and experimental investigation of Eu-doped ZnO nanorods and its application on dye sensitized solar cells. **Journal of Alloys and Compounds**, v. 739, p. 939–947, mar. 2018.

GARCIA, L. P. Uso de máscara facial para limitar a transmissão da COVID-19. **Epidemiologia e servicos de saude : revista do Sistema Unico de Saude do Brasil**, v. 29, n. 2, p. e2020023, 2020.

GUDKOV, S. V et al. **A Mini Review of Antibacterial Properties of ZnO Nanoparticles Frontiers in Physics** , 2021.

GUIMARAES, A. P. et al. Analysis of Bacillus anthracis nucleoside hydrolase via in silico docking with inhibitors and molecular dynamics simulation. **JOURNAL OF MOLECULAR MODELING**, v. 17, n. 11, p. 2939–2951, nov. 2011.

HAMDI, M. et al. Investigating the Internalization and COVID-19 Antiviral Computational Analysis of Optimized Nanoscale Zinc Oxide. **ACS Omega**, v. 6, n. 10, p. 6848–6860, 16 mar. 2021.

HARUN, K. et al. DFT + U calculations for electronic, structural, and optical properties of ZnO wurtzite structure: A review. **Results in Physics**, v. 16, p. 102829, mar. 2020.

HE, R.; TSUZUKI, T. Low-Temperature Solvothermal Synthesis of ZnO Quantum Dots. **Journal of the American Ceramic Society**, v. 93, n. 8, p. 2281–2285, ago. 2010.

HE, W. et al. Photogenerated charge carriers and reactive oxygen species in ZnO/Au hybrid nanostructures with enhanced photocatalytic and antibacterial activity. **Journal**

of the American Chemical Society, v. 136, n. 2, p. 750–757, 2014.

JANAKI, A. C.; SAILATHA, E.; GUNASEKARAN, S. Synthesis, characteristics and antimicrobial activity of ZnO nanoparticles. **Spectrochimica Acta - Part A: Molecular and Biomolecular Spectroscopy**, v. 144, p. 17–22, 2015.

KHAN, M. I. et al. Comparative genome analysis of novel coronavirus (SARS-CoV-2) from different geographical locations and the effect of mutations on major target proteins: An in silico insight. **PLOS ONE**, v. 15, n. 9, p. e0238344, set. 2020.

KHANLARY, M. R.; REYHANI, A. Growth temperature dependence of VLS-grown ultra-long ZnS nanowires prepared by CVD method. **Journal of Theoretical and Applied Physics**, v. 12, n. 2, p. 121–126, 2018.

KHO, R.; TORRES-MARTÍNEZ, C. L.; MEHRA, R. K. A simple colloidal synthesis for gram-quantity production of water- soluble ZnS nanocrystal powders. **Journal of Colloid and Interface Science**, v. 227, n. 2, p. 561–566, 2000.

KOKILAVANI, S. et al. Enhanced visible light driven photocatalytic and antibacterial activities of Ag2WO4 decorated ZnS nanocomposite. **Ceramics International**, v. 47, n. 9, p. 12997–13006, 2021.

KUMAR, P. S. V.; RAGHAVENDRA, V.; SUBRAMANIAN, V. Bader's Theory of Atoms in Molecules (AIM) and its Applications to Chemical Bonding. **Journal of Chemical Sciences**, v. 128, n. 10, p. 1527–1536, 2016.

KUMAR, R. et al. Efficient ZnO-based visible-light-driven photocatalyst for antibacterial applications. **ACS Applied Materials and Interfaces**, v. 6, n. 15, p. 13138–13148, 2014.

KWAMBOKA, B.; OMWOYO*, W.; OYARO, N. Synthesis, characterization and antimicrobial activity of ZnS nanoparticles. **Indian Journal of Nanoscience**, v. 4(2), 2016.

LA PORTA, F. A. et al. Synthesis of wurtzite ZnS nanoparticles using the microwave assisted solvothermal method. **Journal of Alloys and Compounds**, v. 556, p. 153–159, abr. 2013.

LA PORTA, F. A. et al. Zinc blende versus wurtzite ZnS nanoparticles: control of the phase and optical properties by tetrabutylammonium hydroxide. **Phys. Chem. Chem. Phys.**, v. 16, n. 37, p. 20127–20137, 2014a.

LA PORTA, F. A. et al. Correlation between structural and electronic order–disorder effects and optical properties in ZnO nanocrystals. **J. Mater. Chem. C**, v. 2, n. 47, p. 10164–10174, 8 out. 2014b.

LA PORTA, F. A. et al. A DFT Study of Structural and Electronic Properties of ZnS Polymorphs and its Pressure-Induced Phase Transitions. **Journal of the American Ceramic Society**, v. 97, n. 12, p. 4011–4018, dez. 2014c.

LA PORTA, F. A. et al. An experimental and theoretical investigation on the optical and photocatalytic properties of ZnS nanoparticles. **Journal of Physics and Chemistry of Solids**, v. 103, p. 179–189, abr. 2017.

LA PORTA, F. A.; TAFT, C. A. (EDS.). **Functional Properties of Advanced Engineering Materials and Biomolecules**. Cham: Springer International Publishing, 2021.

LA PORTA, F. DE A.; TAFT, C. A. (EDS.). **Emerging Research in Science and Engineering Based on Advanced Experimental and Computational Strategies**. Cham: Springer International Publishing, 2020.

LAFITTE, D. et al. DNA gyrase interaction with coumarin-based inhibitors: the role of the hydroxybenzoate isopentenyl moiety and the 5'-methyl group of the noviose. **Biochemistry**, v. 41, n. 23, p. 7217–7223, jun. 2002.

LAXMA REDDY, P. V. et al. TiO2-based photocatalytic disinfection of microbes in aqueous media: A review. **Environmental Research**, v. 154, n. January, p. 296–303, 2017.

LEE, J. H. et al. Soft-lithographically line-patterned In-doped ZnO quantum dots with hydrothermally grown ZnO nanocolumns for acetone detection. **Sensors and Actuators B: Chemical**, v. 329, p. 129131, fev. 2021.

LIAO, L. et al. Can N95 Respirators Be Reused after Disinfection? How Many Times? **ACS Nano**, v. 14, n. 5, p. 6348–6356, 26 maio 2020.

LONGHI, S. et al. Dynamics of Fusarium solani cutinase investigated through structural comparison among different crystal forms of its variants. **Proteins**, v. 26, n. 4, p. 442–458, dez. 1996.

LONGO, E.; LA PORTA, F. DE A. (EDS.). **Recent Advances in Complex Functional Materials**. Cham: Springer International Publishing, 2017.

MATHIEU, E. et al. A global database of COVID-19 vaccinations. **Nature Human Behaviour**, v. 5, n. 7, p. 947–953, 2021.

MATOS, K. S. et al. Molecular Aspects of the Reactivation Process of Acetylcholinesterase Inhibited by Cyclosarin. **JOURNAL OF THE BRAZILIAN CHEMICAL SOCIETY**, v. 22, n. 10, p. 1999–2004, 2011.

MICOLI, F. et al. The role of vaccines in combatting antimicrobial resistance. **Nature**

Reviews Microbiology, v. 19, n. 5, p. 287–302, 2021.

NAVARRO-LÓPEZ, D. E. et al. Effective antimicrobial activity of ZnO and Yb-doped ZnO nanoparticles against Staphylococcus aureus and Escherichia coli. **Materials Science and Engineering: C**, v. 123, p. 112004, 2021.

NI, Y. et al. Rapid fabrication and optical properties of zinc sulfide nanocrystallines in a heterogeneous system. **Materials Research Bulletin**, v. 39, n. 12, p. 1967–1972, 2004.

O'BOYLE, N. M.; TENDERHOLT, A. L.; LANGNER, K. M. cclib: A library for package-independent computational chemistry algorithms. **Journal of Computational Chemistry**, v. 29, n. 5, p. 839–845, 15 abr. 2008.

PADMAVATHY, N.; VIJAYARAGHAVAN, R. Enhanced bioactivity of ZnO nanoparticles - An antimicrobial study. **Science and Technology of Advanced Materials**, v. 9, n. 3, 2008.

RAI, M.; YADAV, A.; GADE, A. Silver nanoparticles as a new generation of antimicrobials. **Biotechnology Advances**, v. 27, n. 1, p. 76–83, 2009.

RAY, S. K. et al. Ag-BaMoO4: Er3+/Yb3+ photocatalyst for antibacterial application. **Materials Science and Engineering C**, v. 78, p. 1164–1171, 2017.

REGMI, C. et al. Understanding Mechanism of Photocatalytic Microbial Decontamination of Environmental Wastewater. **Frontiers in Chemistry**, v. 6, n. February, p. 1–6, 2018.

SANTOS, M. T. **As diferenças e semelhanças entre outros coronavírus e o Sars-CoV-2**.

SAPSFORD, K. E. et al. Biosensing with luminescent semiconductor quantum dots. **Sensors**, v. 6, n. 8, p. 925–953, 2006.

SATHISHKUMAR, M. et al. Antimicrobial activity of zinc sulphide nanoparticles and to study their characterization. **Elixir Electrical Engineering**, v. 101, n. December 2016, p. 44118–44121, 2016.

SATHISHKUMAR, M.; RAJAMANICKAM, A. T.; SAROJA, M. Characterization, antimicrobial activity and photocatalytic degradation properties of pure and biosynthesized zinc sulfide nanoparticles using plant extracts. **Journal of Materials Science: Materials in Electronics**, v. 29, n. 16, p. 14200–14209, 2018.

SILVA, T. C. et al. Molecular insight into the inhibition mechanism of plant and rat 4-hydroxyphenylpyruvate dioxygenase by molecular docking and DFT calculations. **MEDICINAL CHEMISTRY RESEARCH**, v. 24, n. 11, p. 3958–3971, nov. 2015.

SILVA, T. C. et al. Theoretical structural and electronic analyses with emphasis on the reactivity of iron oxide prototypes in methane C--H bond activation. **Reaction Kinetics, Mechanisms and Catalysis**, v. 120, n. 1, p. 195–208, 2017.

SIRELKHATIM, A. et al. Review on zinc oxide nanoparticles: Antibacterial activity and toxicity mechanism. **Nano-Micro Letters**, v. 7, n. 3, p. 219–242, 2015.

SOWA, H.; AHSBAHS, H. High-pressure X-ray investigation of zincite ZnO single crystals using diamond anvils with an improved shape. **Journal of Applied Crystallography**, v. 39, n. 2, p. 169–175, 1 abr. 2006.

SWANEPOEL, R. Determination of the thickness and optical constants of amorphous silicon. **Journal of Physics E: Scientific Instruments**, v. 16, n. 12, p. 1214–1222, 1983.

TESINI, B. L. **Coronavírus e Síndromes respiratórias agudas (COVID-19, MERS e SARS)**.

THOMSEN, R.; CHRISTENSEN, M. H. MolDock: A New Technique for High-Accuracy Molecular Docking. **J. Med. Chem.**, v. 49, p. 3315–3321, 2006.

UEKI, H. et al. Effectiveness of Face Masks in Preventing Airborne Transmission of SARS-CoV-2. **mSphere**, v. 5, n. 5, p. 2–6, 2020.

VANAJA, M. et al. Phytosynthesis and characterization of silver nanoparticles using stem extract of Coleus aromaticus. **International Journal of Materials and Biomaterials Applications**, v. 3, n. 1, p. 1–4, 2013.

WANG, Y. R.; DUKE, C. B. Atomic and electronic structure of ZnS cleavage surfaces. **Physical Review B**, v. 36, n. 5, p. 2763–2769, 15 ago. 1987.

WOROBEY, M. et al. The emergence of SARS-CoV-2 in Europe and North America. **Science**, v. 370, n. 6516, p. 564–570, 2020.

XIN-YU, Z. et al. Ab Initio Comparative Study of Zincblende and Wurtzite ZnO. **Chinese Physics Letters**, v. 24, n. 4, p. 1032–1034, abr. 2007.

ZHANG, R. et al. One-pot hydrothermal synthesis of ZnS quantum dots/graphene hybrids as a dual anode for sodium ion and lithium ion batteries. **Applied Surface Science**, v. 437, p. 375–383, abr. 2018.

ZHONG, H. et al. Reusable and Recyclable Graphene Masks with Outstanding Superhydrophobic and Photothermal Performances. **ACS Nano**, v. 14, n. 5, p. 6213–6221, 26 maio 2020.

ZHU, N. et al. A Novel Coronavirus from Patients with Pneumonia in China, 2019. **New England Journal of Medicine**, v. 382, n. 8, p. 727–733, 2020.

REFERÊNCIAS

ACCELRYS SOFTWARE. **Discovery Studio Modeling Environment**San Diego, 2012.

ALBERI, K. et al. The 2019 materials by design roadmap. **Journal of Physics D: Applied Physics**, v. 52, n. 1, p. 013001, 2 jan. 2019.

ALCOBA, D. R. et al. Treatment of non-nuclear attractors within the theory of atoms in molecules II: Energy decompositions. **Chemical Physics Letters**, v. 426, n. 4–6, p. 426–430, ago. 2006.

ALSBERG, B. K.; MARCHAND-GENESTE, N.; KING, R. D. A new 3D molecular structure representation using quantum topology with application to structure–property relationships. **Chemometrics and Intelligent Laboratory Systems**, v. 54, n. 2, p. 75–91, dez. 2000.

ANASORI, B. et al. Two-Dimensional, Ordered, Double Transition Metals Carbides (MXenes). **ACS Nano**, v. 9, n. 10, p. 9507–9516, 27 out. 2015.

ANDRADE, J. M. **Teoria do funcional da densidade aplicada na Caracterização do Catalisador CaSnO3**. [s.l.] Universidade Federal da Paraíba, 2016.

AOKI, R. M. et al. Application of heterostructured CdS/ZnS quantum dots as luminescence down-shifting layer in P3HT:PCBM solar cells. **Journal of Luminescence**, v. 237, p. 118178, set. 2021.

ASHRAFI, A.; JAGADISH, C. Review of zincblende ZnO: Stability of metastable ZnO phases. **Journal of Applied Physics**, v. 102, n. 7, p. 071101, out. 2007.

ASSIS, L. C. et al. Theoretical insights into the effect of halogenated substituent on the electronic structure and spectroscopic properties of the favipiravir tautomeric forms and its implications for the treatment of COVID-19. **RSC Advances**, v. 11, n. 56, p. 35228–35244, 2021a.

ASSIS, L. C. et al. Computational evidence for nitro derivatives of quinoline and quinoline N-oxide as low-cost alternative for the treatment of SARS-CoV-2 infection. **Scientific Reports**, v. 11, n. 1, p. 6397, 18 dez. 2021b.

AZPIROZ, J. M. et al. A first-principles study of II–VI (II = Zn; VI = O, S, Se, Te) semiconductor nanostructures. **Journal of Materials Chemistry**, v. 22, n. 40, p. 21453, 2012.

AZPIROZ, J. M.; UGALDE, J. M.; INFANTE, I. Benchmark Assessment of Density Functional Methods on Group II–VI MX (M = Zn, Cd; X = S, Se, Te) Quantum Dots.

Journal of Chemical Theory and Computation, v. 10, n. 1, p. 76–89, 14 jan. 2014.

BADER, R. F. W. Atoms in molecules. **Accounts of Chemical Research**, v. 18, n. 1, p. 9–15, 1 jan. 1985.

BADER, R. F. W. From Schrodinger to atoms in molecules. **Pure and Applied Chemistry**, v. 60, n. 2, p. 145–155, 1 jan. 1988.

BADER, R. F. W. A quantum theory of molecular structure and its applications. **Chemical Reviews**, v. 91, n. 5, p. 893–928, 1 jul. 1991.

BADER, R. F. W. A Bond Path: A Universal Indicator of Bonded Interactions. **The Journal of Physical Chemistry A**, v. 102, n. 37, p. 7314–7323, 1 set. 1998.

BADER, R. F. W.; BEDDALL, P. M. Virial Field Relationship for Molecular Charge Distributions and the Spatial Partitioning of Molecular Properties. **The Journal of Chemical Physics**, v. 56, n. 7, p. 3320–3329, abr. 1972.

BADER, R. F. W.; NGUYEN-DANG, T. T.; TAL, Y. A topological theory of molecular structure. **Reports on Progress in Physics**, v. 44, n. 8, p. 893–948, 1 ago. 1981.

BAI, H. et al. Facile synthesis of mesoporous CdS/PbS/SnO2 composites for high-selectivity H2 gas sensor. **Sensors and Actuators B: Chemical**, v. 340, p. 129924, ago. 2021.

BERGER, D. et al. Improved photoluminescence emission and gas sensor properties of ZnO thin films. **Ceramics International**, v. 42, n. 12, p. 13555–13561, set. 2016.

BERMAN, H. M. et al. The Protein Data Bank. **Nucleic acids research**, v. 28, n. 1, p. 235–242, 2000.

BIHAIN, M. F. R. et al. Cálculos teóricos para elucidação eletrônica de barreiras rotacionais: teoria e aplicações. **Journal of Biotechnology and Biodiversity**, v. 8, n. 2, p. 136–147, 26 jun. 2020.

BIMBERG, D.; POHL, U. W. Quantum dots: promises and accomplishments. **Materials Today**, v. 14, n. 9, p. 388–397, set. 2011.

BURKE, K. Perspective on density functional theory. **The Journal of Chemical Physics**, v. 136, n. 15, p. 150901, 21 abr. 2012.

BURNIN, A.; SANVILLE, E.; BELBRUNO, J. J. Experimental and Computational Study of the Zn n S n and Zn n S n + Clusters. **The Journal of Physical Chemistry A**, v. 109, n. 23, p. 5026–5034, 1 jun. 2005.

BURST, J. M. et al. CdTe solar cells with open-circuit voltage breaking the 1 V barrier. **Nature Energy**, v. 1, n. 3, p. 16015, 29 mar. 2016.

CATLOW, C. R. A. et al. Modelling nano-clusters and nucleation. **Phys. Chem. Chem.**

Phys., v. 12, n. 4, p. 786–811, 2010.

CEDER, G. Predicting Properties from Scratch. **Science**, v. 280, n. 5366, p. 1099–1100, 15 maio 1998.

CEPERLEY, D. M.; ALDER, B. J. Ground State of the Electron Gas by a Stochastic Method. **Physical Review Letters**, v. 45, n. 7, p. 566–569, 18 ago. 1980.

CHENG, L. et al. CdS-Based photocatalysts. **Energy & Environmental Science**, v. 11, n. 6, p. 1362–1391, 2018.

CORTES, A. Grain size dependence of the bandgap in chemical bath deposited CdS thin films. **Solar Energy Materials and Solar Cells**, v. 82, n. 1–2, p. 21–34, 1 maio 2004.

DE CASTRO, A. A. et al. New In Silico Insights into the Application of (Hydroxy)Chloroquine with Macrolide Antibiotic Co-Crystals against the SARS-CoV-2 Virus. **COVID**, v. 2, n. 3, p. 230–243, 28 fev. 2022.

DE JESUS, J. P. A. et al. Effect of drug metabolism in the treatment of SARS-CoV-2 from an entirely computational perspective. **Scientific Reports**, v. 11, n. 1, p. 19998, 7 dez. 2021.

DE JESUS, J. P. A.; JIMENEZ, M. Z.; LA PORTA, F. DE A. Theoretical investigation on the effects of electric field on the electronic structure and spectroscopic properties of Zn6−xCdxS6 clusters as model systems of semiconductor quantum dots. **Computational Materials Science**, v. 188, p. 110147, fev. 2021.

DENNINGTON, R.; KEITH, T. A.; MILLAM, J. M. **GaussView, Version 6.1**, 2016.

DHUPAR, A. et al. In-doped ZnS nanoparticles: structural, morphological, optical and antibacterial properties. **Applied Physics A**, v. 127, n. 4, p. 263, 21 abr. 2021.

DI MAURO, A. et al. ZnO for application in photocatalysis: From thin films to nanostructures. **Materials Science in Semiconductor Processing**, v. 69, p. 44–51, out. 2017.

DIAS, R.; DE AZEVEDO JR., W. Molecular Docking Algorithms. **Current Drug Targets**, v. 9, n. 12, p. 1040–1047, 1 dez. 2008.

FAN, J.; FU, A.; ZHANG, L. Progress in molecular docking. **Quantitative Biology**, v. 7, n. 2, p. 83–89, 4 jun. 2019.

FANG, X. et al. ZnS nanostructures: From synthesis to applications. **Progress in Materials Science**, v. 56, n. 2, p. 175–287, fev. 2011.

FILHO, E. B. A. et al. Synthesis and conformational study of a new class of highly bioactive compounds. **Chemical Physics Letters**, v. 449, n. 4–6, p. 336–340, dez.

2007.

FONSECA, A. F. V. DA et al. A theoretical and experimental investigation of Eu-doped ZnO nanorods and its application on dye sensitized solar cells. **Journal of Alloys and Compounds**, v. 739, p. 939–947, mar. 2018.

FOSTER, J. P.; WEINHOLD, F. Natural hybrid orbitals. **Journal of the American Chemical Society**, v. 102, n. 24, p. 7211–7218, 1 nov. 1980.

FRADERA, X.; AUSTEN, M. A.; BADER, R. F. W. The Lewis Model and Beyond. **The Journal of Physical Chemistry A**, v. 103, n. 2, p. 304–314, 1 jan. 1999.

GARG, P. et al. Hexagonal Planar CdS Monolayer Sheet for Visible Light Photocatalysis. **The Journal of Physical Chemistry C**, v. 120, n. 13, p. 7052–7060, 7 abr. 2016.

GLENDENING, E. D.; LANDIS, C. R.; WEINHOLD, F. Natural bond orbital methods. **WIREs Computational Molecular Science**, v. 2, n. 1, p. 1–42, 20 jan. 2012.

GRABOWSKI, S. J. et al. Quantitative Classification of Covalent and Noncovalent H-Bonds. **The Journal of Physical Chemistry B**, v. 110, n. 13, p. 6444–6446, 1 abr. 2006.

GUDKOV, S. V. et al. A Mini Review of Antibacterial Properties of ZnO Nanoparticles. **Frontiers in Physics**, v. 9, 11 mar. 2021.

GUIMARAES, A. P. et al. Analysis of Bacillus anthracis nucleoside hydrolase via in silico docking with inhibitors and molecular dynamics simulation. **JOURNAL OF MOLECULAR MODELING**, v. 17, n. 11, p. 2939–2951, nov. 2011.

HAFNER, J.; WOLVERTON, C.; CEDER, G. Toward Computational Materials Design: The Impact of Density Functional Theory on Materials Research. **MRS Bulletin**, v. 31, n. 9, p. 659–668, set. 2006.

HAUTIER, G.; JAIN, A.; ONG, S. P. From the computer to the laboratory: materials discovery and design using first-principles calculations. **Journal of Materials Science**, v. 47, n. 21, p. 7317–7340, 10 nov. 2012.

HOHENBERG, P.; KOHN, W. Inhomogeneous Electron Gas. **Physical Review**, v. 136, n. 3B, p. B864–B871, 9 nov. 1964.

HOSSEINI, M. et al. Reduction of Infectivity of SARS-CoV-2 by Zinc Oxide Coatings. **ACS Biomaterials Science & Engineering**, v. 7, n. 11, p. 5022, out. 2021.

HUANG, J.; YIN, Z.; ZHENG, Q. Applications of ZnO in organic and hybrid solar cells. **Energy & Environmental Science**, v. 4, n. 10, p. 3861, 2011.

J. FRISCH, M. et al. **Gaussian 09 (Revision A02)**. [s.l: s.n.].

JACAK, L.; WÓJS, A.; HAWRYLAK, P. **Quantum Dots**. Berlin, Heidelberg: Springer Berlin Heidelberg, 1998.

JAIN, A.; SHIN, Y.; PERSSON, K. A. Computational predictions of energy materials using density functional theory. **Nature Reviews Materials**, v. 1, n. 1, p. 15004, 11 jan. 2016.

JENNINGS, T. L. et al. Reactive Semiconductor Nanocrystals for Chemoselective Biolabeling and Multiplexed Analysis. **ACS Nano**, v. 5, n. 7, p. 5579–5593, 26 jul. 2011.

JIANG, L. et al. Phase Evolution and Morphology Control of ZnS in a Solvothermal System with a Single Precursor. **The Journal of Physical Chemistry C**, v. 112, n. 39, p. 15281–15284, 2 out. 2008.

KEITH, T. A.; BADER, R. F. W.; ARAY, Y. Structural homeomorphism between the electron density and the virial field. **International Journal of Quantum Chemistry**, v. 57, n. 2, p. 183–198, 15 jan. 1996.

KHAN, M. I. et al. Comparative genome analysis of novel coronavirus (SARS-CoV-2) from different geographical locations and the effect of mutations on major target proteins: An in silico insight. **PLOS ONE**, v. 15, n. 9, p. e0238344, set. 2020.

KLEIN, A. Energy band alignment in chalcogenide thin film solar cells from photoelectron spectroscopy. **Journal of Physics: Condensed Matter**, v. 27, n. 13, p. 134201, 10 abr. 2015.

KOCH, W.; HOLTHAUSEN, M. **A Chemist's Guide to Density Functional Theory**. 2nd. ed. [s.l.] Wiley-VCH, 2001.

KOHN, W.; SHAM, L. J. Self-Consistent Equations Including Exchange and Correlation Effects. **Physical Review**, v. 140, n. 4A, p. A1133–A1138, 15 nov. 1965.

KOVALENKO, M. V. et al. Prospects of Nanoscience with Nanocrystals. **ACS Nano**, v. 9, n. 2, p. 1012–1057, 24 fev. 2015.

LA PORTA, F. A. et al. Synthesis of wurtzite ZnS nanoparticles using the microwave assisted solvothermal method. **Journal of Alloys and Compounds**, v. 556, p. 153–159, abr. 2013.

LA PORTA, F. A. et al. Zinc blende versus wurtzite ZnS nanoparticles: control of the phase and optical properties by tetrabutylammonium hydroxide. **Phys. Chem. Chem. Phys.**, v. 16, n. 37, p. 20127–20137, 2014a.

LA PORTA, F. A. et al. A DFT Study of Structural and Electronic Properties of ZnS Polymorphs and its Pressure-Induced Phase Transitions. **Journal of the American Ceramic Society**, v. 97, n. 12, p. 4011–4018, dez. 2014b.

LA PORTA, F. A. et al. A DFT Study of Structural and Electronic Properties of ZnS Polymorphs and its Pressure-Induced Phase Transitions. **Journal of the American Ceramic Society**, v. 97, n. 12, p. 4011–4018, dez. 2014c.

LA PORTA, F. A. et al. An experimental and theoretical investigation on the optical and photocatalytic properties of ZnS nanoparticles. **Journal of Physics and Chemistry of Solids**, v. 103, p. 179–189, abr. 2017.

LA PORTA, F. A.; TAFT, C. A. (EDS.). **Functional Properties of Advanced Engineering Materials and Biomolecules**. Cham: Springer International Publishing, 2021.

LA PORTA, F. DE A.; TAFT, C. A. (EDS.). **Emerging Research in Science and Engineering Based on Advanced Experimental and Computational Strategies**. Cham: Springer International Publishing, 2020.

LAFITTE, D. et al. DNA gyrase interaction with coumarin-based inhibitors: the role of the hydroxybenzoate isopentenyl moiety and the 5'-methyl group of the noviose. **Biochemistry**, v. 41, n. 23, p. 7217–7223, jun. 2002.

LEE, G.-J.; WU, J. J. Recent developments in ZnS photocatalysts from synthesis to photocatalytic applications — A review. **Powder Technology**, v. 318, p. 8–22, ago. 2017.

LIN, M.-H.; HO, C.-H. Synthesis and Optical Characterization of Oxygen-Incorporated ZnS (1– x) O x for UV–Visible Color Palette Light-Emission Matter. **ACS Omega**, v. 2, n. 8, p. 4514–4523, 31 ago. 2017.

LONGHI, S. et al. Dynamics of Fusarium solani cutinase investigated through structural comparison among different crystal forms of its variants. **Proteins**, v. 26, n. 4, p. 442–458, dez. 1996.

LONGO, E.; LA PORTA, F. DE A. (EDS.). **Recent Advances in Complex Functional Materials**. Cham: Springer International Publishing, 2017.

LOOK, D. C. Recent advances in ZnO materials and devices. **Materials Science and Engineering: B**, v. 80, n. 1–3, p. 383–387, mar. 2001.

MATOS, K. S. et al. Molecular Aspects of the Reactivation Process of Acetylcholinesterase Inhibited by Cyclosarin. **JOURNAL OF THE BRAZILIAN CHEMICAL SOCIETY**, v. 22, n. 10, p. 1999–2004, 2011.

MATTA, C. F.; BOYD, R. J. (EDS.). **The Quantum Theory of Atoms in Molecules**. [s.l.] Wiley, 2007.

MATTSSON, A. E. et al. Designing meaningful density functional theory calculations

in materials science—a primer. **Modelling and Simulation in Materials Science and Engineering**, v. 13, n. 1, p. R1–R31, 1 jan. 2005.

MOHALLEM, J. R. Molecular structure and Bader's theory. **Theoretical Chemistry Accounts: Theory, Computation, and Modeling (Theoretica Chimica Acta)**, v. 107, n. 6, p. 372–374, 1 jun. 2002.

MOSTAFA, M. et al. Synthesis, structural, and optical properties of Mn2+ doped ZnS quantum dots for biosensor application. **Optical Materials**, v. 112, p. 110732, fev. 2021.

MURRAY, C. B.; KAGAN, C. R.; BAWENDI, M. G. Synthesis and Characterization of Monodisperse Nanocrystals and Close-Packed Nanocrystal Assemblies. **Annual Review of Materials Science**, v. 30, n. 1, p. 545–610, ago. 2000.

NASERTAYOOB, P.; SHAHBAZIAN, S. The topological analysis of electronic charge densities: A reassessment of foundations. **Journal of Molecular Structure: THEOCHEM**, v. 869, n. 1–3, p. 53–58, nov. 2008.

NAUSE, J.; NEMETH, B. Pressurized melt growth of ZnO boules. **Semiconductor Science and Technology**, v. 20, n. 4, p. S45–S48, 1 abr. 2005.

NAVARRO-LÓPEZ, D. E. et al. Effective antimicrobial activity of ZnO and Yb-doped ZnO nanoparticles against Staphylococcus aureus and Escherichia coli. **Materials Science and Engineering: C**, v. 123, p. 112004, abr. 2021.

NEUGEBAUER, J.; HICKEL, T. Density functional theory in materials science. **Wiley Interdisciplinary Reviews: Computational Molecular Science**, v. 3, n. 5, p. 438–448, set. 2013.

O'BOYLE, N. M.; TENDERHOLT, A. L.; LANGNER, K. M. cclib: A library for package-independent computational chemistry algorithms. **Journal of Computational Chemistry**, v. 29, n. 5, p. 839–845, 15 abr. 2008.

O'BRIEN, S. E.; POPELIER, P. LA. Quantum molecular similarity. Part 2: The relation between properties in BCP space and bond length. **Canadian Journal of Chemistry**, v. 77, n. 1, p. 28–36, 1 jan. 1999.

OLIVEIRA, B. G.; ARAÚJO, R. C. M. U.; RAMOS, M. N. A topologia molecular QTAIM e a descrição mecânico-quântica de ligações de hidrogênio e ligações de di-hidrogênio. **Química Nova**, v. 33, n. 5, p. 1155–1162, 2010.

PAGADALA, N. S.; SYED, K.; TUSZYNSKI, J. Software for molecular docking: a review. **Biophysical Reviews**, v. 9, n. 2, p. 91–102, 16 abr. 2017.

PALUSIAK, M.; GRABOWSKI, S. J. Characteristics of ring critical point as descriptors

of H-bond strength. **Journal of Chemical Research**, v. 2004, n. 7, p. 492–493, 27 jul. 2004.

PEARTON, S. .; REN, F. Advances in ZnO-based materials for light emitting diodes. **Current Opinion in Chemical Engineering**, v. 3, p. 51–55, fev. 2014.

PERDEW, J. P. **Jacob's ladder of density functional approximations for the exchange-correlation energy**. AIP Conference Proceedings. **Anais**...AIP, 2001Disponível em: <http://aip.scitation.org/doi/abs/10.1063/1.1390175>

PEREIRA DA SILVA, C. **COMPUTAÇÃO DE ALTO DESEMPENHO COM PLACAS GRÁFICAS PARA ACELERAR O PROCESSAMENTO DA TEORIA DO FUNCIONAL DA DENSIDADE**. Rio de Janeiro, Brazil: PONTIFÍCIA UNIVERSIDADE CATÓLICA DO RIO DE JANEIRO, 13 abr. 2010.

PLIEGO JR, J. R. Modelos contínuos do solvente: fundamentos. **Química Nova**, v. 29, n. 3, p. 535–542, jun. 2006.

POPELIER, P. On the full topology of the Laplacian of the electron density. **Coordination Chemistry Reviews**, v. 197, n. 1, p. 169–189, fev. 2000.

POPELIER, P. L. A. Quantum Molecular Similarity. 1. BCP Space. **The Journal of Physical Chemistry A**, v. 103, n. 15, p. 2883–2890, 1 abr. 1999.

QI, K. et al. Review on the improvement of the photocatalytic and antibacterial activities of ZnO. **Journal of Alloys and Compounds**, v. 727, p. 792–820, dez. 2017.

RAUBACH, C. W. et al. Photocatalytic activity of semiconductor sulfide heterostructures. **Dalton Transactions**, v. 42, n. 31, p. 11111, 2013.

RODE, J. E.; DOBROWOLSKI, J. C. Variation of BCP ellipticities in the course of the pericyclic and pseudopericyclic [2+2] cycloaddition reactions of cumulenes. **Chemical Physics Letters**, v. 449, n. 1–3, p. 240–245, nov. 2007.

SANVILLE, E.; BURNIN, A.; BELBRUNO, J. J. Experimental and Computational Study of Small (n = 1−16) Stoichiometric Zinc and Cadmium Chalcogenide Clusters. **The Journal of Physical Chemistry A**, v. 110, n. 7, p. 2378–2386, 1 fev. 2006.

SEH, Z. W. et al. Combining theory and experiment in electrocatalysis: Insights into materials design. **Science**, v. 355, n. 6321, 13 jan. 2017.

SHEN, H. et al. High-Efficient Deep-Blue Light-Emitting Diodes by Using High Quality Zn x Cd 1- x S/ZnS Core/Shell Quantum Dots. **Advanced Functional Materials**, v. 24, n. 16, p. 2367–2373, abr. 2014.

SILVA, T. C. et al. Molecular insight into the inhibition mechanism of plant and rat 4-hydroxyphenylpyruvate dioxygenase by molecular docking and DFT calculations.

MEDICINAL CHEMISTRY RESEARCH, v. 24, n. 11, p. 3958–3971, nov. 2015.

SPORTELLI, M. C. et al. On the Efficacy of ZnO Nanostructures against SARS-CoV-2. **International Journal of Molecular Sciences**, v. 23, n. 6, p. 3040, mar. 2022.

SUPREET; SINGH, G. Recent advances on cadmium free quantum dots-liquid crystal nanocomposites. **Applied Materials Today**, v. 21, p. 100840, dez. 2020.

SUZUKI, V. Y. et al. Characterization of the structural, optical, photocatalytic and in vitro and in vivo anti-inflammatory properties of Mn 2+ doped Zn 2 GeO 4 nanorods. **Journal of Materials Chemistry C**, v. 7, n. 27, p. 8216–8225, 2019.

TAFT, C. A. et al. Review: Simulation Models for Materials and Biomolecules. In: [s.l: s.n.]. p. 27–82.

TALAPIN, D. V. et al. Prospects of Colloidal Nanocrystals for Electronic and Optoelectronic Applications. **Chemical Reviews**, v. 110, n. 1, p. 389–458, 13 jan. 2010.

TERESHCHENKO, A. et al. Optical biosensors based on ZnO nanostructures: advantages and perspectives. A review. **Sensors and Actuators B: Chemical**, v. 229, p. 664–677, jun. 2016.

THOMSEN, R.; CHRISTENSEN, M. H. MolDock: A New Technique for High-Accuracy Molecular Docking. **Journal of Medicinal Chemistry**, v. 49, n. 11, p. 3315–3321, 1 jun. 2006.

UMMARTYOTIN, S.; INFAHSAENG, Y. A comprehensive review on ZnS: From synthesis to an approach on solar cell. **Renewable and Sustainable Energy Reviews**, v. 55, p. 17–24, mar. 2016.

UNDERWOOD, T. M.; ROBINSON, R. S. Adducing Knowledge Capabilities of Instrumental Techniques Through the Exploration of Heterostructures' Modification Methods. **ChemPhysChem**, set. 2022.

VENER, M. V. et al. QTAIM Study of Strong H-Bonds with the O−H···A Fragment (A = O, N) in Three-Dimensional Periodical Crystals. **The Journal of Physical Chemistry A**, v. 111, n. 6, p. 1155–1162, 1 fev. 2007.

VOROBYOV, I.; YAPPERT, M. C.; DUPRÉ, D. B. Energetic and Topological Analyses of Cooperative σH- and πH-Bonding Interactions. **The Journal of Physical Chemistry A**, v. 106, n. 44, p. 10691–10699, 1 nov. 2002.

WANG, K. et al. A highly sensitive and rapid organophosphate biosensor based on enhancement of CdS–decorated graphene nanocomposite. **Analytica Chimica Acta**, v. 695, n. 1–2, p. 84–88, jun. 2011.

YAN, F. et al. Design and discovery of a novel half-Heusler transparent hole conductor made of all-metallic heavy elements. **Nature Communications**, v. 6, n. 1, p. 7308, 24 nov. 2015a.

YAN, J. et al. Material descriptors for predicting thermoelectric performance. **Energy & Environmental Science**, v. 8, n. 3, p. 983–994, 2015b.

ZENG, X. et al. Photoelectrochemical Biosensor Using Enzyme-Catalyzed in Situ Propagation of CdS Quantum Dots on Graphene Oxide. **ACS Applied Materials & Interfaces**, v. 6, n. 18, p. 16197–16203, 24 set. 2014.

ZHANG, Y. et al. High-efficiency CdSe/CdS nanorod–based red light–emitting diodes. **Optics Express**, v. 27, n. 6, p. 7935, 18 mar. 2019.